Università di Firenze, Università di Perugia, INdAM consorziate nel CIAFM

DOTTORATO DI RICERCA
IN MATEMATICA, INFORMATICA, STATISTICA

CURRICULUM IN MATEMATICA
CICLO XXXIV

Sede amministrativa Università degli Studi di Firenze
Coordinatore Prof. Paolo Salani

Mathematical Models For Blood Flow
Modelli matematici per il flusso sanguigno

Settore Scientifico Disciplinare MAT/07

Dottorando:
Simone Guadagni

Tutore
Prof. Angiolo Farina

Coordinatore
Prof. Matteo Focardi

Anni 2018/2021

Contents

Introduction

This thesis deals with the mathematical modelling of hemorheology that consists in the study of blood flow either as a homogeneous fluid or as suspension of cells in plasma. Hemorheology is also concerned with the study of the interactions between blood components and between these components and the endothelial cells lining blood vessels. These aspects, however, are not explored in the thesis. An important impetus for progress in this field has been the evidence that many cardiovascular diseases have their main cause in poor circulation. Basically, pathologies with hemorheological origin such as leukemia, hemolytic anemia, thalassemia, or pathologies associated with risk factors for thrombosis and atherosclerosis, such as myocardial infarction, hypertension, stroke, or diabetes, are mainly associated with disturbances in local homeostasis. Therefore, the mathematical and numerical study of constitutive models that can capture the main rheological features of blood over a range of own conditions is ultimately recognized as an important tool for clinical diagnosis and treatment planning.

In the sequel, we will look at a few areas of hemorheology. In particular, we will deal with microcirculation, the part of the circulatory system that includes venules, arterioles, and capillaries. The microcirculation plays a fundamental role in the circulatory system, as it is the part of the system responsible for transporting blood to the periphery. The aging process naturally leads to a significant decrease in microcirculation, but this process can be accelerated by certain factors such as bad habits, environmental factors that are not positive or a poor lifestyle, leading to many diseases. For these reasons, it is particularly important to study the physiology of microcirculation, as it is still not fully understood. Specifically, in this thesis we will analyze the blood flow that occurs in vessels whose diameter is between about 100 and 500 micrometers. In this "segment"two important phenomena occur that are not yet fully explained.

The first fundamental phenomenon is the Fåhraeus-Lindqvist effect [35], which is observed in vessels with diameter less than about $500\mu m$. It consists in a variation in blood viscosity according to the vessel's diameter through it flows. This effect was discovered in the 1930s, and since then its causes are almost unknown. The most widely accepted qualitative explanation is due to R.H. Haynes [58], who

hypothesized the presence of a marginal layer attributable to the migration of red blood cells to the center of the vessel. As for its usefulness, recent studies have shown that while it leads to a substantial reduction in flow resistance and increasing discharge, it does not reduce energy dissipation [7].

The second phenomenon of greatest importance to the physiology of the microcirculatory system is the vasomotion, a rhythmical contraction-relaxation mechanism of microvessels, that regulates fluid and nutrient exchange between the vascular system and peripheral tissues.

This thesis is devoted to the mathematical modeling of these two phenomena, for which, as already mentioned, there are even nowadays no exhaustive theoretical explanations.

The first aim of this thesis is to study the Fåhreus-Lindqvist effect by means of a mathematical model capable of explaining the peculiar behavior of blood in vessels with a diameter of less than or on the order of 500-300 micrometers. The second goal of the thesis concerns the mathematical modeling of vasomotion. Existing models such as [36, 38], which describe the effects on blood flow, are poorly developed because they use inappropriate constitutive laws and consider rectilinear vessels. Therefore, both the rheological aspect and the study of flow in non-flat-walled channels need to be refined, in order to improve the knowledge gained so far and develop new ones based on it. To this end, we will approach the problem by modeling blood as a viscoplastic fluid, more specifically as a Casson fluid.

It is important to emphasize the original and innovative aspect of our research from the mathematical-modelling point of view. Indeed, we have developed out the study of a Casson flow in a duct with symmetric but not parallel walls in an analytical way. This study has been faced in the past using only numerical methods, since the tracking of the yield surface is extremely complex from a mathematical point of view. In viscoplastic fluids, the yield surface represents the interface between the part of the medium characterized by the behavior of a rigid body and the part characterized instead by the classical fluid behavior. The determination of the correct position of the yield surface is fundamental to describe the flow correctly. Because of these difficulties, the study of the peristaltic motion of a Casson fluid has never been tackled. In [55] we have developed a mathematical model allowing to correctly track the spatio-temporal evolution of the yield surface in vessels with non-flat walls and to provide the basis for a similar study on vessels with moving walls, as in the case of peristalsis.

Concerning the Fåhreus-Lindqvist effect, various theories have succeeded each other over the years, aiming to describe it theoretically. None of them, however, has been able to explain the peculiar curves of viscosity versus vessel diameter

obtained Fåhreus and Lindqvist in their 1930 paper [35]. In [54] the problem has been approached in a different way. The blood has been modeled as an inhomogeneous fluid, linking this inhomogeneity to the distribution of red blood cells over its cross section. With this mathematical model the Haynes' conjecture, which assumes migration of red blood cells towards the center of the vessel, has been justified. We have thus laid the foundation for a possible interpretation of the Fåhreus-Lindqvist effect from a fluid dynamical point of view.
After this brief introduction, the thesis develops as follows: In Chapter 1 we will make a quick historical excursus on how hematology emerged from obscurity and, the role of blood and, more generally, of medicine throughout the centuries. Then we analyze the main features of the human circulatory system. In Chapter 2 we will deal with the rheology of blood, deepening its composition of blood, and then analyzing its non-Newtonian properties from a mathematical point of view. We discuss its viscosity, its viscoelasticity and its thixotropic properties in order to describe the main mathematical models able to model its behavior. In Chapter 3, we enter the heart of our research activity by analyzing the Fåhraeus-Lindqvist effect. In particular, after a brief introduction in Section 3.1, we introduce the concept of apparent viscosity [50]. To better interpret and analyze experimental data on blood, we review the literature on the rheology of particle suspensions in Section 3.2. For rigid particles, there is a large amount of published literature. However, the study of suspensions with multiple, interacting, and highly deformable particles such as blood has received less attention and presents a challenge for both theoretical and computational fluid dynamics research. In Section 3.3, we introduce the concept of Marginal layer in a suspension, while Section 3.4 and the following ones are devoted to the definition of the mathematical model based on an entrance flow effect coupled with the Prandtl boundary layer theory. Finally, in Chapter 4 we address the issue of vasomotion and the modeling of blood as a Casson fluid. In detail: in Section 4.2 we introduce the mathematical model, the dimensionless form is obtained in Section 4.3 and the asymptotic expansions in Section 4.4, while the corresponding numerical results are given in Sections 4.5, 4.6. The peristaltic flow is studied in Section 4.9. Some final remarks will be drown in the last chapter.

Chapter 1

Historical aspects

The aim of this section is simply to give a brief sketchy overview of how hematology, one of the most sophisticated branches of medicine because of its close connection with biochemistry, emerged from obscurity. The importance of blood for life must have been clear to people in ancient times, with many implications on a religious level, e.g. from the Leviticus the Jews are obliged not to eat meat containing fresh blood. Closely related to this, in the ancient world health and disease were seen as expressions of supernatural forces, related to the will of gods and demons. In this mixture of superstition and magic, blood always played a crucial role: just think of the rites of blood sacrifice and drinking by which ancient civilization sought to obtain the grace of the gods.
Egyptian expertise in medicine was also highly valued by the Greeks, to the point of being praised by Homer in the Odyssey (c. 800 BC). The Egyptians were very familiar with the interior of the human body through the practice of mummification. They knew the main blood vessels (about 46) and the prominent role of the heart. According to clay tablets from the library of Ashurbanipal in Nineveh (7th century BC) reveal a much more mystical approach to medicine: the heart was the center of mental activity, blood was the essence of life, and the organ that controlled circulation was the liver. Egyptians and Mesopotamians certainly practiced bloodletting as a treatment for numerous diseases.
Hippocrates (c. 460 BC - c. 370 BC) was certainly the most influential figure in Western civilization from the standpoint of medicine. The main merit attributed to Hippocrates is the separation of medicine from religion (which in Greece was then dominated by the cult of Asklepios). According to Hippocrates, health depends on the balance of the four humors (blood, phlegm, black bile and yellow bile) became a paradigm that went unchallenged for centuries. Along with Hippocrates another important scholar was Alcmaeon of Croton (5th century BC), who was the first to distinguish arteries and veins on the basis of direct observations prac-

ticing dissection of animals. It should be remembered that Hippocrates theory, i.e. the interpretation of health as a balance of "entities", was also a defining feature of Eastern doctrines, at least as old as Ayurveda, the traditional Indian medicine. One of its basic principles is that the doshas, the three inner life forces, must be in balance to be healthy. Ayurveda is still widely practiced and includes bloodletting as one of the "five actions". Just as old and current as Ayurveda is traditional Chinese medicine, which is also inspired by the concept of the balance of two "principles": yin and yang, opposites and complementary forces [77].
Galen of Pergamon (131-201) achieved great fame in Rome where he became known as Aelius (Claudius) Galenus. Galen perfected the theory of Hippocrates by considering the combination of the four temperaments (choleric, melancholic, sanguine, phlegmatic) and the four qualities (cold, hot, humid, dry). Galen gave bloodletting fundamental importance as he believed that it restored the balance of the lost humors of the body. It is not for nothing that bloodletting was practiced almost until today, when it proved itself be a generally useless and even dangerous practice.

As already mentioned, over the centuries, blood circulation has fascinated scholars and intellectuals. However, only after the sixteenth century, hematology got rid of many false knowledge and embarked on the path that would lead it to one of the most important sectors of medicine. Aristotle (384-322 B.C.) declared that the heart was an organ with three chambers and the seat of the soul, a concept that has penetrated our civilization since even today heart and soul are used as synonyms. Aristotle's thought "no one will derive any benefit from their body after death"encouraged the practice of dissection of corpses resulting in many important discoveries. Vivisection of animals and even criminals sentenced to death, was performed publicly by Erasistratus (304-250 BC) and Herophilus (335-280 BC).
The theory of humors was also followed in Islamic medicine, although the famous Persian scientist Muhammad ibn Zakariya Razi (865-925), opposed to several of Galen's statements on the basis of his experimental observations. It is important to emphasize before 16th century the theories of Hippocrates, Aristotle and Galen, which later turned out to be wrong, dominated Western medicine.
Great credit for founding medicine as a modern science goes to Andries van Wesel (1514-1564), a Flemish anatomist better known as Andreas Vesalius, who revolutionized physiology by basing his studies on direct observation of dissected human bodies. In his most important work, De Humani Corporis Fabrica Libri Septem (1543), inspired by Razi's books, he pointed out several of Galen's errors (especially in the description of the circulatory system). During his life he was severely attacked by the followers of Galen, especially by the Church: It is said that he was sentenced to death in Spain because an autopsy appeared to show the heart of a presumed dead man beating (Leonardo da Vinci also had to stop his studies on

dissected corpses during his time in Rome because of accusations of witchcraft). Another brilliant scientist who gave an enormous contribution to the development of medicine was William Harvey (1578-1657) who in his famous treatise Exercitatio Anatomica De Motu Cordis et Sanguinis in Animalibus (1628) provided the first correct systematic description of blood circulation, limited to the great vessels. In this text he, based on a mechanical model, defined the heart the pump of the circulatory system. He also measured the amount of blood present in the body. He found that two ounces (about 59 ml) of blood leave the heart with each beat, so that at 72 heartbeats per minute, the heart pumps 540 pounds (about 245 l) of blood into the circulatory system every hour. Harvey, applying the principle of mass balance, showed that such a large amount of blood could not be created in the body and therefore the blood did not form but simply circulated in the body, thanks to the pumping action of the heart.
We also cite Andrea Cesalpino (1519-1603), an Italian anatomist and botanist, who demonstrated that the heart is the sole responsible for the movement of blood and that blood moves to and from the heart. This was shortly followed by the important contributions of the eclectic English scientist Stephen Hales (1677-1761), who determined the volume of blood in the body, the heart's power, and the blood pressure. To understand the composition of the blood, we had to wait until the end of the sixteenth century. Indeed, it was during this period that the microscope, attributed to the Dutchmen Hans and Zacharias Jannsen, was invented. The studies of Anthony Leeuwenhoek (1632-1723) paved the way for microbiology. In 1674 he studied red blood cells (RBCs), which had previously been identified in the blood of frogs by Jan Swammerdam (1658) and also observed by Marcello Malpighi (1628-1694). Because of their remarkably small size, it was necessary to wait much longer for the discovery of platelets, which occurred in 1842 with the advent of more powerful microscopes. In terms of size, it is quite curious that white blood cells (WBCs) or leukocytes, which are much larger than platelets, were not discovered in blood until a year later (1843). The reason for this late discovery is not because of the size of white blood cells, in fact they had already been observed in pus, but it had not been understood that they were part of the blood components. It was not until the nineteenth century that hematologists began to reap the benefits of many technological and scientific innovations. It was during this period that Lionel Beale (1828-1906), in his book The Microscope in its Applications to Practical Medicine, illustrated in great detail the constituents of blood known in his day. More recently, we recall the discovery of the system of blood groups A, B, O by the Nobel Prize winner (1930) Karl Landsteiner (1868-1943), who, together with the American scientist Alexander Solomon Wiener (1907-1976), also discovered the Rhesus factor (1937), which may (Rh+) or may not (Rh-) be present on the surface of red blood cells.

Chapter 2

Blood rheology

In this section we present a brief overview of the rheological properties of blood, including its most significant non-Newtonian characteristics and discuss the main constitutive models introduced to capture one or more of these properties.

2.1 Blood composition

Blood is a concentrated and complex heterogeneous suspension of various cellular elements, the hematocytes, in an aqueous solution, the plasma. Plasma is very abundant in blood, accounting for about 55% of its volume and consisting of about 92% of water. The rest is made up of proteins, waste products, and organic molecules. The most important cells carried by the blood are red blood cells (RBCs or erythrocytes), white blood cells (WBCs or leukocytes) and platelets (thrombocytes). The main function of plasma is to transport the substances it contains through the circulatory system. Let us now analyze the properties of hematocytes in more detail.
Leukocytes have an almost spherical shape, their diameter ranges from 6 to 17 μm and in an average man they have a concentration of about $7 - 11 \cdot 10^3$ per cubic millimeter. They are our body's defense cells and are particularly responsible for innate (natural, nonspecific) and acquired (adaptive, specific) immune responses.
Erythrocytes are biconcave disks of a much smaller size than leukocytes, but of a much higher concentration. They have a mean diameter of $6 - 8\mu m$ and a maximum thickness of $2 - 3$ μm. In an average man, the concentration of red blood cells is about $5 - 6 \cdot 10^6$ per cubic millimeter of blood. Red blood cells make up more than 99% of all blood cells. Hematocrit is defined as the percentage of red blood cells per unit volume of blood (about $40 - 45\%$ in an average man). The primary function of erythrocytes is to transport oxygen and carbon dioxide

throughout the body, thanks to hemoglobin.
Thrombocytes, on the other hand, are small fragments of nonnucleated disk-shaped cells, much smaller than erythrocytes and leukocytes, with a volume of about $2 - 3\ \mu m^3$.
Platelets are essential for blood clotting. Leukocytes and platelets make up about 1% of the remaining particles in the blood and are therefore of little importance in the study of blood rheology.

2.2 Blood rheological properties

A fluid is called Newtonian when shear stress and shear speed are proportional, the constant of proportionality being referred to as viscosity. Plasma, consisting mainly of water, can be considered a Newtonian fluid, but, in general, this is not true of blood due to the many particles it contains. To describe the rheological behavior of blood it is therefore necessary to use more sophisticated models than the simple Newtonian model. In particular, some of blood properties emerge when the size of the hematocytes is comparable to the size of the lumen. At the level of the systemic circulation, where the vessels have "larger"diameters blood can be considered as a homogeneous non-Newtonian fluid. On the other hand, if we consider the pulmonary circulation, where the diameter of the vessels is comparable to the size of the red blood cells, the blood cannot be modeled as a homogeneous fluid and we have to consider it as a suspension of hematocytes, mainly erythrocytes, in the plasma. The presence of cellular elements in the blood and their interactions lead to significant changes in the rheological properties of the blood and reliable measurements must be made to derive appropriate microstructure models.

The viscosity of blood is generally 2-4 times higher than that of plasma and depends mainly on the hematocrit. In particular, the non-Newtonian behavior of blood becomes more evident as the concentration of red blood cells increases, causing the hematocrit to rise. It has been observed that erythrocytes in blood at low shear rates tend to form an aggregate structure in the form of rods of individual cells called Rouleaux, which in turn can coalesce and form a three-dimensional branched structure. As a result, the viscosity of the suspension increases. In particular, the apparent viscosity increases slowly until the shear rate decreases to less than $1s^{-1}$, and then increases dramatically. Some studies have experimentally shown that rouleaux do not form when plasma proteins, fibrinogen, and globulins have been removed from the blood. In fact, suspensions of erythrocytes in plasma show strong non-Newtonian behavior, whereas the suspension in saline (without fibrinogen or globulins) shows Newtonian fluid behavior. When blood that has a high hematocrit and is nearly stationary, the presence of Rouleaux can induce a

yield stress that serves as a stress threshold for flow. At high shear rates, larger than $400s^{-1}$, the RBCs assume an elongated, ellipsoidal shape. Under these conditions, there is almost no collision between red blood cells and their contours revolve around their internal fluid. Therefore, the apparent viscosity decreases, a feature that becomes significant for vessels less than $1mm$ in diameter but is strongly pronounced for vessels with diameter less than $300\mu m$.
Geometric packing effects and radial migration of red blood cells can create a very thin layer of cell-free plasma near the vessel wall that has a lubricating effect. This is known as the Fåhraeus-Lindqvist effect. Plasma skimming is another effect that leads to a decrease in the apparent viscosity when blood flows in small vessels to the side of the parent vessel. This is due to a decrease in viscosity associated with a reduction in hematocrit (Fåhraeus effect). This occurs in small vessels or in regions of stable recirculation, such as the venous system and in parts of the arterial vascular system where the geometry has been altered (e.g., stenoses or aneurysms). However, in the system of large arteries, blood flow is basically Newtonian under normal physiological conditions.

A viscous fluid that is capable of storing and releasing energy is called viscoelastic. As we have mentioned in the previous sections, the behavior of blood depends greatly on the circumstances under which we analyze it. In blood with a normal hematocrit value, viscoelasticity is due to the reversible deformation of the 3D microstructures of red blood cells [29, 123], in particular, the elastic energy is due to the properties of the RBC membrane, which shows stress relaxation [34]. Considering the available experimental evidence, it is reasonable to develop non-Newtonian fluid models for blood that are capable of shear thinning and stress relaxation, where the relaxation time depends on the shear rate. For shear rates larger than $10s^{-1}$, the viscoelastic behavior of blood must be considered, while for shear rates below this threshold, the elastic nature of blood is negligible. Another important property of blood is its thixotropic behavior, i.e., the ability of pseudoplastic fluids to change their viscosity when subjected to shear stresses. In blood, this property is essentially due to processes such as the formation and dissolution of the 3D microstructure, the elongation and recovery of RBCs, and the formation and dissolution of the layers of aligned erythrocytes that develop in a finite time [8].

There are some substances, such as pastes, that do not deform at a shear stress below a critical value usually referred to, usually referred to as yield stress, while at a higher stress they start to flow. Materials with a yield stress are called Bingham fluids [15]. The explanation for this phenomenon is related to the energy required to break the internal bonds of the material: If this energy is sufficient, the material behaves like a fluid, otherwise it behaves like a rigid body. The critical stress level,

also known as the yield value or simply the yield, is considered to be a material property of the fluid. Blood is also believed to possess this property.
However, it is debatable whether the yield point of blood really exists, as the measurements made show a large variability, ranging from 0.002 to 0.40 $dynes/cm^2$[30]. This large difference is attributed to artifacts resulting from the interactions between the erythrocytes and the surfaces of the rheometer, as well as from the experimental methods used to measure the yield stress and the duration of the experiments [8].

2.3 Blood constitutive models

In this section, we will discuss the basic models most commonly used in large and medium-sized arteries i.e. radius larger than about 500 μm, to describe local blood flow. In these vessels, the blood behaves as a homogeneous fluid. This assumption does not hold true in smaller vessels (arterioles, venules and capillaries) where significant changes in rheological behavior occur.
In reality, blood is a non-Newtonian fluid, but assuming that all macroscopic length and time scales are sufficiently large relative to the length and time scales at the level of the individual erythrocyte so that the continuum assumption holds, it can still be considered a Newtonian fluid. For example, the apparent viscosity in arteries with diameters larger than $300\mu m$ is in the range of 3 to 4 times the one of water. The models we are going to illustrate are not suitable in the capillary network.
For an overview of hemorheology in the microcirculation, see the article by Popel and Johnson [98].

Blood flow in the cardiovascular system, as with other fluids, is subject to the conservation laws of momentum, mass, and energy described accordingly. Further constraints and conditions can be derived from the constitutive equations for the walls of the vessel. These walls are indeed flexible and subject to the mechanical drive of the heart, which strongly influences the dynamics of blood flow. For macroscopic modeling of blood flow, we consider the most general form of the constitutive equations for incompressible viscous fluids by defining the Cauchy stress tensor $\mathbf{T}$ such that

$$\mathbf{T} = -p\mathbf{I} + \boldsymbol{\tau} \tag{2.1}$$

where p is the Lagrange multiplier arising from the incompressibility constraint usually referred to as pressure, $\mathbf{I}$ is the identity matrix and $\boldsymbol{\tau}$ is the *extra-stress* (or deviatoric stress) tensor, representing the forces which the material develops

in response to being deformed.
We also introduce the strain rate tensor or rate of deformation tensor

$$\mathbf{D}(\mathbf{u}) \equiv \mathbf{D} = \frac{\left(\nabla \mathbf{u} + \nabla \mathbf{u}^T\right)}{2}. \tag{2.2}$$

where $\mathbf{u}$ is the fluid velocity.
In the sequel we will introduce some models characterized by a particular type of $\boldsymbol{\tau}$.
Talking about blood circulation, we can assume that blood is a Newtonian fluid when flows in large healthy arteries (diameter $\gtrsim 1\ mm$). However, under certain experimental or physiological conditions, especially at low shear rates, blood exhibits non-Newtonian properties and more complex constitutive models must be used. In this case, we need a more general constitutive equation that relates the stress to the shear rate. A very important class of constitutive equations that satisfy the invariance requirements can be written as follows

$$\boldsymbol{\tau} = \phi_1(II_D, III_D)\mathbf{D} + \phi_2(II_D, III_D)\mathbf{D}^2 \tag{2.3}$$

where II_D and III_D are the second and third principal invariants of the rate of deformation tensor $\mathbf{D}$, given by

$$II_D = \frac{(\operatorname{tr}\mathbf{D})^2 - \operatorname{tr}(\mathbf{D})^2}{2}, \qquad III_D = \det(\mathbf{D}). \tag{2.4}$$

Incompressible fluids like (2.3) are called Reiner-Rivlin fluids. Particular attention is given to a special class of Reiner-Rivlin fluids called generalized Newtonian fluids, for which

$$\boldsymbol{\tau} = 2\mu(II_D, III_D)\mathbf{D} \tag{2.5}$$

from which, assuming μ as a constant (called dynamic viscosity) we obtain the Navier-Stokes equations

$$\begin{cases} \rho\dfrac{\partial \mathbf{u}}{\partial t} + \rho\left(\mathbf{u}\cdot\nabla\right)\mathbf{u} = -\nabla p + \mu\Delta\mathbf{u} \\ \\ \nabla\cdot\mathbf{u} = 0 \end{cases} \tag{2.6}$$

where ρ is the blood density.
Since many fluids are mechanically incompressible $\operatorname{tr}\mathbf{D} = 0$ and it turns out that $II_D = -(\operatorname{tr}\mathbf{D}^2)/2$. Moreover, since also III_D vanishes in many flows, it is useful to introduce a measure of the rate of deformation, the so-called shear rate, usually denoted by $\dot{\gamma}$, and defined by

$$\dot{\gamma} = \sqrt{2tr\left(\mathbf{D}^2\right)} = \sqrt{-4II_D}, \tag{2.7}$$

and write the generalized Newtonian model (2.5) in the form

$$\boldsymbol{\tau} = 2\mu(\dot{\gamma})\mathbf{D}, \tag{2.8}$$

where $\mu(\dot{\gamma})$ is a shear dependent viscosity function. A simple example of a generalized Newtonian fluid is the power-law fluid, for which the viscosity function is given by

$$\mu(\dot{\gamma}) = K\dot{\gamma}^{n-1} \tag{2.9}$$

the positive constants n and K being the power-law index and the consistency, respectively. From this model we derive for $n = 1$ the Newtonian fluid model, i.e. the one with constant viscosity. For $n < 1$ we obtain a monotonically decreasing function of the shear rate, so that the fluid is called shear-thinning, while for $n > 1$ the viscosity increases with the shear rate and the fluid is called shear-thickening. In modeling blood, the shear thinning model is often used because it leads to "simple"analytical solutions, even though it imposes unphysical conditions: In fact, it predicts unbounded viscosity at zero shear rate and zero viscosity when $\dot{\gamma} \to \infty$. Viscosity functions that generalize (2.9) in the sense that have bounded and non-zero limiting values, can be written in the form

$$\mu(\dot{\gamma}) = \mu_\infty + (\mu_0 - \mu_\infty)\,\beta(\dot{\gamma}), \tag{2.10}$$

or, in non-dimensional form as

$$\frac{\mu(\dot{\gamma}) - \mu_\infty}{\mu_0 - \mu_\infty} = \beta(\dot{\gamma}). \tag{2.11}$$

Here, μ_0 and μ_∞ are the asymptotic viscosity values at zero and infinite shear rates and $\beta(\dot{\gamma})$ is a shear dependent function, satisfying the following natural limit conditions

$$\lim_{\dot{\gamma}\to 0} \beta(\dot{\gamma}) = 1, \qquad \lim_{\dot{\gamma}\to\infty} \beta(\dot{\gamma}) = 0. \tag{2.12}$$

Different choices of the function $\beta(\dot{\gamma})$ correspond to different models for blood flow, depending for example on hematocrit, temperature, plasma viscosity or other factor strictly related to the individual (age, gender and health condition).
An example of the beta function, which plays a major role in modeling blood is

$$\beta(\dot{\gamma}) = \left[1 + (\lambda\dot{\gamma})^a\right]^{\frac{n-1}{a}}, \qquad 0 < n < 1 \tag{2.13}$$

which is the Carreau-Yasuda model [18]. The parameters λ, n and a are the material constants specific for that kind of model.
Concerning viscoelasticity, a huge number of nonlinear viscoelastic constitutive models for blood are available. We are not going to use this kind of models in this

thesis, so we just give some information concerning them. One of the simplest rate type models accounting for the viscoelasticity of blood is the Maxwell model

$$\boldsymbol{\tau} + \lambda_1 \overset{\nabla}{\boldsymbol{\tau}} = 2\mu \mathbf{D} \tag{2.14}$$

where λ_1 is the relaxation time and

$$\overset{\nabla}{\boldsymbol{\tau}} = \frac{d\boldsymbol{\tau}}{dt} + (\mathbf{u} \cdot \nabla)\,\boldsymbol{\tau} - \nabla \mathbf{u} \boldsymbol{\tau} - \boldsymbol{\tau} \nabla \mathbf{u}^T \tag{2.15}$$

stands for the so-called upper-convected Oldroyd derivative, a generalization of the material time derivative $\frac{d\boldsymbol{\tau}}{dt} = \frac{\partial \boldsymbol{\tau}}{\partial t} + \mathbf{u} \cdot \nabla \mathbf{u}$, chosen so that $\overset{\nabla}{\boldsymbol{\tau}}$ is objective under a superposed rigid body motion and the resulting second-order tensor is symmetric [100][199].
A more general class of rate type models, includes the Oldroyd-B models [87] defined by

$$\boldsymbol{\tau} + \lambda_1 \overset{\nabla}{\boldsymbol{\tau}} = 2\mu(\mathbf{D} + \lambda_2 \overset{\nabla}{\mathbf{D}}) \tag{2.16}$$

where the material coefficient λ_2 denotes the retardation time and is such that $0 \leq \lambda_2 < \lambda_1$. Oldroyd-type fluids are considered Maxwell fluids with additional viscosity. These types of models, also called upper convection Maxwells, are a generalization of the earlier model (2.14). Thurston [121, 122] was one of the first (1972) to recognize the viscoelastic nature of blood, noting that viscoelastic behavior becomes less pronounced with increasing shear rate.
Among the differential viscoelastic constitutive models recently proposed in the literature we just mention the empirical five-constant generalized Oldroyd-B model introduced by Yeleswarapu [125]. In this model, the constant viscosity μ of (2.16) was replaced by a generalized Newtonian viscosity of the form

$$\mu(\dot{\gamma}) = \mu_\infty + (\mu_0 - \mu_\infty) \left[\frac{1 + \ln(1 + \zeta \dot{\gamma})}{1 + \zeta \dot{\gamma}} \right]. \tag{2.17}$$

The 3 parameters μ_0, μ_∞ and ζ have been derived by fitting experimental data for steady capillary flow. This model captures the shear thinning behavior of blood over a large range of shear rates but it has some limitations, since the relaxation times do not depend on the shear rate, which does not agree with experimental observations.
We now illustrate some viscoplastic models that are often encountered in hemorheology. The behavior of viscoplastic materials shows a critical value of stress below which the material does not flow. As mentioned before, such a critical value is usually referred to as yield stress. Viscoplastic materials are also called Bingham plastics, after Bingham [16], who was the first to describe several types of paint in

this way in 1919. The models used for these materials included also the Herschel-Bulkley model [59], the Casson model [22] and the Heinz-Casson model [42]. A detailed review of viscoplastic fluids can be found, in Bird, Dai and Yarusso [17], Mitsoulis [81], Huilgol [61], Frigaard and Nouar [43] and Farina et al. [37].
All these models have various practical applications. The Herschel-Bulkley models are used for muds, foams, ceramics and slurries. The Casson model is widely used to model blood flow [39, 36] as it describes blood flow quite well in low shear regions. Indeed, the Casson fluid undergoes no deformation until the shear stress is below the critical threshold and above such a threshold it displays a shear thinning behavior. Merrill et al. [79] found that at shear rates in the range $0.1 - 1.0\ s^{-1}$ the Casson constitutive equation fitted very well the experimental data. We however remark that yield stress models can be useful to model blood flow in low shear rate regions though the existence of a yield stress for blood and its use as a material parameter is still nowadays a controversial issue.
Yield stress materials require a finite shear stress τ_o (the so-called yield stress) to start flowing. A relatively simple, and physically relevant yield criterion is given by

$$|\boldsymbol{\tau}| = \tau_o, \tag{2.18}$$

where $|\boldsymbol{\tau}| = \sqrt{II_{\boldsymbol{\tau}}}$, $II_{\boldsymbol{\tau}}$ being the second invariant of the extra stress tensor, $\boldsymbol{\tau}$ (see (2.4)). We mean that, for $|\boldsymbol{\tau}| < \tau_o$, the fluid does not flow.
The simplest yield stress model is the Bingham fluid [15] which can be written in the form

$$\begin{cases} \mathbf{D} = \mathbf{O} & \text{if } |\boldsymbol{\tau}| < \tau_o, \\ \boldsymbol{\tau} = 2\left[\mu + \dfrac{\tau_0}{\sqrt{2\dot{\gamma}}}\right]\mathbf{D} & \text{if } |\boldsymbol{\tau}| \geq \tau_o \end{cases} \tag{2.19}$$

where μ is the viscosity attained when the fluid flows and $\dot{\gamma}$ is given by (2.7).
Other yield stress models commonly used for blood are the Herschel-Bulkley and the Casson models (see e.g. [100, 101]), both capturing a nonlinear dependence of viscosity on shear rate.
The Herschel-Bulkley model displays a power-law viscosity like (2.9) and can be written in a form similar to (2.19)

$$\begin{cases} \mathbf{D} = \mathbf{O} & \text{if } |\boldsymbol{\tau}| < \tau_o, \\ \boldsymbol{\tau} = 2\left[K\dot{\gamma}^{n-1} + \dfrac{\tau_0}{\sqrt{2\dot{\gamma}}}\right]\mathbf{D} & \text{if } |\boldsymbol{\tau}| \geq \tau_o, \end{cases} \tag{2.20}$$

where $\dot{\gamma}$ is the shear rate given by (2.7).
The most common yield stress model for blood is the Casson constitutive model

[109] which, has the form

$$\begin{cases} \mathbf{D} = \mathbf{O} & \text{if } |\boldsymbol{\tau}| < \tau_o, \\ \boldsymbol{\tau} = 2\left[\sqrt{\mu} + \dfrac{\sqrt{\tau_0}}{\sqrt{2\dot{\gamma}}}\right]^2 \mathbf{D} & \text{if } |\boldsymbol{\tau}| \geq \tau_o, \end{cases} \tag{2.21}$$

As for the Herschel-Bulkley fluid, the Casson fluid behaves rigidly until (2.18) is satisfied, and after that it displays a shear thinning behavior.

When constitutive equations (2.19)-(2.21) are considered, one has to solve a very complex problem even in a simple 2D setting. In particular, one has to track the evolution of the σ interface, where the constitutive equation exhibits a "singularity". Indeed, for Casson model (2.21), it is easy to see extrapolate the relation between the norm $|\boldsymbol{\tau}| = \mathrm{tr}\,(\boldsymbol{\tau}^2)$ and $\dot{\gamma}$ given by (2.7), namely

$$\begin{cases} |\boldsymbol{\tau}| = \left[\sqrt{\mu\dot{\gamma}} + \sqrt{\tau_o}\right]^2 & \dot{\gamma} > 0, \\ |\boldsymbol{\tau}| \in [0, \tau_o] & \dot{\gamma} = 0, \end{cases} \tag{2.22}$$

which is a graph and not a function. Moreover (2.22) is not differentiable in $\dot{\gamma} = 0$. To bypass this difficulty, it is generally used to smooth the constitutive relationship by considering (see [81] for more details) the Papanastasiou model [88],

$$|\boldsymbol{\tau}| = \left[\sqrt{\mu\dot{\gamma}} + \sqrt{\tau_o}(1 - e^{-\sqrt{m\dot{\gamma}}})\right]^2, \qquad \text{Papanastasiou} \tag{2.23}$$

or alternatively with the Bercovier-Engelman model [14]

$$|\boldsymbol{\tau}| = \left[\sqrt{\mu\dot{\gamma}} + \sqrt{\frac{\tau_o\dot{\gamma}}{\dot{\gamma} + e}}\right]^2, \qquad \text{Bercovier-Engelman,} \tag{2.24}$$

where m and e are positive parameters. In particular (2.23) and (2.24) converge to the Casson model (2.21) for $m \to \infty$ and for $e \to 0$. The advantage of using (2.23) or (2.24) lies in the fact that the apparent viscosity $\mu(\dot{\gamma})$ is now a differentiable function of $\dot{\gamma}$ for all $\dot{\gamma} \geqslant 0$.
In Figure 2.1 we have plotted the regularized constitutive equations (2.23), (2.24) for different values of the parameters m, e. Using the regularized models (2.23), (2.24) the constitutive equation can be rewritten as

$$\boldsymbol{\tau} = \mu_i(\dot{\gamma})\mathbf{D} \qquad i = P,\ BE$$

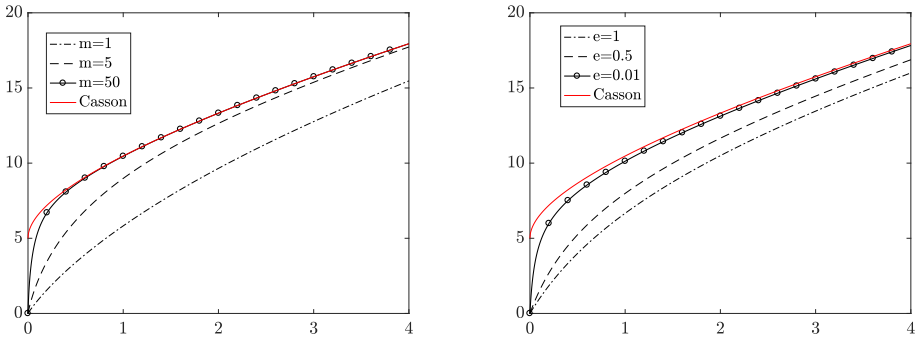

Figure 2.1: Shear stress vs Shear rate: regularized models. In the left panel Papanastasiou regularized model, in the right one Bercovier-Engelman regularized model

with

$$\begin{cases} \mu_p(\dot\gamma) = \left(\sqrt{\mu} + \sqrt{\tau_o}\dfrac{(1-e^{-\sqrt{m\dot\gamma}})}{\dot\gamma}\right)^2, & \text{(Papanastasiou).} \\ \\ \mu_{be}(\dot\gamma) = \left(\sqrt{\mu} + \sqrt{\dfrac{\tau_o}{\dot\gamma + e}}\right)^2, & \text{(Bercovier-Engelman).} \end{cases} \tag{2.25}$$

When we consider (2.25) the Navier-Stokes system (2.6) becomes

$$\begin{cases} \operatorname{div}\mathbf{v} = 0, \\ \\ \rho\dfrac{d\mathbf{v}}{dt} = -\nabla p + \operatorname{div}\left(\mu_i(\dot\gamma)\mathbf{D}\right). \end{cases}$$

If $\mu_i = const$ we recover the classical Navier-Stokes model (2.6).

Chapter 3

Microcirculation and the Fåhraeus- Lindqvist effect

In 1930 a new blood effect, which was destinated to revolutionize the knowledge of hemodynamics and be an hemodynamical open problem still nowadays, was first documented by a German group, [74]. Shortly after, in 1931, it was reported independently by the Swedish scientists Robin Fåhraeus and Johan Torsten Lindqvist, after whom the discovery is commonly named as the *Fåhraeus-Lindqvist effect* [35]. This effect consists in the fact that blood viscosity seems to vary depending on the diameter of the vessel in which blood flows. In particular, starting with vessels smaller than $300\mu m$ in diameter and considering tubes whose diameters were smaller and smaller until a minimum length of $4 - 5\mu m$, the two scientists observed a corresponding decrease in blood viscosity. Consequently, they concluded that blood cannot be considered a Newtonian fluid, i.e., a linear viscous fluid (with constant viscosity), when it flows through vessels whose diameter is less than or, at least, equal to about $300\mu m$: such interpretation is acceptable limited to blood vessels greater than $300\mu m$ in diameter. In particular, this entails that blood does not fulfill the Poiseuille law in all vessels: indeed, such law holds true only for Newtonian fluids and, as we stated above, this is not the case for blood in microvessels.

Fåhraeus and Lindqvist experiment was carried out by using a viscosimeter which was linked to a mercury manometer and a thermostat to keep pressure and temperature constant. Moreover, there was an important difference between such viscosimeter and those which had been developed since that moment: it made the blood flow through an horizontal rotating glass tube, so red blood cells could not accumulate on the vessel floor. In order to establish a possible viscosity change depending on the tube diameter, they kept it constant, as well as pressure and temperature, and they prevented blood coagulation by means of a sodium citrate

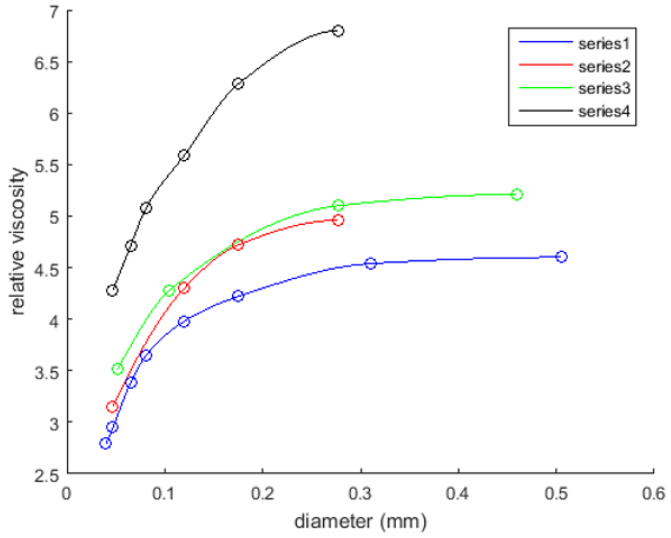

Figure 3.1: Experimental results of R. Fåhreus and T. Lindqvist [35]. In the axis of ordinate is shown the apparent viscosity of blood relative to that of plasma. In particular, in series 1 the plasma viscosity is 1.63, in series 2 the viscosity of the plasma is 1.65, in series 3 the plasma viscosity is 1.60. Series 4 refers to artificially plasma-depleted blood (plasma viscosity is 1.72).

solution.
Through the years, lots of explanations of the phenomenon succeeded one another, [7]. Nowadays, the interpretation which has received the largest agreement in the scientific community is the plasma cell-free layer model, which was developed by Haynes, [58], in the 1950s.
According to him, there is a thin layer adjacent to the capillary wall that is depleted of red blood cells and it is usually called plasma layer or marginal zone or cell-free layer.
Since it is red cell-poor, its (effective) viscosity is lower than that of whole blood, resulting in a reduction of flow resistance within the capillary, with the net effect that the (effective) viscosity is less than that for whole blood. Moreover, due to the fact that the cell-free layer is very thin (approximately $2 - 3\mu m$), [111], this effect is insignificant in vessels whose diameter is large.
However, this explanation, while accurate, is ultimately unsatisfying, since it fails to answer the fundamental question of why a plasma cell-free layer forms. Many studies, the majority of which consisted of numerical simulations, [110], have been carried out in order to find the way to solve this issue, but none of them proved satisfactory.
The aim of this chapter is to propose a new approach to the problem. Drawing inspiration from another fluid dynamics phenomenon, the so-called channel entrance flow, which is based on Prandtl boundary layer theory, our approach is to develop a mathematical model aimed at describing the formation of the marginal layer.

3.1 Apparent viscosity

The flow resistance of a vessel is defined as

$$R = \frac{\Delta p}{Q}, \tag{3.1}$$

where Δp is the pressure drop driving the flow and Q is the discharge (or volume flow rate). R is a quantity of obvious relevance in the study of blood flow in tubes and shows (provided it is constant) that the blood flow Q is directly proportional to Δp, in other words the greater the pressure difference, the greater the flow.
Applying Hagen-Poiseuille law to the steady laminar flow of a Newtonian fluid with viscosity μ, we get

$$Q = \frac{\pi}{128}\frac{\Delta p D^4}{L\mu}, \tag{3.2}$$

which implies

$$R = \frac{128 L \mu}{\pi D^4}.$$

So, flow resistance is proportional to the fluid viscosity, tube length L and sensitively dependent on the diameter D by being proportional to its inverse fourth power. This result is physiologically important, as it shows how relatively small changes in the diameter of microvessels can cause substantial changes in flow resistance and thereby control the distribution of blood flow to tissues at the local level.
In order to analyze the rheological effects which are associated with RBCs in microvessels, it is convenient to rearrange (3.2) and define the apparent viscosity of blood as

$$\mu_{app} = \frac{\pi}{128}\frac{D^4}{L}R = \frac{\pi}{128}\frac{D^4}{L}\frac{\Delta p}{Q}. \tag{3.3}$$

Consequently, the relative apparent viscosity is given by $\mu_{rel} = \mu_{app}/\mu_p$, where μ_p is the viscosity of the plasma or any other suspending medium. Of course, for a Newtonian fluid $\mu_{app} = \mu$ but, in general (i.e., for a non-Newtonian fluid) μ_{app} is not the fluid "viscosity".

In 1931, Robin Fåhraeus and Johan Torsten Lindqvist, showed that the blood apparent viscosity varies depending on the diameter of the tube it travels through, [35], i.e. the so-called Fåhraeus-Lindqvist effect.
Over the years many scholars have tried to theoretically explain the dependence of apparent viscosity on the vessel diameter. The proposed theories have never led to satisfactory results. However, in the 1990s, attempts were made to reproduce, with best fitting techniques, the behavior of the apparent viscosity as a function of the vessel diameter and blood hematocrit. In 1992, Axel Prieset al., [96], collected and analyzed multiple experimental results on the flow of RBCs suspensions in glass tubes and they developed an empirical equation for the dependence of the relative apparent viscosity on the tube diameter D, in μm, and hematocrit H_D[1],

$$\mu_{rel} = 1 + (\mu_{45} - 1)\frac{(1 - H_D)^C - 1}{(1 - 0.45)^C - 1}, \tag{3.4}$$

where

[1]Another effect that we are not going to discuss here is the *Fåhraeus effect*, a phenomenon in which the tube hematocrit, H_T, i.e. the volume of red blood cells divided by total blood volume in a tube, is less than the so-called discharge hematocrit, H_D, i.e. the hematocrit of the blood within the reservoir feeding the vessel.

$$\mu_{45} = 220\exp(-1.3D) + 3.2 - 2.44\exp(-0.06D^{0.645})$$

is the relative apparent blood viscosity for a discharge hematocrit $H_D = 0.45$. The exponent C giving the dependence on hematocrit is governed by

$$C = (0.8 + \exp(-0.075D))\left(-1 + \frac{1}{1 + 10^{-11}D^{12}}\right) + \frac{1}{1 + 10^{-11}D^{12}}. \tag{3.5}$$

In 1994, Pries et al., [50], through an indirect approach in which they examined the distributions of blood flow and hematocrit in vivo, i.e. in microvascular networks, derived an empirical relationship to describe the dependence of the apparent viscosity on the vessel diameter and hematocrit for flows in vivo. Indeed the few such data available suggested that the apparent viscosity in vivo was higher than the one expected according to (3.4), developed for glass tube experiments.
The new formula elaborated by Pries and coworkers is

$$\mu_{rel} = \left[1 + (\mu_{45} - 1)\frac{(1 - H_D)^C - 1}{(1 - 0.45)^C - 1}\left(\frac{D}{D - 1.1}\right)^2\right]\left(\frac{D}{D - 1.1}\right)^2,$$

where

$$\mu_{45} = 6\exp(-0.085D) + 3.2 - 2.44\exp(-0.06D^{0.645})$$

is the relative apparent blood viscosity for $H_D = 0.45$ and the quantity C is given by equation (3.20). According to this result, the apparent viscosity in living microvessels with a diameter of $30\mu m$ or less is markedly higher than its value in glass tubes with corresponding diameters. The main cause of this difference was found to be the presence of an ESL, or glycocalyx, on the inner surface of endothelial cells, with a width of the order of $1\mu m$. This layer consists of a dilute matrix of loosely bound macromolecules, which largely impedes plasma flow in its interior and thereby reduces the effective lumen available width for the flow of plasma and RBCs.
During the past 20 years, the above equations for the apparent viscosity of blood in vitro and in vivo have been used extensively in theoretical analysis of blood flow in networks of microvessels. Nevertheless, the development of theories capable of predicting the behaviors described by these equations and, moreover, explaining the causes of RBCs migration to the central core has proved to be a formidable challenge. In the remaining part of the chapter, we show that RBCs migration from the blood vessel outer layer toward the central region can be rigorously modeled. However, for the time being, we restrict ourselves to illustrate the most important theories that have been proposed until now.

3.2 Marginal layer

The formation of a cell-free layer near the vessel walls is the main reason for the distinctive properties of blood in microvessels and, thus, for the Fåhraeus-Lindqvist effect.
Several studies about physical phenomena contributing to this behavior have been carried out (just using simulation techniques) since 1970s and they are discussed below. Many references on such issue may be found in the recent paper by Timothy W. Secomb [110].

- **Size exclusion Effect**

  The RBC center of mass is excluded from a zone near the wall as a result of the finite size of the RBC. For an RBC in a disk-like configuration, the minimum dimension is at least $2\mu m$, so the center of mass of the cell cannot physically approach within $1\mu m$ of the wall.

- **Migration Away from Solid Boundaries**

  For Stokes flow of suspensions in tubes, migration away from the walls is a consequence of particle deformability. Indeed, a neutrally buoyant rigid particle in a dilute suspension does not generally migrate across the flow away from a solid boundary in Stokes flow. For spherical particles, this result follows from the fact that equations of fluid motion are linear and that a reversal of the flow direction would result in the opposite migration, which would be a contradiction. For non-spherical particles, the same argument applies if the particle and flow have symmetry with respect to a plane perpendicular to the flow direction at some point during motion. The migration is demonstrated in three-dimensional simulations of motions of RBCs and other deformable particles in shear flow near a solid boundary. However, a general mechanistic understanding of the phenomenon has proved elusive: no proof has been presented that such migration direction is always true for this kind of particles.

- **Migration Resulting from the Curvature of the Velocity Profile**

  The mechanism we discussed in the previous paragraph would occur in the case of a linear shear flow over a solid boundary. A distinct mechanism for migration arises from the fact that the fluid motion in tube flow has a curved velocity profile, with a velocity gradient that increases from the centerline to the wall (Poiseuille flow). Therefore, the effect of velocity profile curvature is likely to play a significant role in the migration of RBCs to the centerline in dilute suspensions, but experimental studies are still actually

unable to understand how much such curvature is responsible for it owing to the impossibility to separate wall effects from the velocity curvature ones.

- **Effects of the Endothelial Surface Layer**

  The walls of living microvessels are lined with a layer of macromolecules attached to endothelial cells forming the inner surface of the vessel walls: it is referred to as the ESL or glycocalyx. Although static RBCs can compress the layer, flowing of RBCs and plasma are excluded by a lubrication-type[2] mechanism, which has been likened to skiing on powder snow. Despite the fact that mechanics of interactions between suspended particles and a deformable porous wall layer is an interesting and biologically relevant topic, it has only recently received little attention.

- **Migration due to Cell-to-Cell Interactions**

  Under physiological conditions with a hematocrit of $40 - 45\%$, the RBCs trend of migrating to the centerline is obviously opposed by the effect of RBCs crowding in the interior of the vessel. In a suspension subject to shear flow, the high concentration leads to frequent collisions, which cause fluctuations in lateral velocity and drive a diffusion-like motion of the particles, with a net flux down the concentration gradient. Such effect is called shear-induced diffusion or dispersion. Therefore, the width of the cell-free layer is governed by the balance between the various mechanisms driving the formation and enlargement of the layer and the opposing effects of shear-induced diffusion. However when it comes to put such theory into practice, the predicted hematocrit profile should show a cusp in the vessel centerline which has never been observed.

In recent years, advances in numerical techniques and in parallel computation capabilities have made it feasible to perform direct simulations of multiple RBCs flowing in narrow tubes, including a fairly realistic representation of the cells' mechanical properties. From such simulations, the apparent viscosity of the flow can be deduced, and the statistical properties of the time-varying cell-free layer thickness can be analyzed. In simulations by Dmitry Fedosov et al., [40, 41], the predicted relative apparent viscosity agreed closely with experimental results for hematocrits between 15% and 45% and tube diameters from 10 to $40\mu m$. Moreover, the average cell-free layer thickness agreed with an estimated value of $1.8\mu m$. These findings support the view that the flow properties of blood in narrow glass

[2]In fluid dynamics, lubrication theory describes the flow of fluids (liquids or gases) in a geometry in which one dimension is significantly smaller than the others. An example is the flow above air hockey tables, where the thickness of the air layer beneath the puck is much smaller than the dimensions of the puck itself.

tubes can indeed be understood in terms of the mechanical properties of individual RBCs and principles of fluid mechanics. At the same time, this approach requires a separated, computationally intensive simulation for each case of interest, and fundamental fluid mechanical mechanisms may be difficult to deduce from the results.

3.3 Marginal layer in suspensions

The model that we will illustrate in the next sections to theoretically explain the formation of the marginal layer is based on a different approach from those listed in the previous section. To simplify the model as much as possible, we will treat blood as a suspension of non-deformable particles in a Newtonian fluid. In this framework, the hematocrit ϕ represents the volume fraction occupied by the particles. Because of their importance in industrial and biological applications such as fluidized beds [5, 52], pneumatic transportation [25], particle sedimentation [51], [49], mud flows and landslides [116], blood [39, 110] and so on, the two-constituent flows of a mixture composed of a Newtonian fluid and solid particles have been the subject of numerous theoretical studies.
Suspensions present diverse rheological behavior such as shear thinning, shear thickening, and thixotropy depending on the microstructure of the materials, the nature of the interactions involved, and the properties of the carrier liquid. Rheology of suspensions remains an active research field, and no unifying view has been proposed yet [119].
Here we consider neutrally buoyant (i.e. the fluid and particles density is essentially the same), chemically stable (nonaggregating) particles in a Newtonian fluid and we model it as isotropic inhomogeneous linear viscous fluid with effective viscosity that varies with concentration of the solid particles [9]

$$\boldsymbol{\tau} = -p\mathbf{I} + 2\mu(\phi)\mathbf{D}, \tag{3.6}$$

where the viscosity μ is a positive function of ϕ. When ϕ is uniform on the flow domain we recover the constitutive response of a Newtonian fluid. Conversely, when ϕ is not uniform the flow is inhomogeneous.
The dynamics of ϕ is governed by a simple advection equation in which any diffusive flux is ignored. In the framework of non-colloidal suspensions (the particles characteristic diameter is assumed to be sufficiently large for Brownian effects to be negligible), the solid-fluid interaction term depends on the Darcy's number [99, 32], which can become quite large being proportional to the square of the ratio between the macroscopic length scale and the particles size. Hence the two phases have practically the same velocity and the suspension can be considered as a single non-homogeneous fluid [4, 44, 75]. The dynamics of such a fluid is governed by

the equation of balance of linear momentum and the continuity equation for the fluid and by the advection equation for ϕ, which simply reduces to the material derivative equal to zero.

The viscosity of suspensions of solid particles in linear viscous liquids for the case of $\phi \leq 0.1$, is calculated by the well-known Einstein formula [33] dating back to 1906. Improvements to the Einstein formula are based on the work of Batchelor and Green [10, 11] and Batchelor [12]. In regimes where the average separation distance between particles is smaller than the particle size, multiple-body and short-range interactions give rise to strong non-Newtonian effects. This was first suggested by the dimensional analysis of Krieger [66, 67] and also confirmed by both experimental observations and numerical simulations.
As expected intuitively, suspension viscosity increases with the concentration, and in the dense regime, a divergence of viscosity is observed at a maximum packing fraction [24]. In particular, there have been numerous studies of suspension viscosity as a function of particle concentration and composition. So many theoretical and empirical models have resulted that it is difficult to find a unifying theme. Here we just mention to the recent review by Hund et. Al. [62] and to the numerous references therein reported.

In this thesis we will show how the formation of a marginal layer can be explained, in the context of the fluid dynamics of suspensions treated as inhomogeneous media, as an entrance effect, i.e. caused by to the particular flow profile that develops right at the vessel inlet. As a viscous fluid flows through a channel, the velocity profile undergoes a change from its initial entrance form to the familiar parabolic Poiseuille profile far downstream from the entrance [108]. In the inlet region (whose dimension is commonly referred to as entrance length) the pressure gradient differs from that in the region in which the flow is fully developed and the flow has a transverse component which then vanishes. However, this transverse component of velocity has a very important effect: it "pushes" the particles towards the channel center lowering ϕ near the vessel walls and so causing an increase in the inhomogeneity. Actually, the formation of a particle depleted layer close to the walls is one of the main distinctive flow properties of suspensions in vessels. Though several physical phenomena contribute to this behavior [114], little attention has been devoted the migration caused by peculiar flow that develops in the entry region. We believe that the knowledge of the suspensions entry flow behavior could turn out to be useful in investigating the particles migration towards the vessels central core.

More specifically, in the sequel we investigate how the "entrance effect" causes a particles migration away from vessel walls. In particular, considering an almost uniform inlet profile for ϕ, we want to analyze to what extent the transverse

velocity changes the profile itself, causing the so-called flow "marginalization". We also provide further insight into the influence of Reynolds number, particles size and effective viscosity on the particles migration away from the walls.

The intrinsic practical importance of understanding the hydrodynamical development of laminar flow in the entrance of a channel have been the motivation behind many theoretical, numerical and experimental investigations [19, 21, 27, 57, 69, 73, 106, 107, 108, 113, 117, 118]. All of them are based on the Prandtl approach but differ on the analysis of the mathematical problem. Some of them are based on the integral formulation of motion and continuity boundary layer equations, others consist in dividing the entrance region into two parts: boundary layer theory is applied to the first one, while the second one is treated by perturbing the velocity field. Further approaches appeal to inertial terms linearization. In this thesis, in order to treat the flow of a suspension, we construct a suitable generalization of the Langhaar method [69].

Particles migration towards the tube center is common in practical situations such as pressure-driven flow in tubes and channels. It has been quantified for the first time by Segré and Silberberg [112] who showed that at low Reynolds numbers a rigid sphere transported along in Poiseuille flow through a tube is subject to radial forces which tend to carry it to an equilibrium position at about 0.6 tube radii from the axis, irrespective of the radial position at which the sphere first entered the tube. The steady long-time decrease as well as the short-time increase in the effective viscosity of a concentrated suspension in a Couette viscometer was observed also by Gadala-Maria and Acrivos [48] and by Leighton and Acrivos [71], who argued that small-scale surface roughness of the particles leads to irreversible motion during interparticle interaction. We also mention the studies by Nott and Brady [86] who show that net irreversible migration is produced even when suspended particles are perfectly smooth hard spheres. In particular, they also estimate the channel length L in terms of its height and particle radius, for achieving steady state in the pressure-driven flow of a viscous suspension. Similar analysis have been performed by Hampton et al. [56], Phan-Thien and Fang [94] and in the recent paper by Lecampion and Garagash [70].

The earliest experimental study of inhomogeneous suspension have been conducted by Karnis et al. [64], who reported substantial blunting of the velocity profiles, by Koh et al. [65], whose Laser Doppler Velocimetry (LDV) experiments reveal considerable inhomogeneity in the particle concentration due to migration of particles towards the center of the channel. Other experimental studies have also confirmed the migration of particles from regions of high to low shear rate, Leighton and Acrivos [72], Abbott et al. [1], Sinton and Chow [115], Arp and Mason [6], Hookham [60] and Phan-Thien et al. [93]. Also the experiments performed in a biological context, have shown that in arteries terminal branches, arterioles and

venules (i.e. microcirculation) the red blood cells do not distribute uniformly on cross section [23, 28].
There are essentially two approaches for suspension flow, the diffusive flux model originally proposed by Leighton and Acrivos [71], and the "mixture" model. Diffusive flux models provide a kinematic description of the shear-induced particle migration in which the particle migration flux is expressed in terms of the gradients of the particle concentration and shear rate. This model was later applied by Phillips et al. [95] to pressure-driven suspension flow in tubes. However, as pointed out in [95], such a model predicts that in a steady Couette, or Poiseuille, flow the particles volume fraction attains a cusp at the centerline (never observed in experiments performed on suspensions) where it takes its maximum admissible value.
In the "mixture" model there are no diffusion considerations; rather mass, momentum, and energy balances are written for the particulate phase and the fluid phase (or for the solid phase and the entire suspension). Applying then the mass and momentum balance equations the particle migration is driven by the divergence of the normal stresses of the particle phase. Models of that kind have been recently developed by Monsorno et Al. [82, 83], Lecampion, Garagashp [70] and Boyer et Al. [20] and applied to confined pressure-driven laminar flow of neutrally buoyant non-Brownian suspensions [2]. Essentially they treat the suspension as a mixture [99, 32] and are characterized by considerable mathematical difficulties due to the boundary conditions. Indeed, one of the thorny obstacles when it comes to putting mixture theory in practice, is our inability to prescribe boundary conditions for stress boundary value problems, since we do not know how to distribute the traction (or compression) among the various mixture components.
In conclusion, we can state that adopting model (3.6), i.e. inhomogeneous fluid and no particles diffusion, we are able to obtain a simple model for the entrance flow of a suspension in a rectilinear channel. It is worth pointing out that our approach allows to evaluate the particles migration towards vessel center, at least when the inlet ϕ has a simple profile, solving a system of two autonomous ODE's, whose equilibrium solution provides the essential characteristics of the fully developed flow.

3.4 Governing equations

As an incompressible viscous fluid flows through a channel, the velocity profile undergoes a change from its initial entrance form to the familiar parabolic Poiseuille profile at an axial location far downstream from the entrance: that distance is commonly referred to as entrance length.
We consider a mechanically incompressible flow in a channel of amplitude $2H$ and

undefined length, but larger than H. We denote by x the longitudinal coordinate and by y the transversal one. The velocity field is

$$\boldsymbol{v} = u\boldsymbol{e}_x + v\boldsymbol{e}_y \ , \tag{3.7}$$

and, recalling (3.6), we set $\mu(\phi) = \mu_{ref}\mu(\phi)$, where μ_{ref} is a reference viscosity and $\mu(\phi)$ is dimensionless. The mathematical formulation of the problem is

$$\frac{\partial \phi}{\partial t} + \boldsymbol{v} \cdot \nabla \phi = 0, \tag{3.8}$$

$$\nabla \cdot \boldsymbol{v} = 0, \tag{3.9}$$

$$\rho\left(\frac{\partial \boldsymbol{v}}{\partial t} + (\boldsymbol{v} \cdot \nabla)\,\boldsymbol{v}\right) = -\nabla p + \mu_{ref}\nabla \cdot (2\mu(\phi)\mathbf{D})\,, \tag{3.10}$$

where ρ is the constant and uniform suspension density. Symmetry demands that u is even in y and v is odd, whereas the pressure and ϕ are even, provided the inlet profile is symmetric [124].
Phan-Thien and Fang in [94] consider in the r.h.s of (3.8) a diffusive flux of the solid phase $\boldsymbol{N}$, whose constitutive equation is the one of [95]. Such a system has been solved numerically using the finite volume method, widely used to solve convection-diffusion transport problems.
We rescale now the problem (3.8), (3.9), (3.10) with

$$\tilde{x} = \frac{x}{L}, \quad \tilde{y} = \frac{y}{H}, \quad \tilde{u} = \frac{u}{U}, \quad \tilde{v} = \frac{v}{V}, \quad \tilde{p} = \frac{p}{\rho U^2},$$

where U is the characteristic inlet velocity, $L = H\sqrt{\mathsf{Re}}$, with $\mathsf{Re} = \rho UH/\mu_{ref}$ is the Reynolds number which is assumed to be sufficiently large and $V = UH/L$. Setting

$$\alpha = \frac{1}{\sqrt{\mathsf{Re}}},$$

and neglecting "$\sim$"to keep notation as light as possible, we rewrite system (3.8)–(3.10) neglecting all terms $O(\alpha^n)$, $n \geq 2$. We thus get

$$\begin{cases} u\dfrac{\partial \phi}{\partial x} + v\dfrac{\partial \phi}{\partial y} = 0, \\ \\ \dfrac{\partial u}{\partial x} + \dfrac{\partial v}{\partial y} = 0, \\ \\ u\dfrac{\partial u}{\partial x} + v\dfrac{\partial u}{\partial y} = -\dfrac{\partial p}{\partial x} + \alpha\dfrac{\partial}{\partial y}\left(\mu(\phi)\dfrac{\partial u}{\partial y}\right) \\ \\ \dfrac{\partial p}{\partial y} = 0, \qquad \Longrightarrow \qquad p = p(x). \end{cases} . \tag{3.11}$$

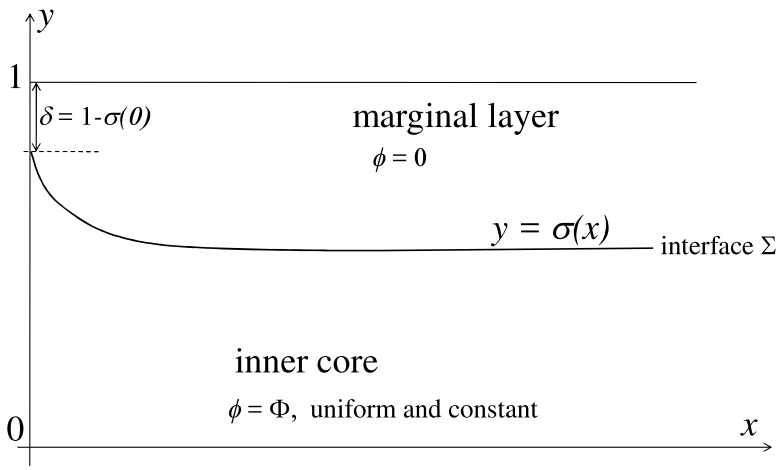

Figure 3.2: A schematic drawing of the geometrical model.

Here we consider a simpler version of (3.11), assuming that the inlet velocity is uniform on the cross section

$$u\left(0,y\right)=1, \qquad v\left(0,y\right)=0,$$

and the inlet solid volume fraction is

$$\phi_{in}(y)=\begin{cases}\Phi, & 0\leq y\leq 1-\delta,\\ 0, & 1-\delta<y\leq 1,\end{cases} \tag{3.12}$$

with Φ constant and $\delta = H/a$, where a is the particle radius. The reason of such a distribution is essentially geometrical. The finite size of particles limits the radial distribution of their centers. Indeed, for sphere-like practicles the center of mass cannot physically approach within a certain length of the wall. Hence, a particles-depleted layer, whose dimensionless thickness is $\mathcal{O}\left(\delta\right)$, forms close to the wall.
Starting from $x = 0$, our aim is to evaluate the evolution of such a particles depleted layer. If its amplitude grows with x, then the particles migrate towards the tube center. So, focussing only in the upper half of the canal for reasons of symmetry, we denote by Σ the interface[3] between the marginal layer and the inner core, see Fig. 3.2, whose equation is

$$y=\sigma\left(x\right), \qquad \text{with} \qquad \sigma(0)=1-\delta,$$

The interface Σ is the material curve being the flow line starting from $(0, 1-\delta)$, and therefore its equation is

$$-u(x,\sigma(x))\sigma'(x)+v(x,\sigma(x))=0.$$

[3]Actually Σ is a free boundary since its position is unknown.

So Σ splits the channel into two regions: the marginal layer in which $\phi = 0$ and the inner core where $\phi \equiv \Phi$ (see again Fig. 3.2). Hence the dimensionless viscosity is

$$\mu = \begin{cases} \mu(\Phi), & 0 \le y \le \sigma, \\ 1, & \sigma < y \le 1. \end{cases} \tag{3.13}$$

We have two different Prandtl systems, matched together with suitable boundary conditions obtained imposing continuity of velocity and normal stress [26]. So, denoting by $[\![\cdot]\!]$ the jump of the quantity $(\cdot)$ across Σ and writing μ in place of $\mu(\Phi)$, the final formulation of the free boundary problem is the following:
Inner Region, $0 \le y < \sigma$

$$\begin{cases} \dfrac{\partial u}{\partial x} + \dfrac{\partial v}{\partial y} = 0, & x \ge 0, \quad 0 \le y < \sigma(x), \\ u\dfrac{\partial u}{\partial x} + v\dfrac{\partial u}{\partial y} = -\dfrac{\partial p}{\partial x} + \alpha\mu\dfrac{\partial}{\partial y}\left[\dfrac{\partial u}{\partial y}\right], & x \ge 0, \quad 0 \le y < \sigma(x), \\ p = p(x), & x \ge 0, \\ \dfrac{\partial u}{\partial y} = 0, \qquad v = 0, & x \ge 0, \quad y = 0, \\ u = 1, \qquad v = 0, & x = 0, \quad 0 \le y \le 1 - \delta. \end{cases} , \tag{3.14}$$

System (3.14) is nothing more that Prandtl equation, i.e. system (3.11), where to keep notation as light as possible we set $\mu(\phi) = \mu$ (3.13).

Outer region, $\sigma < y \le 1$

$$\begin{cases} \dfrac{\partial u}{\partial x} + \dfrac{\partial v}{\partial y} = 0, & x \ge 0, \quad \sigma(x) < y \le 1, \\ u\dfrac{\partial u}{\partial x} + v\dfrac{\partial u}{\partial y} = -\dfrac{\partial p}{\partial x} + \alpha\dfrac{\partial^2 u}{\partial y^2}, & x \ge 0, \quad \sigma(x) < y \le 1, \\ p = p(x), & x \ge 0, \\ u = 0, \qquad v = 0, & x \ge 0, \quad y = 1, \\ u = 1, \qquad v = 0, & x = 0, \quad 1 - \delta < y \le 1. \end{cases} . \tag{3.15}$$

System (3.15) is the Prandtl equation (3.11) with $\mu = 1$, because of (3.13).

Free boundary Σ, $y = \sigma(x)$

$$\begin{cases} -u(x,\sigma(x))\sigma'(x) + v(x,\sigma(x)) = 0, \\ [\,u\,] = 0, \\ [\,v\,] = 0, \\ [\,p\,] = 0, \\ \mu \left.\dfrac{\partial u}{\partial y}\right|_{y=\sigma^-} = \left.\dfrac{\partial u}{\partial y}\right|_{y=\sigma^+}, \\ \sigma(0) = \sigma_0 = 1 - \delta. \end{cases} \tag{3.16}$$

Σ is a material surface whose equation is therefore given by $(3.16)_1$, usually called kinematics condition. The other equations in system (3.16) represent the continuity of velocity and stress across Σ.

While the transversal velocity v vanishes as $x \to \infty$, the longitudinal-one velocity develops from the entrance flat profile to a "final" Poiseuille-like profile which, setting $\sigma_\infty = \lim_{x\to\infty} \sigma(x)$, is given by

$$u_\infty = \begin{cases} \dfrac{3}{2}\dfrac{\mu}{\sigma_\infty^3 + \mu(1-\sigma_\infty^3)}(1-y^2), & \sigma_\infty \le y \le 1 \\ \dfrac{3}{2}\dfrac{\mu}{\sigma_\infty^3 + \mu(1-\sigma_\infty^3)}\left(1 - \sigma_\infty^2 + \dfrac{\sigma_\infty^2 - -y^2}{\mu}\right), & 0 \le y < \sigma_\infty. \end{cases} \tag{3.17}$$

We have already remarked that Σ is the material curve. Hence

$$\int_0^{\sigma_0} u(0,y)\,dy = \int_0^{\sigma_\infty} u_\infty(y)\,dy,$$

so that σ_0 and σ_∞ are linked through (see also Fig. 3.5 in Section 3.6)

$$\sigma_0 = \frac{3}{2}\frac{\mu}{\sigma_\infty^3 + \mu(1-\sigma_\infty^3)}\left[\sigma_\infty + \sigma_\infty^3\left(\frac{2}{3\mu} - 1\right)\right]. \tag{3.18}$$

We easily realize that $\sigma_0 \to 1$ as $\sigma_\infty \to 1$, i.e. as $\delta \to 0$, regardless of μ, meaning that the amplitude of the particle-free layer remains practically unchanged in those

vessels whose radius is much larger than the particles radius a. Next, (3.18) clearly states that σ_∞ depends only on μ and σ_0: the Reynolds number does not play any role. We however remark that equation (3.18) simply provides the link between the initial and asymptotic radius of the core, but it does not give any information on the behavior of $\sigma(x)$. The solution to (3.14)-(3.15) will provide $\sigma(x)$. In particular, we will be able to estimate the influence of Reynolds number on the decay of $\sigma(x)$ towards the asymptotic value σ_∞.

3.5 Approximate solution

It is not possible to solve analytically problem (3.14)-(3.15) as it stands, but we shall now look for an approximate solution fulfilling the mass conservation and momentum balance to secure the physical consistency of the theory, i.e.

$$\begin{cases} \dfrac{d}{dx}\displaystyle\int_0^1 u(x,y)dy = 0, \\ \\ \dfrac{d}{dx}\displaystyle\int_0^1 u^2(x,y)dy = -p'(x) + \alpha \left.\dfrac{\partial u}{\partial y}\right|_{y=1}. \end{cases} \tag{3.19}$$

In particular $(3.19)_1$ represents the continuity equation, i.e. the discharge is the same in any cross section. To justify $(3.19)_2$ we combine the Prandtl equation and the continuity equation, obtaining

$$\frac{\partial u^2}{\partial x} + \frac{\partial}{\partial y}(uv) = -p'(x) + \alpha\frac{\partial^2 u}{\partial y^2}.$$

Then, integrating both sides over the interval $0 \le y \le 1$ and using the boundary conditions, we get $(3.19)_2$.

Our starting point is the method developed in [69] and also illustrated in in Chapter 16 of [68]. We linearize the terms of inertia through an auxiliary function β, which is assumed to depend only on x. The generalization that we propose here consists in treating the outer and inner regions separately and then use the boundary conditions $(3.16)_2$-$(3.16)_4$ to find the global solution.

Let us start with the outer region and introduce

$$\kappa_{outer} = u\frac{\partial u}{\partial x} + v\frac{\partial u}{\partial y} + p(x) - \alpha\beta^2 u, \qquad \sigma \le y \le 1, \tag{3.20}$$

where $\beta = \beta(x)$ is unknown at this stage. We then assume that $\kappa_{outer} = \kappa_{outer}(x)$ and, after substituting (3.21) into $(3.15)_2$ we obtain

$$\alpha\frac{\partial^2 u}{\partial y^2} = \alpha\beta^2 u + \kappa_{outer}(x),$$

whose symmetric solution, imposing $(3.15)_4$, is

$$u(x,y) = C\left[\cosh(\beta y) - \cosh\beta\right],$$

where $C = C(x)$ has yet to be determined.
Proceeding in a similar way in the inner region, we introduce[4]

$$\kappa_{inner} = u\frac{\partial u}{\partial x} + v\frac{\partial u}{\partial y} + p(x) - \alpha\beta^2 u, \qquad 0 \le y < \sigma,$$

still assuming $\kappa_{inner} = \kappa_{inner}(x)$, and rewrite $(3.14)_2$ in this way

$$\mu\alpha\frac{\partial^2 u}{\partial y^2} = \alpha\beta^2 u + \kappa_{inner}(x),$$

whose symmetric solution is

$$u(x,y) = D\cosh\left(\frac{\beta}{\sqrt{\mu}}y\right) - \frac{\kappa_{inner}}{\alpha\beta^2}.$$

with $D = D(x)$ being arbitrary. We then use $(3.16)_2$ and $(3.16)_5$ to express D and κ_{inner} in terms of $C(x)$, getting

$$u = \begin{cases} C\ F_{out}(y,\beta), & \sigma < y < 1, \\ \\ C\ F_{in}(y,\beta,\sigma), & 0 < y < \sigma. \end{cases} \tag{3.21}$$

where

$$F_{out}(y,\beta) = \cosh(\beta y) - \cosh\beta\ , \tag{3.22}$$

and

$$F_{in}(y,\beta,\sigma) = \frac{\sinh(\beta\sigma)}{\sqrt{\mu}\sinh\left(\frac{\beta\sigma}{\sqrt{\mu}}\right)}\left[\cosh\left(\frac{\beta y}{\sqrt{\mu}}\right) - \cosh\left(\frac{\beta}{\sqrt{\mu}}\right)\right]$$
$$+\cosh(\beta\sigma) - \cosh\beta. \tag{3.23}$$

Finally, to determine C we exploit $(3.19)_1$ getting

$$C(\beta,\sigma) = \left\{\frac{\sinh\beta - \sinh(\beta\sigma)}{\beta} + \sigma\cosh(\beta\sigma) - \cosh\beta + \right.$$
$$\left. + \frac{\sinh(\beta\sigma)}{\sqrt{\mu}\sinh\left(\frac{\beta\sigma}{\sqrt{\mu}}\right)}\left[\frac{\sqrt{\mu}}{\beta}\sinh\left(\frac{\beta\sigma}{\sqrt{\mu}}\right) - \sigma\sqrt{\mu}\cosh\left(\frac{\beta\sigma}{\sqrt{\mu}}\right)\right]\right\}^{-1}. \tag{3.24}$$

[4]Following strictly the Langhaar approach we should assume that $\kappa_{outer} = \kappa_{inner} = 0$, but that is not fulfilled by the solution.

To check the compatibility with the asymptotic behavior (3.17). We assume $\lim_{x\to\infty}\beta(x) = 0$ and $\lim_{x\to\infty}\sigma(x) = \sigma_\infty$ and expanding (3.23) and (3.24) as $x \to \infty$, we have

$$u = \begin{cases} -\dfrac{C\beta^2}{2}\left(1-y^2\right), & \sigma_\infty \le y \le 1, \\ -\dfrac{C\beta^2}{2}\left(1-\sigma_\infty^2+\dfrac{\sigma_\infty^2--y^2}{\mu}\right), & 0 \le y < \sigma_\infty. \end{cases}$$

On the other hand from (3.25) we obtain

$$\lim_{x\to\infty} C = -\frac{3}{\beta^2}\frac{\mu}{\sigma_\infty^3+\mu\left(1-\sigma_\infty^3\right)},$$

and so (3.17) is recovered.
To write explicitly the equation for σ, i.e. $(3.16)_1$, we need v that we recover from the continuity equation, namely $v = \int_y^1 \frac{\partial u}{\partial x}dy'$. So $(3.16)_1$ rewrites

$$\sigma' = \frac{\int_\sigma^1 \frac{\partial u}{\partial x}dy}{u(x,\sigma)}. \tag{3.25}$$

Recalling now (3.22), (3.23) and (3.25), we can rewrite (3.26) as

$$\sigma' = \frac{\int_\sigma^1 \left[\left(\frac{\partial C}{\partial\beta}\beta' + \frac{\partial C}{\partial\sigma}\sigma'\right)F_{out} + C\frac{\partial F_{out}}{\partial\beta}\beta'\right]dy}{CF_{out}},$$

which, after some manipulations, becomes

$$\sigma' = Q(\beta,\sigma)\,\beta', \tag{3.26}$$

where

$$Q(\beta,\sigma) = \frac{\frac{\partial C}{\partial\beta}\mathcal{F}_1 + C\mathcal{F}_2}{CF_{out} - \frac{\partial C}{\partial\sigma}\mathcal{F}_1}, \tag{3.27}$$

with

$$\begin{aligned} \mathcal{F}_1(\beta,\sigma) &= \int_\sigma^1 F_{out}(\beta,y)\,dy \\ &= \frac{\sinh\beta - \sinh\beta\sigma}{\beta} - (1-\sigma)\cosh\beta, \end{aligned}$$

and

$$\begin{aligned}\mathcal{F}_2(\beta,\sigma) &= \int_\sigma^1 \frac{\partial F_{out}}{\partial \beta} dy \\ &= (\sigma-1)\sinh\beta + \frac{\cosh\beta - \sigma\cosh(\beta\sigma)}{\beta} + \frac{\sinh(\beta\sigma)-\sin\beta}{\beta^2}.\end{aligned}$$

What remains is to determine the equation for β from momentum balance $(3.19)_2$. Following [69], we compute p' through $(3.14)_2$ evaluated in $y=0$, and so obtain

$$2\int_0^1 u\frac{\partial u}{\partial x}dy = \left[u\frac{\partial u}{\partial x} - \alpha\mu\frac{\partial^2 u}{\partial y^2}\right]_{y=0} + \alpha\left.\frac{\partial u}{\partial y}\right|_{y=1}. \tag{3.28}$$

Starting from the l.h.s. we have

$$\begin{aligned}&2\int_0^1 u\frac{\partial u}{\partial x}dy = 2\left[\int_0^\sigma CF_{in}\frac{\partial(CF_{in})}{\partial x}dy + \int_\sigma^1 CF_{out}\frac{\partial(CF_{out})}{\partial x}dy\right] \\ &= 2\left\{C\left(\frac{\partial C}{\partial\beta}\beta' + \frac{\partial C}{\partial\sigma}\sigma'\right)(\mathcal{K}_1+\mathcal{K}_3) + C^2\left[\beta'(\mathcal{K}_2+\mathcal{K}_4)+\sigma'\mathcal{K}_5\right]\right\},\end{aligned}$$

where

$$\begin{aligned}\mathcal{K}_1 &= \int_\sigma^1 F_{out}^2 dy, \quad \mathcal{K}_2 = \int_\sigma^1 F_{out}\frac{\partial F_{out}}{\partial\beta}dy, \\ \mathcal{K}_3 &= \int_0^\sigma F_{in}^2 dy, \quad \mathcal{K}_4 = \int_0^\sigma F_{in}\frac{\partial F_{in}}{\partial\beta}dy, \quad \mathcal{K}_5 = \int_0^\sigma F_{in}\frac{\partial F_{in}}{\partial\sigma}dy.\end{aligned}$$

The explicit expressions of $\mathcal{K}_i$, $i=1,2,3,4,5$, computed with the aid of the computer software MAXIMA® [76], are displayed in the Appendix. Focussing then on the r.h.s of (3.29) we identify 3 terms, for which we give here the explicit expression:

- First term on the r.h.s of (3.29), $u\frac{\partial u}{\partial x}\big|_{y=0}$

$$\left.u\frac{\partial u}{\partial x}\right|_{y=0} = C\left(\frac{\partial C}{\partial\beta}\beta' + \frac{\partial C}{\partial\sigma}\sigma'\right)\mathcal{W}_3 + C^2(\beta'\mathcal{W}_4 + \sigma'\mathcal{W}_5)$$

  where

$$\mathcal{W}_3 = \left.F_{in}^2\right|_{y=0}, \quad \mathcal{W}_4 = \left.F_{in}\frac{\partial F_{in}}{\partial\beta}\right|_{y=0}, \quad \mathcal{W}_5 = \left.F_{in}\frac{\partial F_{in}}{\partial\sigma}\right|_{y=0}.$$

  Again, the explicit expressions of $\mathcal{W}_i$, $i=3,4,5$ are showed in the Appendix.

- Second term on the r.h.s of (3.29), $-\alpha\mu\frac{\partial^2 u}{\partial y^2}\Big|_{y=0}$

$$-\alpha\mu\frac{\partial^2 u}{\partial y^2}\bigg|_{y=0} = -\alpha\mu C\,\frac{\partial^2 F_{in}}{\partial y^2}\bigg|_{y=0} = -\alpha C\beta^2\frac{\sinh(\beta\sigma)}{\sqrt{\mu}\sinh\left(\frac{\beta\sigma}{\sqrt{\mu}}\right)}\,.$$

- Third term on the r.h.s of (3.29), $\alpha\,\frac{\partial u}{\partial y}\Big|_{y=1}$

$$\alpha\,\frac{\partial u}{\partial y}\bigg|_{y=1} = \alpha C\beta\sinh\beta\,.$$

So inserting the above expressions in (3.29) and recalling (3.27), (3.28) we have

$$\beta' = \frac{N(\beta,\sigma)}{D(\beta,\sigma)},$$

where

$$N = \alpha C\left[\beta\sinh\beta - \beta^2\frac{\sinh(\beta\sigma)}{\sqrt{\mu}\sinh\left(\frac{\beta\sigma}{\sqrt{\mu}}\right)}\right],$$

$$\begin{aligned} D &= C\left(\frac{\partial C}{\partial\beta}+\frac{\partial C}{\partial\sigma}Q\right)\left[2\left(\mathcal{K}_1+\mathcal{K}_3\right)-\mathcal{W}_3\right]+ \\ &\quad +C^2\left[2\left(\mathcal{K}_2+\mathcal{K}_4\right)-\mathcal{W}_4\right]+C^2Q\left[2\mathcal{K}_5-\mathcal{W}_5\right]. \end{aligned}$$

Ultimately we come to the following ODE system

$$\begin{cases} \beta' = \dfrac{N(\beta,\sigma)}{D(\beta,\sigma)}, \\[2ex] \sigma' = \dfrac{N(\beta,\sigma)}{D(\beta,\sigma)}Q(\beta,\sigma)\,, \end{cases} \tag{3.29}$$

which has to be supplemented with suitable "initial" conditions. While $\sigma(0)=\sigma_0$ is well defined, we know from the standard theory (Chapter 16 of [68]) that β diverges as $x\to 0$. Hence, we prefer focusing on $x\to\infty$ (which reads as $x = n\sqrt{\mathsf{Re}}$, with $n\gg 1$) where $\beta\to 0$, and $\sigma\to\sigma_\infty$, which can be expressed in terms of σ_0 (the actually available datum) inverting (3.18).

3.6 Numerical simulations

To check the numerical solver, but also the model, we compare the solution to (3.30) when $\mu = 1$ with the classical Langhaar solution. Indeed, when $\mu = 1$, we are dealing with a homogeneous flow and the curve $y = \sigma(x)$ represents the flow line staring from $(0, \sigma_0)$.
According to the Langhaar theory the equation for $\beta(x)$ is

$$\frac{1}{\alpha}\frac{\partial}{\partial x}S(\beta(x)) = -H(\beta(x)), \tag{3.30}$$

where

$$S = \frac{\dfrac{1}{\cosh(\beta)} - \dfrac{3}{2}\dfrac{\tanh(\beta)}{\beta} + \dfrac{1}{2}}{\left(1 - \dfrac{\tanh(\beta)}{\beta}\right)^2},$$

$$H = \beta^2 \left(\frac{1 - \dfrac{1}{\cosh(\beta)}}{1 - \dfrac{\tanh(\beta)}{\beta}} - 1 \right).$$

The equation for σ is still given by $(3.16)_1$ where now

$$u(x, y) = \frac{1 - \dfrac{\cosh(\beta y)}{\cosh\beta}}{1 - \dfrac{\tanh\beta}{\beta}},$$

while v, i.e. the transversal velocity, has a more complicated expression[5] that we are not reporting here. Fig.s 3.3, 3.4 display the difference between β and σ computed using system (3.30) with $\mu = 1$ and the ones coming from the Langhaar theory [69]. This difference is in the order of magnitude of 10^{-5} at maximum (see left panel of Fig.3.3), implying that both model (3.30) and the numerical solver are very accurated.
Figure 3.5 displays $\sigma_\infty(\sigma_0)$ obtained inverting (3.18), for $\mu = 1,\ 5,\ 10,\ 15,\ 20$. Actually, since $\mu = \mu(\Phi)$, Fig. 3.5 shows that the largest migration occurs when the suspension is very diluted, i.e. $\mu \sim 1$. A "large" Φ, that is a "large" μ, reduces the marginalization. The latter depends on the particles radius a trough $\sigma_0 = 1 - a/H$ (provided is finite).
The widening of the marginal layer (as a consequence of the particles migration towards the center) is highlighted in Fig. 3.6, where, still exploiting (3.18),

[5] v can be determined after some algebra from the continuity equation.

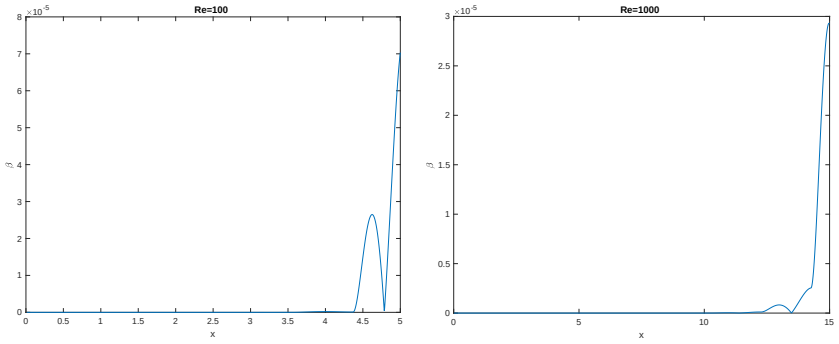

Figure 3.3: Difference between $\beta(x)$ computed using (3.30) with $\mu = 1$ and the one computed using (3.31), for $\mathsf{Re} = 10^2$, and $\mathsf{Re} = 10^3$.

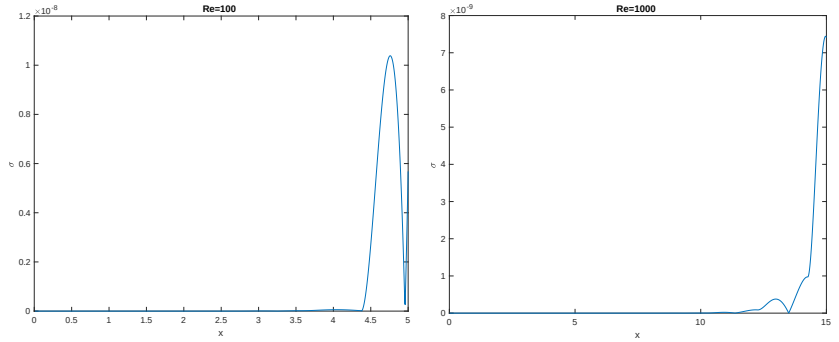

Figure 3.4: Difference between $\sigma(x)$ computed using (3.30) with $\mu = 1$ and the one computed using the classical Langhaar solution [69], for $\mathsf{Re} = 10^2$, and $\mathsf{Re} = 10^3$.

$\delta_\infty = 1 - \sigma_\infty$ is plotted versus $\delta_0 = 1 - \sigma_0$. In particular, as μ increases the dependence of δ_∞ on μ vanishes, as evident from (3.18). Therefore, for a given marginal layer inlet amplitude δ_0, there exists a maximum value towards which δ_∞ tends asymptotically as $\mu \to \infty$. We also note that each curve $\delta_\infty(\delta_0)$, although monotonously increasing, is concave. In fact, the largest increase in the particle-free layer amplitude occurs for small values of δ_0. Considering, for instance $\mu = 1$, we have $\delta_\infty(0.1) \sim 0.275$, i.e. the marginal layer has more than doubled, while $\delta_\infty(0.2) \sim 0.39$.

In Fig. 3.7 the behavior of $\sigma(x)$ for different values of Re, μ and σ_0 is reported. The numerical data obtained show that the flow indubitably stabilizes in a core-annulus configuration and that the lowest is μ the largest is the particles drifting towards the center, as in Fig. 3.5. Actually, the curves showed in Fig. 3.7 provide a "visual" explanation of migration occurring just in the entrance region. Indeed, the transversal velocity drives the particles away from the vessel walls (thus enlarging

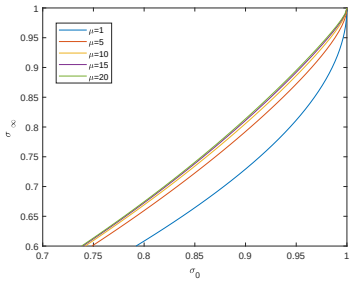

Figure 3.5: Behavior of $\sigma_\infty(\sigma_0)$ given by (3.18) for $\mu = 1, 5, 10, 15, 20$.

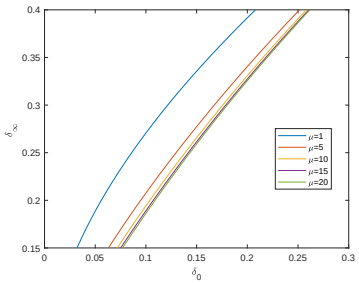

Figure 3.6: Behavior of $\delta_\infty = 1 - \sigma_\infty$ as a function of $\delta_0 = 1 - \sigma_0$, inlet marginal layer width, for $\mu = 1, 5, 10, 15, 20$.

the marginal layer) within the inlet region, while has no effect far downstream (where it vanishes). This therefore explains either the particular structure of the asymptotic flow and the particles migration towards the center (migration caused by the peculiar structure of the flow in the entrance region).
As expected, Re has no influence on the radius of the asymptotic inner core σ, but just on the extension of the entrance region, which increases as Re increases (as in the classic entrance flow theory).

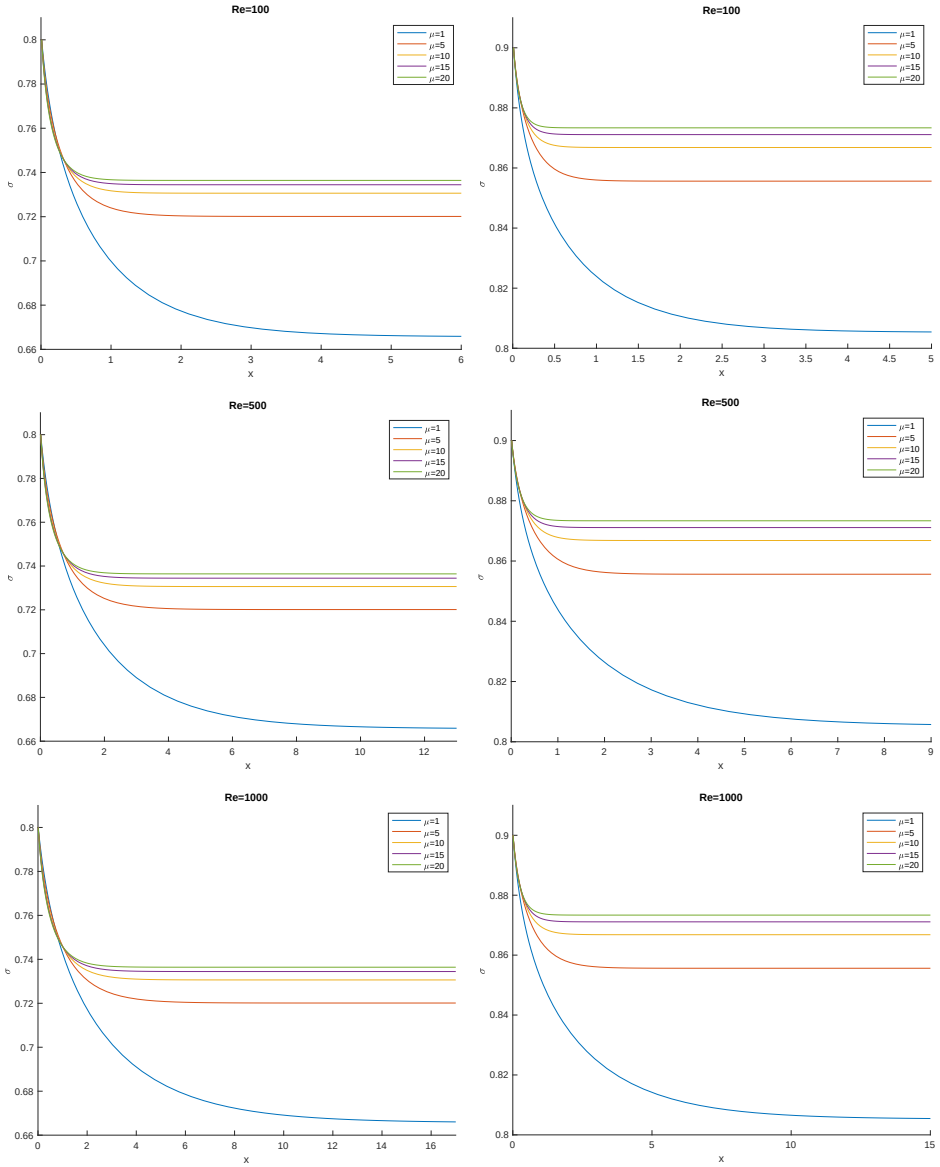

Figure 3.7: Behavior of $\sigma(x)$ for $\mathsf{Re} = 100$, 500, 1000, and finite σ_0. In particular, $\sigma_0 = 0.8\,, 0.9$. For each case five value of μ have been considered.

3.7 Final remarks

The formation of a low particles concentration layer near the walls of the vessel is one of the distinctive flow properties of suspensions in tubes. Though several physical phenomena contribute to the particles migration, a general mechanistic understanding of this effect has proved elusive.
In this chapter, we have faced up to a very important and still unexplained phenomenon, as mentioned before, occurring in microcirculation: the Fåhraeus-Lindqvist effect. Such an effect was discovered almost a hundred years ago and it has signed the history of hemodynamics due to the inability of the scientific community to find a satisfactory fluid dynamical explanation for it. Nowadays, the only step which is universally accepted towards this goal is Haynes interpretation, according to which the Fåhraeus-Lindqvist effect is caused by the formation of a RBCs-depleted layer close to the wall of blood vessels smaller than $300\mu m$ in diameter. In other words, in blood vessels of more or less these dimensions, RBCs tend to accumulate in the middle zone and this leads to the formation of a central RBCs-containing core which is surrounded by a plasma layer. However, in fluid dynamics nobody has ever succeeded in understanding why such a layer forms. This is the crux of the problematic role which is played by the Fåhraeus-Lindqvist effect in hemodynamics. As we discussed in Section 3.2, many hypothesis have been proposed through the years to justify the RBCs migration towards the blood vessel cross section, but all of them, while reasonable, proved insufficient. Moreover, they whole consisted in numerical simulations: a mathematical model being able to explain the Fåhraeus-Lindqvist effect has never been developed. We have tried to fill this lack by proposing an original approach. We have indeed built a mathematical model and applied the Prandtl boundary layer equations for the channel entrance flow. In previous Sections, considering an inhomogeneous flow model, namely equations (3.6), (3.8)-(3.10), we have investigated to what extent the peculiar velocity field that develops at the vessel inlet causes the particles migration towards the center, inducing a larger flow inhomogeneity.
To investigate qualitatively and quantitatively this phenomenon, we considered a "step" particles distribution at the vessel inlet setting $\phi = 0$ in a layer close to the wall (whose amplitude is related to the particles radius) and ϕ constant elsewhere. This profile finds its physical justification in the so-called "size exclusion effect": the suspended particles cannot approach the wall without their radius.
We therefore tackled the study of migration, also known as marginalization, in the development of a model for the central core radius $\sigma(x)$. The longitudinal evolution of σ not only provides a "visual" explanation of the particles migration, but also allows for an estimate of the influence played by the main physical and geometric quantities characterizing the flow. To this aim, we generalized the entrance flow theory developed in the 1940s by Langhaar [69], considering a typi-

cal core-annulus structure. The mathematical problem results in the autonomous system (3.30) for the auxiliary function β and the interface σ, which we solved numerically. The results showed that the flow attains downstream a steady configuration. In particular, we highlighted that migration is more evident the more the suspension is diluted. In fact, a "large" viscosity (which obviously occurs when the suspension is concentrated) reduces the particles radial drift, i.e. the marginal layer widening. The latter depends also on the particles size, provided the ration between the particles radius a and the channel half-amplitude H is finite.
The Reynolds number does not affect the asymptotic core radius but strongly influences the length of the entrance region.
Our model, despite its limitations, has therefore shown that in rectilinear flows the movement of the particles towards the duct axis can also be explained as an entrance effect, i.e. in terms of the transversal velocity occurring in the entrance region.

Chapter 4

Use of viscoplastic models in microcirculation

4.1 Vasomotion

Blood vessels equipped with smooth muscle cells may undergo radial oscillation that are independent of heart pulsation or respiratory rhythm, and have indeed a different frequency. This phenomenon, called vasomotion, is more pronounced, in terms of frequency and relative amplitude, at the level of the vessels characterized by a large pressure drop, and as a matter of fact it has been studied more intensively for arterioles and venules, for which frequency can reach 25 cpm and amplitude can peak to 100% of mean diameter [63]. Despite a quite numerous literature on vasomotion physiology, its influence on microcirculation is still a matter of debate. In venules there is no doubt that vasomotion favors blood flow, thanks to the action of valves [36]. However in [80] and in [53] are provided clues for opposite interpretations argument in terms of arterioles resistance. In [31] the authors, experimenting with bat wings, provided new evidence that venules vasomotion acts as a pump, enhancing blood flow, thus supporting the old claim by Jones in quantitative terms. Anyway, we emphasize that venules valves, preventing backflow, produce a scenario which differs substantially from the one observed in arterioles [38]. In [36] and [38] the rheological model proposed to describe blood flow was the Newtonian one. This is undoubtedly not useful to our approach because, as illustrated above, we are modeling the microcirculation flows. In this chapter we propose a first attempt to improve the model, considering a more appropriate rheological model such as the Casson model. We will then develop a model for the peristaltic flow of a Casson fluid. This problem is completely original. In fact, as regards the Casson flow, in the literature there is no theoretical study concerning neither the peristaltic flow nor the flow in a channel with non-flat walls. We will

therefore first tackle the study of the Casson flow in a channel with non-flat walls and then the study of the flow guided by the motion of the walls (peristaltic flow).

Concerning Casson flows most of the efforts in the theoretical analyses focus on the extent and the shape of yielded/unyielded regions, which are the main feature of viscoplastic materials. A possible approach is the one introduced in [45, 46] where the equation of motion of the unyielded part is written in an integral form. According to this method, originally developed by Safronchik [105], the unyielded region is treated as a rigid body of variable mass whose dynamics is governed by the cardinal equations. We remark that the yield surface can be determined using other methods, such as the ones illustrated in [43, 84, 85, 97].
In this chapter we focus on the Casson model and analyze the flow in a symmetric channel with "small" aspect ratio so that the lubrication approximation can be safely used. We analyze the dynamics considering two conditions driving the flow: prescribed inlet-outlet pressure difference and peristaltic motion. The case of prescribed inlet discharge has been already analyzed in [47]. We investigate also the conditions ensuring that the inner plug does not come in touch with the walls. Peristaltic flow (for which walls are set in motion by a traveling velocity profile) is studied because of their great importance in understating artery and vein physiology [36, 39].

4.2 Mathematical model

The constitutive equation for a Casson fluid is given by (2.21)
We investigate the 2D flow in a channel as the one depicted in Fig. 4.1. The x axis coincides with the channel symmetry line and $y = \pm h(x)$ are the channel walls. The velocity field is given by

$$\boldsymbol{v}(x, y, t) = u(x, y, t)\boldsymbol{e}_1 + v(x, y, t)\boldsymbol{e}_2.$$

The yielded part of the flow, i.e. $|\boldsymbol{\tau}| \geqslant \tau_o$, and the unyielded part, i.e. $|\boldsymbol{\tau}| \leqslant \tau_o$, are separated by the sharp interfaces $y = \pm\sigma(x, t)$. Because of symmetry we may confine our analysis only to the upper part of the channel.
The motion of the unyielded region (schematically depicted in Fig. 4.2)

$$\Omega_t = \{(x, y) : \quad 0 \leq x \leq L,\ 0 \leq y \leq \sigma(x, t)\},$$

obeys to the equation of balance of linear momentum that we write in an integral form [37]

$$\int_{\Omega_t} \frac{\partial}{\partial t}(\rho\boldsymbol{v})dV + \int_{\partial\Omega_t} \rho\boldsymbol{v}(\boldsymbol{v}\cdot\boldsymbol{n})dS = \int_{\partial\Omega_t} \boldsymbol{\tau}\boldsymbol{n}dS, \tag{4.1}$$

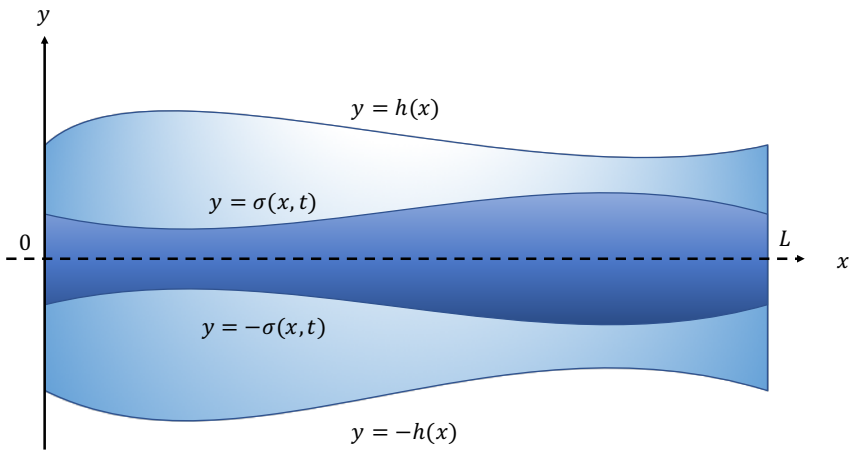

Figure 4.1: Flow in a symmetric channel with curved walls. The yielded region $|\boldsymbol{\tau}| \geqslant \tau_o$, and the unyielded one $|\boldsymbol{\tau}| \leqslant \tau_o$ are separated by a sharp interface $y = \pm\sigma(x,t)$.

where $\boldsymbol{n}$ is the normal to Ω_t pointing outward. In the yielded region $\sigma \leqslant y \leqslant h$ the governing equations of the system

$$\begin{cases} \dfrac{\partial u}{\partial x} + \dfrac{\partial v}{\partial y} = 0, \\ \rho\left(\dfrac{\partial u}{\partial t} + \dfrac{\partial u}{\partial x}u + \dfrac{\partial u}{\partial y}v\right) = -\dfrac{\partial p}{\partial x} + \dfrac{\partial \tau_{11}}{\partial x} + \dfrac{\partial \tau_{12}}{\partial y}, \\ \rho\left(\dfrac{\partial v}{\partial t} + \dfrac{\partial v}{\partial x}u + \dfrac{\partial v}{\partial y}v\right) = -\dfrac{\partial p}{\partial y} + \dfrac{\partial \tau_{12}}{\partial x} + \dfrac{\partial \tau_{22}}{\partial y}, \end{cases} \tag{4.2}$$

where body forces have been neglected. In the unyielded part, because of symmetry, the motion is a pure translation and the velocity is given by

$$\boldsymbol{v} = u_c(t)\boldsymbol{e}_1,$$

To write the equations of the unyielded part component-wise we look at Fig. 4.2 where the boundary $\partial\Omega_t$ has been divided into 4 components

$$\partial\Omega_t = \mathcal{F}_1 \cup \mathcal{F}_2 \cup \mathcal{F}_3 \cup \mathcal{F}_4 \ .$$

The first component of equation (4.1) is given by

$$\frac{\partial}{\partial t}(\rho u_c)\int_{\Omega_t} dV + \rho u_c^2 \int_{\partial\Omega_t} (\boldsymbol{e}_1 \cdot \boldsymbol{n}) dS = \int_{\partial\Omega_t} (\boldsymbol{\tau}\boldsymbol{n} \cdot \boldsymbol{e}_1) dS, \tag{4.3}$$

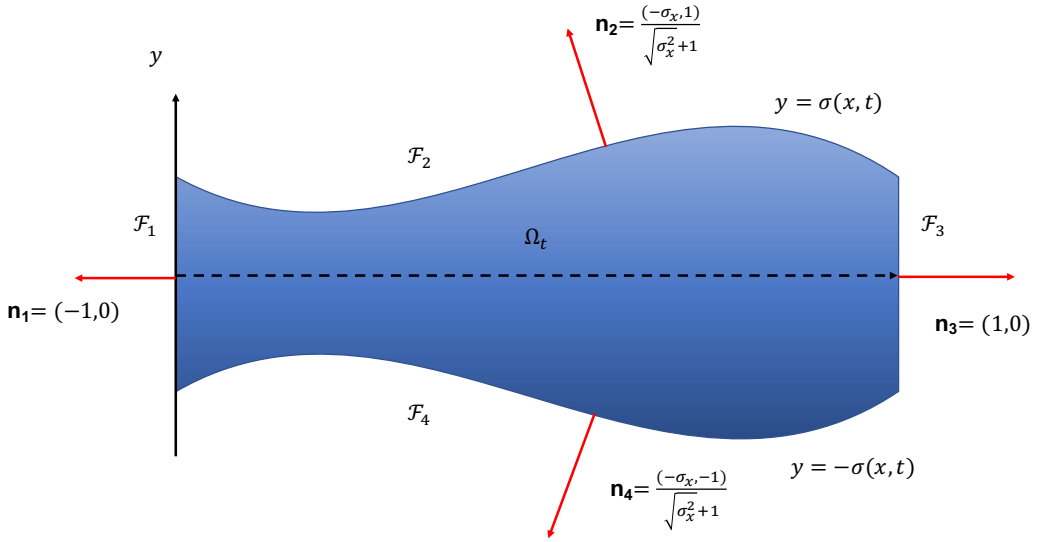

Figure 4.2: The unyielded domain.

while the second by

$$0 = \int_{\partial\Omega_t} (\boldsymbol{\tau}\boldsymbol{n} \cdot \boldsymbol{e}_2) dS. \tag{4.4}$$

Since the stress tensor is given by

$$\boldsymbol{\tau} = \begin{pmatrix} -p + \tau_{11} & \tau_{12} \\ \tau_{12} & -p + \tau_{22} \end{pmatrix},$$

on the surfaces $\mathcal{F}_1$ and $\mathcal{F}_3$ the only non zero components of the applied stress are the normal ones, namely

$$\boldsymbol{\tau}\Big|_{x=0} = \begin{pmatrix} -p_{in} & 0 \\ 0 & -p_{in} \end{pmatrix}, \qquad \boldsymbol{\tau}\Big|_{x=L} = \begin{pmatrix} -p_{out} & 0 \\ 0 & -p_{out} \end{pmatrix},$$

which implies that no torque is applied to the rigid core. Under these hypotheses, setting $\sigma_{in} = \sigma(0,t)$, $\sigma_{out} = \sigma(L,t)$ and recalling that

$$dS = \sqrt{\sigma_x^2 + 1} dx,$$

we find that (4.4) is automatically fulfilled, while (4.3) becomes

$$2\frac{\partial}{\partial t}(\rho u_c)\int_0^L \sigma dx = 2(p_{in}\sigma_{in} - p_{out}\sigma_{out}) + \\ +2\int_0^L \Big(\sigma_x p - \sigma_x \tau_{11} + \tau_{12}\Big)\Big|_\sigma dx.$$

Recalling that u_c depends only on the t variable, integrating by parts we find

$$\rho\frac{du_c}{dt}\int_0^L \sigma(x,t)dx = \int_0^L \left[-\frac{\partial p}{\partial x}\sigma - \frac{\partial \sigma}{\partial x}\tau_{11} + \tau_{12}\right]\Big|_\sigma dx, \tag{4.5}$$

which is the motion of the unyielded phase. To conclude the formulation of the model we specify the boundary conditions which are

$$u(x,h,t)=v(x,h,t) = 0, \quad \text{(No-slip and impermeability)}, \tag{4.6}$$

$$u(x,\sigma^+,t)=u_c(t), \quad v(x,\sigma^+,t) = 0, \quad \text{(continuity of the velocity)}. \tag{4.7}$$

Problem (4.2), (4.5), (4.6), (4.7) is very complex, even in a simple 2D setting. Analytical solutions can be found in the case the aspect ratio of the channel is sufficiently small. Indeed in that case we can make use of the lubrication approximation to determine a semi-analytical solution.

4.3 Non dimensional formulation

We rescale the system as

$$x = L\tilde{x}, \qquad y = \epsilon L\tilde{y}, \qquad t = \left(\frac{L}{U}\right)\tilde{t}, \qquad u = U\tilde{u},$$

$$v = \epsilon U\tilde{v}, \qquad u_c = U\tilde{u}_c, \qquad h = H\tilde{h}, \qquad \sigma = H\tilde{\sigma},$$

$$\boldsymbol{\tau} = \left(\frac{\mu U}{H}\right)\tilde{\boldsymbol{\tau}}\ , \qquad \mathbf{D} = \left(\frac{U}{H}\right)\tilde{\mathbf{D}}, \qquad p = \left(\frac{\mu U L}{H^2}\right)\tilde{p},$$

where L is the length of the channel, $H = \max_{[0,L]} h(x)$ and

$$\epsilon = \frac{H}{L} \ll 1,$$

is the aspect ratio. We also introduce the dimensionless half-discharge as

$$Q = \frac{1}{UH}\int_0^H u\ dy = \int_0^1 \tilde{u}\ d\tilde{y}. \tag{4.8}$$

With this scaling we get

$$\tilde{\mathbf{D}} = \begin{bmatrix} 2\epsilon\dfrac{\partial\tilde{u}}{\partial\tilde{x}} & \left(\dfrac{\partial\tilde{u}}{\partial\tilde{y}} + \epsilon^2\dfrac{\partial\tilde{v}}{\partial\tilde{x}}\right) \\ \left(\dfrac{\partial\tilde{u}}{\partial\tilde{y}} + \epsilon^2\dfrac{\partial\tilde{v}}{\partial\tilde{x}}\right) & 2\epsilon\dfrac{\partial\tilde{v}}{\partial\tilde{y}} \end{bmatrix},$$

$$\tilde{\boldsymbol{\tau}} = \left[1 + \frac{\sqrt{B}}{\sqrt{\dot{\tilde{\gamma}}}}\right]^2 \begin{bmatrix} 2\epsilon\dfrac{\partial\tilde{u}}{\partial\tilde{x}} & \left(\dfrac{\partial\tilde{u}}{\partial\tilde{y}} + \epsilon^2\dfrac{\partial\tilde{v}}{\partial\tilde{x}}\right) \\ \left(\dfrac{\partial\tilde{u}}{\partial\tilde{y}} + \epsilon^2\dfrac{\partial\tilde{v}}{\partial\tilde{x}}\right) & 2\epsilon\dfrac{\partial\tilde{v}}{\partial\tilde{y}} \end{bmatrix},$$

where

$$B = \left(\frac{\tau_o H}{\mu U}\right), \tag{4.9}$$

is the Bingham number and where

$$\dot{\tilde{\gamma}} = \sqrt{2\epsilon^2\left[\left(\frac{\partial\tilde{u}}{\partial\tilde{x}}\right)^2 + \left(\frac{\partial\tilde{v}}{\partial\tilde{y}}\right)^2\right] + \left(\frac{\partial\tilde{u}}{\partial\tilde{y}} + \epsilon^2\frac{\partial\tilde{v}}{\partial\tilde{x}}\right)^2}. \tag{4.10}$$

Equation $(4.2)_1$ becomes

$$\frac{\partial\tilde{u}}{\partial\tilde{x}} + \frac{\partial\tilde{v}}{\partial\tilde{y}} = 0,$$

while equations $(4.2)_{2,3}$ become

$$\begin{cases} \epsilon\mathsf{Re}\left(\dfrac{\partial\tilde{u}}{\partial\tilde{t}} + \dfrac{\partial\tilde{u}}{\partial\tilde{x}}\tilde{u} + \dfrac{\partial\tilde{u}}{\partial\tilde{y}}\tilde{v}\right) = -\dfrac{\partial\tilde{p}}{\partial\tilde{x}} + \epsilon\dfrac{\partial\tilde{\tau}_{11}}{\partial\tilde{x}} + \dfrac{\partial\tilde{\tau}_{12}}{\partial\tilde{y}}, \\ \epsilon^3\mathsf{Re}\left(\dfrac{\partial\tilde{v}}{\partial\tilde{t}} + \dfrac{\partial\tilde{v}}{\partial\tilde{x}}\tilde{u} + \dfrac{\partial\tilde{v}}{\partial\tilde{y}}\tilde{v}\right) = -\dfrac{\partial\tilde{p}}{\partial\tilde{y}} + \epsilon^2\dfrac{\partial\tilde{\tau}_{12}}{\partial\tilde{x}} + \epsilon\dfrac{\partial\tilde{\tau}_{22}}{\partial\tilde{y}}, \end{cases} \tag{4.11}$$

where

$$\mathsf{Re} = \frac{\rho U H}{\mu},$$

is the Reynolds number. Finally, equation $(4.5)_1$ becomes

$$\epsilon \mathsf{Re} \left[\dot{\tilde{v}}_c \int_0^1 \tilde{\sigma}(\tilde{x}, \tilde{t}) d\tilde{x} \right] = \int_0^1 \left[-\frac{\partial \tilde{p}}{\partial \tilde{x}} \tilde{\sigma} - \epsilon \frac{\partial \tilde{\sigma}}{\partial \tilde{x}} \tilde{\tau}_{11} + \tilde{\tau}_{12} \right] \Big|_{\tilde{\sigma}} d\tilde{x}.$$

4.4 Leading order approximation

Let us now focus on the leading order approximation. In practice we simplify the model retaining only those terms that do not contain ϵ. This is the so-called lubrication approximation. Dropping the tildes to keep the notation as light as possible we have

$$\begin{cases} \dfrac{\partial u}{\partial x} + \dfrac{\partial v}{\partial y} = 0, \\ \dfrac{\partial \tau_{12}}{\partial y} = \dfrac{\partial p}{\partial x}, \qquad \text{(Yielded phase)} \quad y \in [\sigma, h], \\ \dfrac{\partial p}{\partial y} = 0, \end{cases} \tag{4.12}$$

$$\begin{cases} \displaystyle\int_0^1 \left[-\frac{\partial p}{\partial x} \sigma + \tau_{12} \right] \Big|_{\sigma} dx = 0, \\ \\ u = u_c \qquad v = 0, \end{cases} \qquad \text{(Unyielded phase)} \quad y \in [0, \sigma], \tag{4.13}$$

where

$$\tau_{12} = \frac{\partial u}{\partial y} \left[1 + \frac{\sqrt{B}}{\sqrt{\left| \dfrac{\partial u}{\partial y} \right|}} \right]^2. \tag{4.14}$$

The yield condition is given by

$$\dot{\gamma}\Big|_{\sigma} = \left| \frac{\partial u}{\partial y} \right|_{\sigma} = 0 \tag{4.15}$$

Recalling that in the upper yielded part $\partial u / \partial y < 0$ we find

$$\frac{\partial u}{\partial y} = - \left| \frac{\partial u}{\partial y} \right|,$$

so that (4.14) rewrites as

$$\tau_{12} = -\left[\sqrt{\left|\frac{\partial u}{\partial y}\right|} + \sqrt{B}\right]^2, \tag{4.16}$$

implying that (4.15) is given by

$$\tau_{12}\Big|_{\sigma} = -B,$$

with B given by (4.9).
From $(4.12)_3$ we see that $p = p(x,t)$ so that, integrating $(4.12)_2$ between σ and y we find

$$\tau_{12} = -B + \frac{\partial p}{\partial x}(y-\sigma). \tag{4.17}$$

Inserting (4.16) into (4.17) we get

$$\left[\sqrt{\left|\frac{\partial u}{\partial y}\right|} + \sqrt{B}\right]^2 = B + \frac{\partial p}{\partial x}(\sigma - y),$$

and hence

$$\frac{\partial u}{\partial y} = -\left(\sqrt{B + \frac{\partial p}{\partial x}(\sigma - y)} - \sqrt{B}\right)^2. \tag{4.18}$$

Assuming that the pressure drop $\Delta p > 0$ we expect $p_x < 0$ so that $p_x(\sigma - y) > 0$ in the yielded phase. Integrating (4.18) between y and h and exploiting (4.6) we find

$$u = \int_y^h \left(\sqrt{B + \frac{\partial p}{\partial x}(\sigma - \xi)} - \sqrt{B}\right)^2 d\xi.$$

Setting

$$\mathcal{P} = \frac{p}{B}, \tag{4.19}$$

we may rewrite u as

$$\frac{u}{B} = \int_y^h \left(\sqrt{1 + \mathcal{P}_x(\sigma - \xi)} - 1\right)^2 d\xi,$$

which, after some algebra, gives

$$\begin{aligned} \frac{u}{B} &= \frac{\mathcal{P}_x}{2}\Big[(\sigma - y)^2 - (\sigma - h)^2\Big] + 2(h - y) + \\ &\quad + \frac{4}{3\mathcal{P}_x}\Big[(\mathcal{P}_x(\sigma - h) + 1)^{3/2} - (\mathcal{P}_x(\sigma - y) + 1)^{3/2}\Big]. \end{aligned} \tag{4.20}$$

Evaluating (4.20) on $y = \sigma$ we find

$$-\frac{u_c}{B} = \frac{\mathcal{P}_x}{2}(\sigma - h)^2 + 2(\sigma - h) - \frac{4}{3\mathcal{P}_x}\left[(\mathcal{P}_x(\sigma - h) + 1)^{3/2} - 1\right], \tag{4.21}$$

where we recall that u_c does not depend on x. Rearranging (4.20) and (4.21) we find

$$\frac{u}{u_c} = \left[1 - \frac{\frac{\mathcal{P}_x}{2}(\sigma - y)^2 + 2(\sigma - y) - \frac{4}{3\mathcal{P}_x}\left[(\mathcal{P}_x(\sigma - y) + 1)^{3/2} - 1\right]}{\frac{\mathcal{P}_x}{2}(\sigma - h)^2 + 2(\sigma - h) - \frac{4}{3\mathcal{P}_x}\left[(\mathcal{P}_x(\sigma - h) + 1)^{3/2} - 1\right]}\right], \tag{4.22}$$

so that we can easily check that $u|_h = 0$ and $u|_\sigma = u_c$, i.e. (4.6), (4.7) are fulfilled. We now exploit the constraint of incompressibility $u_x + v_y = 0$. Recalling the conditions $v|_h = v|_\sigma = 0$ we find

$$0 = \int_\sigma^h \frac{\partial v}{\partial y} dy = -\int_\sigma^h \frac{\partial u}{\partial x} dy.$$

As a consequence

$$\frac{\partial}{\partial x}\left(\int_\sigma^h u dy\right) = -u_c \frac{\partial \sigma}{\partial x} + \underbrace{\left(\int_\sigma^h \frac{\partial u}{\partial x} dy\right)}_{=0},$$

i.e.

$$\frac{\partial}{\partial x}\left(\int_\sigma^h \frac{u}{u_c} dy + \sigma\right) = 0, \tag{4.23}$$

which we may write also as

$$\frac{\partial}{\partial x}\left(\frac{\int_\sigma^h u \; dy + \sigma u_c}{u_c}\right) = 0. \tag{4.24}$$

Recalling the definition (4.8), we easily realize that

$$Q = \int_0^h u \; dy = \int_\sigma^h u \; dy + \sigma u_c, \tag{4.25}$$

and since u_c does not depend on x, (4.24) is equivalent to $\dfrac{\partial Q}{\partial x} = 0$, i.e. the non dimensional discharge is the same at any cross section x of the channel. Inserting (4.21) into (4.23) we find

$$\frac{\partial}{\partial x}\left(h - \int_{\sigma}^{h} \frac{\frac{\mathcal{P}_x}{2}(\sigma-y)^2 + 2(\sigma-y) - \frac{4}{3\mathcal{P}_x}\Big[(\mathcal{P}_x(\sigma-y)+1)^{3/2}-1\Big]}{\frac{\mathcal{P}_x}{2}(\sigma-h)^2 + 2(\sigma-h) - \frac{4}{3\mathcal{P}_x}\Big[(\mathcal{P}_x(\sigma-h)+1)^{3/2}-1\Big]}dy\right) = 0. \tag{4.26}$$

Integrating the above in y, after some algebra we find

$$h + \frac{\frac{\mathcal{P}_x}{6}(\sigma-h)^3 + (\sigma-h)^2 + \frac{4}{3\mathcal{P}_x}(\sigma-h) - \frac{8}{15\mathcal{P}_x^2}\Big[(\mathcal{P}_x(\sigma-h)+1)^{5/2}-1\Big]}{\frac{\mathcal{P}_x}{2}(\sigma-h)^2 + 2(\sigma-h) - \frac{4}{3\mathcal{P}_x}\Big[(\mathcal{P}_x(\sigma-h)+1)^{3/2}-1\Big]} = \frac{Q}{u_c}, \tag{4.27}$$

where u_c is the core velocity given by (4.21) and where we assume that Q, given by (4.25), is positive. Introducing the quantity

$$\ell\,(x) = h\,(x) - \sigma\,(x) > 0, \tag{4.28}$$

we rewrite the (4.27) as

$$\frac{-\frac{\mathcal{P}_x}{6}\ell^3 + \ell^2 - \frac{4}{3\mathcal{P}_x}\ell - \frac{8}{15\mathcal{P}_x^2}\Big[(1-\mathcal{P}_x\ell)^{5/2}-1\Big]}{\frac{\mathcal{P}_x}{2}\ell^2 - 2\ell - \frac{4}{3\mathcal{P}_x}\Big[(1-\mathcal{P}_x\ell)^{3/2}-1\Big]} = \frac{Q}{u_c} - h. \tag{4.29}$$

Next, the integral equation for the unyielded phase $(4.13)_1$ that can be rewritten as

$$-\int_{0}^{1} \mathcal{P}_x(h-\ell)dx = 1. \tag{4.30}$$

Finally, from (4.21), we observe that

$$\frac{d}{dx}\left(\frac{u_c}{B}\right) = \frac{d}{dx}\left[\frac{\mathcal{P}_x}{2}\ell^2 - \ell - \frac{4}{3\mathcal{P}_x}\Big[(1-\mathcal{P}_x\ell)^{3/2}-1\Big]\right] = 0.$$

The above is due to the fact that u_c cannot depend on x.

In conclusion, the problem to be solved is the following

$$\begin{cases} \dfrac{1}{\mathcal{P}_x}\dfrac{-\frac{1}{6}(\mathcal{P}_x\ell)^3+(\mathcal{P}_x\ell)^2-\frac{4}{3}(\mathcal{P}_x\ell)-\frac{8}{15}\Big[(1-\mathcal{P}_x\ell)^{5/2}-1\Big]}{\frac{1}{2}(\mathcal{P}_x\ell)^2-2(\mathcal{P}_x\ell)-\frac{4}{3}\Big[(1-\mathcal{P}_x\ell)^{3/2}-1\Big]}=\dfrac{Q}{u_c}-h, \\ \\ -\displaystyle\int_0^1 \mathcal{P}_x(h-\ell)dx=1, \\ \\ \dfrac{d}{dx}\left[\dfrac{\mathcal{P}_x}{2}\ell^2-\ell-\dfrac{4}{3\mathcal{P}_x}\Big[(1-\mathcal{P}_x\ell)^{3/2}-1\Big]\right]=0, \end{cases} \tag{4.31}$$

to which we must add the boundary conditions $\mathcal{P}|_{x=0}$ and $\mathcal{P}|_{x=1}$ if the pressure difference is prescribed or alternatively Q and $\mathcal{P}|_{x=1}$ (actually in place of $\mathcal{P}|_{x=1}$ we can prescribe $\mathcal{P}|_{x=0}$). The unknowns are: $(\mathcal{P},\ell,Q)$ in the first case and $(\mathcal{P},\ell,\mathcal{P}|_{x=1})$ in the second case. The problem is thus formally closed. However the solution technique varies according to the conditions that are prescribed.

4.5 Solution to system (4.31) when the discharge and the outlet pressure are prescribed

Here we describe a method, different from the one illustrated in [47], to determine the solution of system (4.31), when the dimensionless discharge Q is prescribed and when the outlet pressure, i.e. $p|_{x=1}$ is known. In particular, we rescale the outlet pressure 0, setting $p|_{x=1}=0$. Let us introduce the new function

$$z(x)=-\mathcal{P}_x(x)\,\ell(x), \tag{4.32}$$

with ℓ given by (4.28). We remark that $z>0$.
System (4.31) can be rewritten as

$$\begin{cases} \dfrac{1}{\mathcal{P}_x}\dfrac{N(z)}{D(z)}=\dfrac{Q}{u_c}-h, \\ \\ \displaystyle\int_0^1(-z-\mathcal{P}_x h)dx=1, \\ \\ \dfrac{d}{dx}\left[\dfrac{D(z)}{\mathcal{P}_x}\right]=0 \end{cases} \tag{4.33}$$

where

$$\begin{aligned} N(z) &= \tfrac{z^3}{6} + z^2 + \tfrac{4}{3}z - \tfrac{8}{15}\Big[(1+z)^{5/2} - 1\Big] \\ D(z) &= \tfrac{z^2}{2} + 2z - \tfrac{4}{3}\Big[(1+z)^{3/2} - 1\Big], \end{aligned} \tag{4.34}$$

and, exploiting (4.21),

$$\frac{u_c}{B} = -\frac{D(z)}{\mathcal{P}_x}. \tag{4.35}$$

From $(4.33)_1$ we get

$$\frac{1}{\mathcal{P}_x} = \frac{\left(\dfrac{Q}{u_c} - h\right) D(z)}{N(z)}, \tag{4.36}$$

which plugged in $(4.33)_3$ gives

$$\frac{d}{dx}\left[\frac{\left(\dfrac{Q}{u_c} - h\right) D(z)^2}{N(z)}\right] = 0. \tag{4.37}$$

Computing the derivative in (4.37) we find

$$\frac{dz}{dx} = \frac{h_x D(z) N(z)}{\left(\dfrac{Q}{u_c} - h\right)\left[2D'(z)N(z) - N'(z)D(z)\right]} = \mathcal{F}(z, x, Q, u_c), \tag{4.38}$$

where Q is prescribed and u_c is unknown.
We now solve the nonlinear Cauchy problem

$$\begin{cases} z_x = \mathcal{F}(z, x, u_c), \\ \mathcal{P}_x = \dfrac{N(z)}{\left(\dfrac{Q}{u_c} - h\right) D(z)}, \\ \mathcal{P}\big|_{x=1} = 0, \\ z\Big|_{x=1} = z_o, \end{cases} \tag{4.39}$$

starting from $x = 1$ and proceeding backward. In particular, $0 < z_o = \mathcal{O}(1)$ is some initial guess for the unknown z. Solving (4.39) we obtain the solution $(\mathcal{P}, z)$,

where both $\mathcal{P}$ and z are functions of x but depend also on the parameters z_o and u_c. The latter are determined by imposing that $(\mathcal{P}, z)$ fulfils $(4.33)_2$ and (4.35). The numerical procedure used to solve (4.39) coupled with $(4.33)_2$ and (4.35) is illustrated in the next section.
We notice that when $h_x = 0$, i.e. when $h = 1$, (4.38) entails $z_x = 0$ and $z = z_o = const.$, so that $z_o = -\mathcal{P}_x \ell = const.$ Recalling that Q is prescribed, equation (4.36) gives

$$\frac{1}{\mathcal{P}_x} = \frac{\left(\dfrac{Q}{u_c} - 1\right) D(z_o)}{N(z_o)} = const., \tag{4.40}$$

and therefore $\ell = const$ yielding $\sigma = const.$, since $\ell = 1 - \sigma$. We now exploit $(4.33)_2$ to evaluate $\mathcal{P}_x$, getting

$$-z_o - \mathcal{P}_x = 1, \quad \Rightarrow \quad \mathcal{P}_x = -\left(1 + z_o\right), \tag{4.41}$$

which, once plugged in (4.40), gives rise to the following algebraic equation

$$-\frac{N\left(z_o\right)}{\left(1 + z_o\right) D\left(z_0\right)} = \frac{Q}{u_c} - 1. \tag{4.42}$$

from which we can derive z_o, provided we are able to express u_c in terms of z_o. To this aim, we plug (4.41) into (4.35)

$$\frac{u_c}{B} = \frac{D(z_o)}{1 + z_o}, \tag{4.43}$$

and exploit such a relation in (4.42)

$$-\frac{N\left(z_o\right)}{\left(1 + z_o\right) D\left(z_0\right)} = \frac{Q}{B} \frac{1 + z_o}{D\left(z_o\right)} - 1, \tag{4.44}$$

which is the final algebraic equation allowing to derive z_o. In particular, introducing

$$F\left(z_0\right) = \frac{Q}{B} \frac{1 + z_o}{D\left(z_o\right)} - 1 + \frac{N\left(z_o\right)}{\left(1 + z_o\right) D\left(z_0\right)}, \tag{4.45}$$

we rewrite (4.44) as $F\left(z_0\right) = 0$. So, solving $F\left(z_0\right) = 0$, we find z_0 then, in a chain, u_c from (4.43) and σ from (4.32), i.e.

$$\sigma = 1 - \frac{z_o}{1 + z_o} = \frac{1}{1 + z_o}.$$

Clearly, z_0 solution to (4.44) depends on the ratio Q/B. So, the first panel of Fig. 4.3 displays $z_0 = z_0\left(Q/B\right)$. We notice that $z_0 > 1$, as $Q/B > 0$, and that $z_0 \to \infty$, when $Q/B \to \infty$.

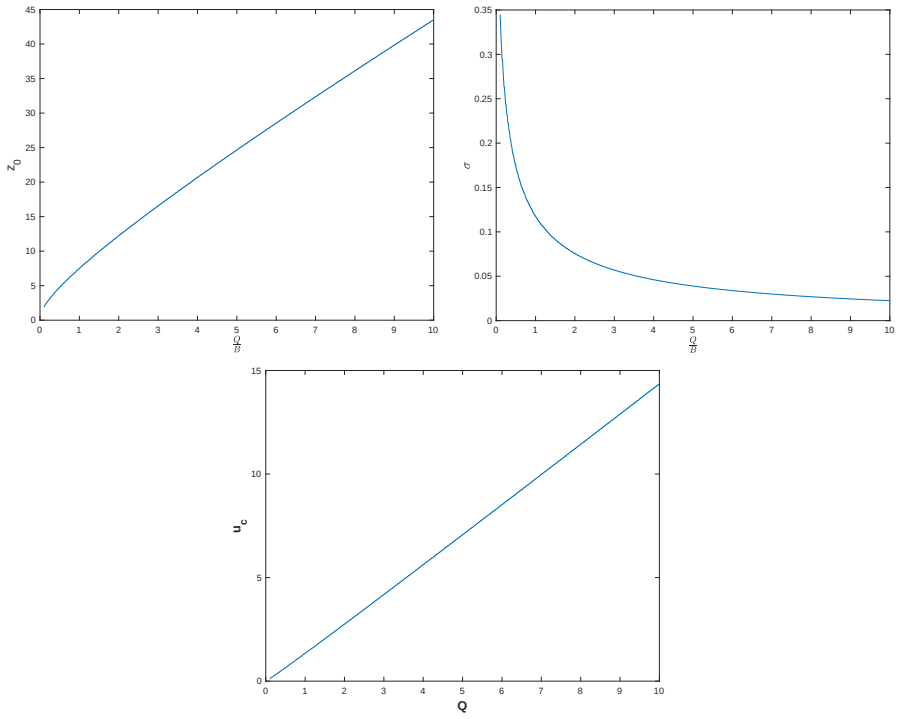

Figure 4.3: The first panel shows $z_0 = z_0(Q/B)$, with z_0 obtained by solving $F(z_0) = 0$, with F given by (4.45). The second plot displays $\sigma = \sigma(Q/B)$. In the last panel we take $B = 1$, and plot $u_c = u_c(Q)$, given by (4.43).

To solve (4.39) coupled with $(4.33)_2$ and (4.35) we start from the solution corresponding to the flat channel, i.e. where $h(x) \equiv 1$. In particular, let $\bar{z}_0$ the solution to (4.44) and $\bar{u_c}$ given by (4.43). We then consider a generic wall profile $h\,(x) \neq 1$, and set up an iterative minimum-finding procedure. We proceed by determining a grid around the values $\bar{z}_0$ and $\bar{u_c}$ and, after having selected a pair (z_0, u_c) in the grid, we solve the Cauchy problem (4.39), obtaining the pair $(\mathcal{P}\,(x; z_0, u_c)\,,\ z\,(x; z_0, u_c))$ and compute

$$d_1 = \left| \frac{u_c}{B} - \frac{\left(\dfrac{Q}{u_c} - h\right) D^2(z)}{N(z)} \right|, \tag{4.46}$$

$$d_2 = \left| \int_0^1 \left[z(\xi) + 1 + h(\xi) \frac{N(z(\xi))}{D(z(\xi)) \left(\dfrac{Q}{u_c} - h(\xi)\right)} \right] d\xi \right|. \tag{4.47}$$

We then repeat the procedure all grid values and for each value (z_0, u_c) we compute the norm

$$\|d\| = \sqrt{d_1^2 + d_2^2}.$$

We stop the procedure when we reach a pair (z_0^*, u_c^*), whose corresponding $\|d\|$ is smaller than a prescribed tolerance. In particular, once u_c^* has been determined, exploiting (4.32) and (4.36), we obtain the following explicit expression for σ

$$\sigma(x) = h(x) + \frac{z(x) \left(\dfrac{Q}{u_c} - h(x)\right) D(z)}{N(z)}.$$

In Fig. 4.4 some simulations for various values of Q/B are displayed. As wall profile we considered

$$h\,(x) = 1 \pm \frac{1}{\delta} \sin\,(\pi x)\,.$$

In agreement with the most recent literature, the yield surface $\sigma\,(x)$ shows a profile "inverse" with respect to $h\,(x)$. Indeed, where the duct attains its maximum/minimum width the surface $\sigma\,(x)$ attains its minimum/maximum thickness.

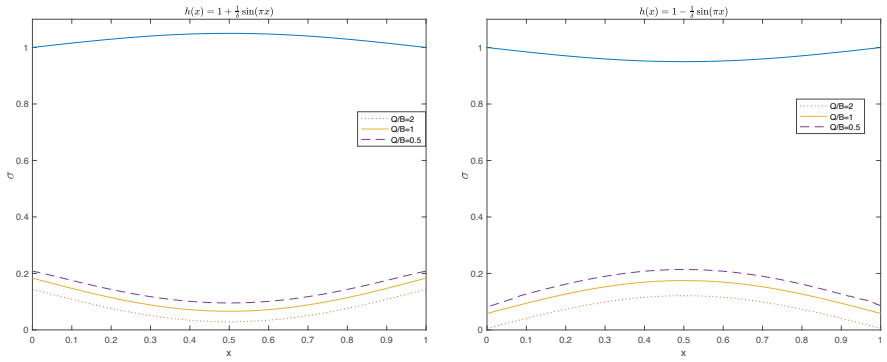

Figure 4.4: Plots of the surface σ for $\delta = 20$ and three values of $\frac{Q}{B}$: 2, 1 and 0.5.

4.6 Solution to system (4.31) when the pressure difference is prescribed

We now assume that, in place of the discharge Q, the pressure drop $\Delta p = p|_{x=0} - p|_{x=1}$, is prescribed, i.e. recalling (4.19)

$$-\int_0^1 \mathcal{P}_x dx = \frac{\Delta p}{B}. \tag{4.48}$$

In particular, recalling (4.19), we stipulate $\mathcal{P}(0) = \dfrac{\Delta p}{B}$, and $\mathcal{P}(1) = 0$. We then proceed as in Section 4.5 and, recalling (4.36) and (4.38) in which we set $K = Q/u_c$, unknown parameter, we focus on the following Cauchy problem

$$\begin{cases} \mathcal{P}_x = \dfrac{N(z)}{(K - h(x))\, D(z)}, \\ \\ z_x = \dfrac{h_x D(z) N(z)}{(K-h)\left[2D'(z)N(z) - N'(z)D(z)\right]}, \\ \\ \mathcal{P}(0) = \frac{\Delta p}{B}, \quad z(0) = z_o, \end{cases} \tag{4.49}$$

where z is given by (4.32) and z_o is some initial guess (which, at this stage, plays the role of an unknown parameter as K). Solving (4.49) we find $\mathcal{P} = \mathcal{P}(x, K, z_o)$, and $z = z(x, K, z_o)$. To determine K and z_o we impose the second boundary

condition on $\mathcal{P}$, i.e. $\mathcal{P}(1)=0$, and $(4.33)_2$, namely

$$\begin{cases} \mathcal{P}(1,K,z_o)=0, \\ \\ \displaystyle\int_0^1 \Big[z(x)+h(x)\underbrace{\frac{N(z)}{(K-h(x))\,D(z)}}_{\mathcal{P}_x}\Big]dx=-1. \end{cases} \tag{4.50}$$

The yield surface follows from (4.32), i.e.

$$\sigma(x)=h(x)+\frac{z(x)}{\mathcal{P}_x}=h(x)+z(x)\frac{N(z(x))}{(K-h(x))\,D(z(x))}. \tag{4.51}$$

When $h_x=0$, i.e. $h\equiv 1$, $(4.49)_2$ entails $z(x)=\bar{z}_o$, while $(4.49)_1$, $(4.49)_3$ imply

$$\mathcal{P}_x=\frac{N(\bar{z}_o)}{\left(\overline{K}-1\right)D(\bar{z}_o)},\quad\Longrightarrow\quad \mathcal{P}(x)=\frac{N(\bar{z}_o)}{\left(\overline{K}-1\right)D(\bar{z}_o)}x+\frac{\Delta p}{B}. \tag{4.52}$$

Therefore system (4.50) rewrites as

$$\begin{cases} \dfrac{N(\bar{z}_o)}{\left(\overline{K}-1\right)D(\bar{z}_o)}+\dfrac{\Delta p}{B}=0, \\ \\ \bar{z}_o+\dfrac{N(\bar{z}_o)}{\left(\overline{K}-1\right)D(\bar{z}_o)}=-1, \end{cases} \tag{4.53}$$

by which

$$\frac{N(\bar{z}_o)}{\left(\overline{K}-1\right)D(\bar{z}_o)}=-\frac{\Delta p}{B},\qquad \underset{(4.52)}{\Longrightarrow}\qquad \mathcal{P}(x)=\frac{\Delta p}{B}(1-x),$$

and

$$\bar{z}_o=\frac{\Delta p}{B}-1,\qquad \overline{K}=1-\frac{BN(\bar{z}_o)}{\Delta pD(\bar{z}_o)}, \tag{4.54}$$

with N and D given by (4.34). Next, exploiting (4.51) we obtain

$$\sigma_o=1-\frac{\bar{z}_o}{\dfrac{\Delta p}{B}}=\frac{B}{\Delta p}.$$

To solve problem (4.50) coupled with (4.53) we start considering $\bar{z}_o$ and $\overline{K}$ given by (4.54), i.e. the parameters corresponding to the flat channel $h(x)\equiv 1$. We then consider a generic wall profile $h(x)\neq 1$, and set up an iterative minimum-finding

scheme. We proceed by determining a grid around the values $\bar{z}_o$ and $\overline{K}$ and, after having selected a pair (z_o, K) in the grid, we solve the Cauchy problem (4.49), obtaining the pair $(\mathcal{P}(x; z_o, K),\ z(x; z_o, K))$ and compute

$$d_1 = |\mathcal{P}(1, K, z_o)|,$$

$$d_2 = \left| \int_0^1 \left(z(x) + h(x) \frac{N(z)}{(K - h(x)) D(z)} + 1 \right) dx \right|.$$

We then repeat the procedure for all grid values and for each pair (z_o, K) we compute the norm

$$\|d\| = \sqrt{d_1^2 + d_2^2}.$$

We stop the procedure when we reach a pair (z_o^*, K^*), whose corresponding $\|d\|$ is smaller than a prescribed tolerance. Once (z_o, K) have been determined, σ is given by (4.51).

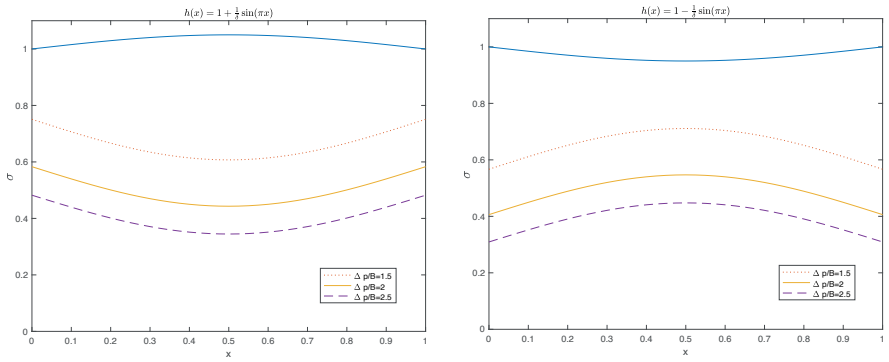

Figure 4.5: Simulations for $h(x) = 1 \pm \frac{1}{\delta}\sin(\pi x)$, with $\delta = 20$, for various values of $\dfrac{\Delta p}{B}$.

4.7 Approximate solution

In this section we illustrate a technique to find an approximate solution to (4.31) when the pressure difference is prescribed and peculiar conditions on the data are fulfilled. We recall the generalized form of the binomial Newton formula

$$\sum_{k=0}^{\infty} \binom{\alpha}{k} x^k = (1 + x)^{\alpha}, \quad \text{for} \quad |x| < 1, \tag{4.55}$$

where, given $\alpha \in \mathbb{R}$ and $k \in \mathbb{N}$, $\binom{\alpha}{k}$ is the generalized binomial coefficient

$$\binom{\alpha}{0} = 1, \qquad \binom{\alpha}{k} = \frac{\alpha\,(\alpha-1)\ldots(\alpha-(k-1))}{k!}, \quad \text{for} \quad k \geq 1.$$

So, assuming

$$|\mathcal{P}_x(\sigma - h)| < 1, \tag{4.56}$$

we exploit (4.55) in (4.20),

$$\frac{u}{B} = -\frac{1}{12}\mathcal{P}_x^2\left[(\sigma-h)^3 - (\sigma-y)^3\right] + \mathcal{O}(|\mathcal{P}_x(\sigma-h)|^3) \tag{4.57}$$

where the third order terms have been neglected. Proceeding similarly in (4.21) we obtain

$$\frac{u_c}{B} = \frac{1}{12}\mathcal{P}_x^2(h-\sigma)^3 + \mathcal{O}(|\mathcal{P}_x(\sigma-h)|^3). \tag{4.58}$$

Then neglecting the higher order terms the velocity field u inside the channel can be rewritten as

$$u = \begin{cases} u_c - \dfrac{1}{12}B\mathcal{P}_x^2(h-\sigma)^3 & 0 < y < \sigma \\ \\ u_c - \dfrac{1}{12}B\mathcal{P}_x^2(y-\sigma)^3 & \sigma < y < h \end{cases} \tag{4.59}$$

where we remind that $\mathcal{P}_x < 0$. We remark that the approximate expression (4.59) fulfills the no-slip condition.
Let us now rewrite equation (4.23) as follows

$$\frac{\partial}{\partial x}\left(\int_\sigma^h \frac{u}{B}dy\right) = -\frac{u_c}{B}\frac{\partial \sigma}{\partial x}.$$

After some algebra and using (4.57) and (4.58) we obtain

$$\sigma(x) = -3h(x) + \mathcal{C}, \tag{4.60}$$

where $\mathcal{C}$ is a constant unknown at this stage. To determine $\mathcal{C}$, we exploit equations (4.60) and (4.30), namely

$$\begin{cases} \displaystyle\int_0^1 p_x\sigma \; dx = -B, \\ \sigma = -3h + \mathcal{C}. \end{cases}$$

Imposing the boundary conditions for the pressure, i.e. $p(x = 0) = \Delta p$, and $p(x = 1) = 0$, we get this explicit expression for $\mathcal{C}$

$$\mathcal{C} = \frac{B - 3\int_0^1 p_x h \, dx}{\Delta p},$$

which, plugged into (4.60), gives

$$\sigma = -3h(x) + \frac{B - 3\int_0^1 p_x h \, dx}{\Delta p}. \tag{4.61}$$

At this point we are in position to determine $p(x)$. We take (4.58), which, recalling (4.28), can be rewritten as

$$\frac{u_c}{B} = \frac{1}{12}\mathcal{P}_x^2 \, \ell^3 = 0,$$

and differentiate it with respect to x

$$p_{xx} + \frac{3}{2} p_x \left(\frac{\ell_x}{\ell}\right) = 0.$$

Now exploiting the (4.60) we obtain the following boundary value problem based on an integro-differential equation

$$\begin{cases} p_{xx} + \dfrac{6h_x}{4h(x) + \dfrac{3\int_0^1 p_x h \, dx - B}{\Delta p}} p_x = 0, \\ p|_{x=0} = \Delta p, \\ p|_{x=1} = 0. \end{cases} \tag{4.62}$$

Remark 4.7.1 *As already stated the approximation is meaningful when (4.56) is fulfilled, i.e.* $\frac{|p_x|}{B}|\sigma - h| < 1$.
Considering, for simplicity, $h \equiv 1$*, the pressure gradient is* $p_x = -\Delta p$ *and, exploiting* (4.61)*, we have* $\sigma = \frac{B}{\Delta p}$*. Hence*

$$\frac{|p_x|}{B}|\sigma - 1| < 1 \Longrightarrow \sigma > \frac{1}{2}.$$

At the same time, in order to prevent the flow come to a stop, $\sigma < 1$ *i.e.* $\frac{B}{\Delta p} < 1$. *Hence the approximation above developed is expected to hold true when*

$$\frac{1}{2} < \frac{B}{\Delta p} < 1. \tag{4.63}$$

To solve the problem (4.62) we set up an iterative procedure. As first guess we consider the linear function $p(x) = \Delta p(1-x)$, and use (4.61), to give the first guess of the yield surface. The solution at the n^{th}, $n \geq 1$, step is obtained solving this boundary value problem

$$\begin{cases} p_{xx}^{(n)} + 6h_x \left[4h(x) + \dfrac{3\displaystyle\int_0^1 p_x^{(n-1)} h \, dx - B}{\Delta p} \right]^{-1} p_x^{(k)} = 0, \\ p^{(n)}\big|_{x=0} = \Delta p, \\ p^{(n)}\big|_{x=1} = 0, \end{cases}$$

and the corresponding yield surface $\sigma^{(n)}$ is obtained by (4.61). We stop the procedure when $\left\| p^{(n)} - p^{(n-1)} \right\|_{\mathrm{L}^2([0,1])}$ becomes smaller than a prescribed tolerance. Figure 4.6 displays the yield surface when the wall profile is $h(x) = 1 \pm \frac{1}{\delta}\sin(\pi x)$, with $\delta = 20$, for various values of $B/\Delta p$.

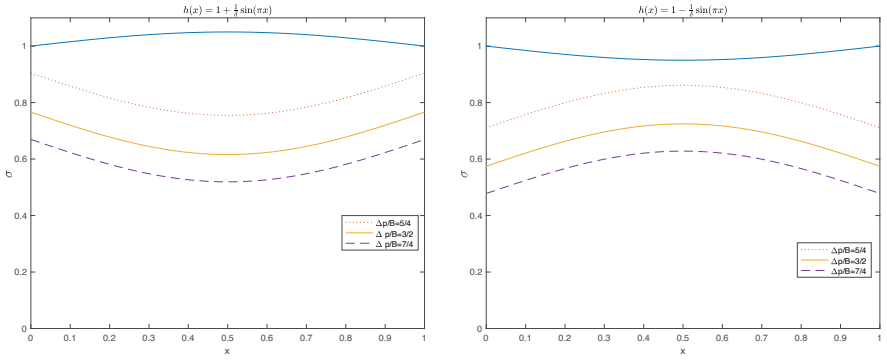

Figure 4.6: Plots of the approximate yield surface $\sigma\,(x)$ when $h(x) = 1 \pm \frac{1}{20}\sin(\pi x)$, for three values of $\frac{\Delta p}{B}$, namely $\frac{5}{4}$, $\frac{3}{2}$ and $\frac{7}{4}$ fulfilling (4.63).

The approximation here developed holds true for $|\mathcal{P}_x||\sigma - h| < 1$. So to validate the procedure we have to verify if $|\mathcal{P}_x||\sigma - h| < 1$ is fulfilled. Figure 4.7 shows the plot of $|\mathcal{P}_x||\sigma - h|$ for the 3 cases displayed in Fig. 4.6.

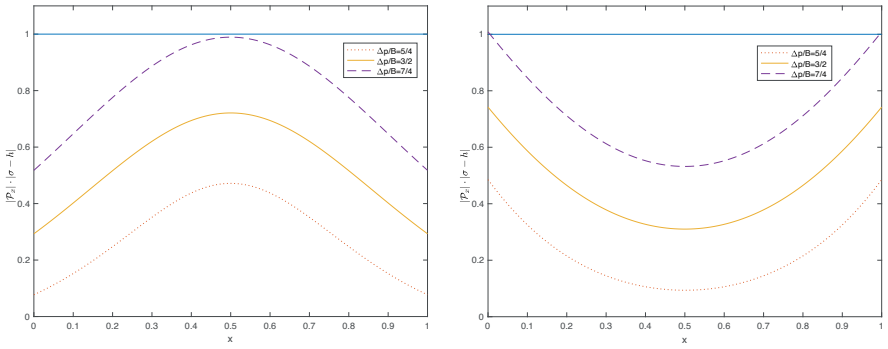

Figure 4.7: Plots of $|\mathcal{P}_x||\sigma - h|$ for the cases in the Fig. 4.6.

In the right panel of Fig. 4.7 we notice that the condition under which the approximation is valid is not satisfied at the inlet and outlet, so just in these two positions it is possible that there are problems determining $\sigma(x)$.
In Fig. 4.8 we report the comparison between $\sigma(x)$ given by (4.51) and $\sigma(x)$ obtained by the approximate model (4.62), (4.61). Figure 4.9 displays again the comparison between $\sigma(x)$ given by (4.51) and the approximated one, i.e. $\sigma(x)$ given by (4.62) and (4.61), but now $\frac{B}{\Delta p} < \frac{1}{2}$, i.e. out of the range of validity of the approximate model.
Figure 4.10 shows the comparison between $p(x)$ obtained solving (4.49), (4.50) and solving (4.62) when $\frac{B}{\Delta p} = 0.75$, and $\frac{B}{\Delta p} = 0.91$.

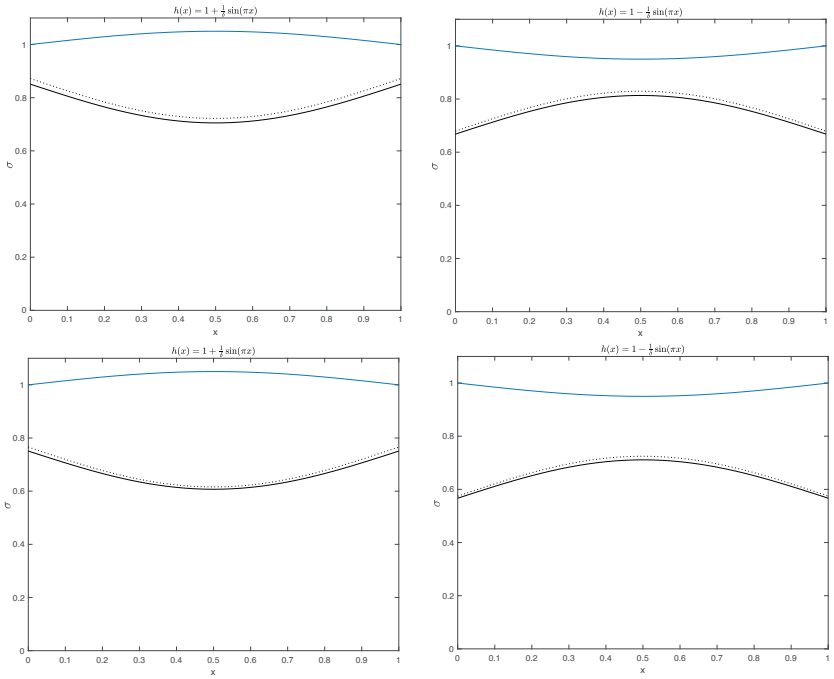

Figure 4.8: Comparisons between $\sigma(x)$ given by (4.51), continuous curve, and $\sigma(x)$ given by the approximate model (4.62), (4.61), dotted curve. In the upper panels $\frac{B}{\Delta p} = \frac{10}{13}$. In the lower panels $\frac{B}{\Delta p} = \frac{2}{3}$

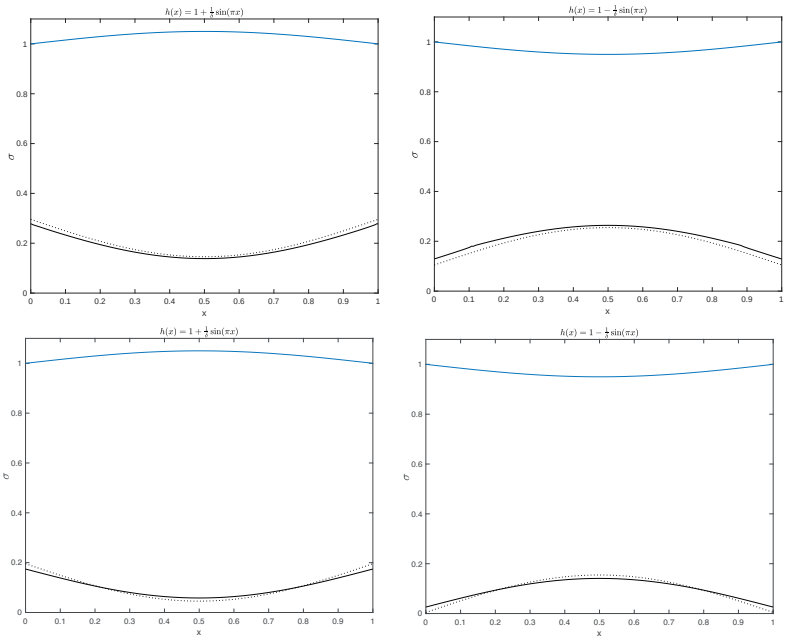

Figure 4.9: Comparisons between $\sigma(x)$ given by (4.51), continuous curve, and $\sigma(x)$ given by the approximate model (4.62), (4.61), dotted curve, when $\frac{B}{\Delta p} < \frac{1}{2}$, i.e. out of the validity range for the approximation model. In the upper panels $\frac{B}{\Delta p} = \frac{1}{5}$. In the lower panels $\frac{B}{\Delta p} = \frac{1}{10}$

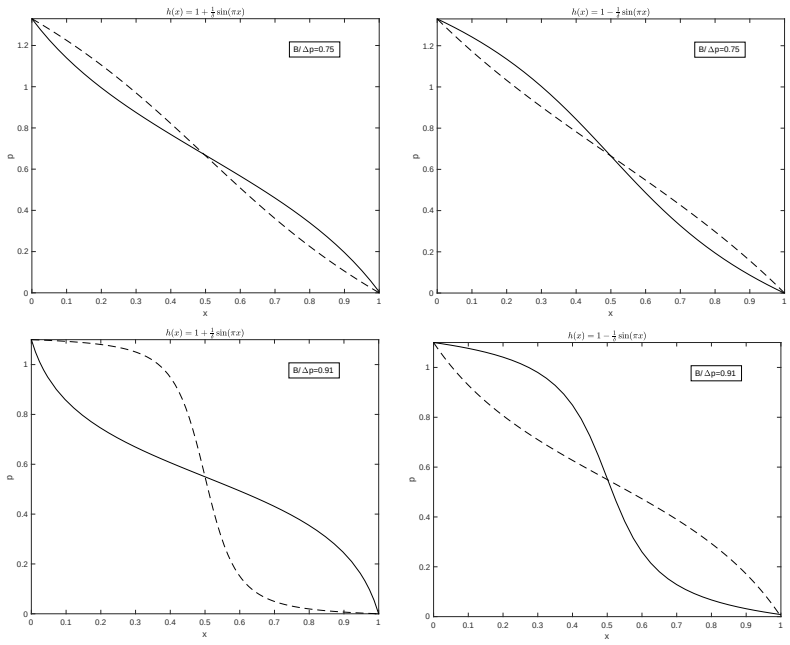

Figure 4.10: Comparisons between $p(x)$ given by (4.51), continuous curve, and $p(x)$ given by the approximate model (4.62), dotted curve, for $\frac{B}{\Delta p} = 0.75$, $\frac{B}{\Delta p} = 0.91$. On the left side the wall profile is $h(x) = 1 + \frac{1}{\delta}\sin(\pi x)$ on the right side $h(x) = 1 - \frac{1}{\delta}\sin(\pi x)$. In both cases with $\delta = 20$.

4.8 Comparison with the pressure driven Bingham flow in a channel

Problem (4.62) is very similar to the one governing the Bingham flow in a channel, namely (see [45], equation (39))

$$\begin{cases} p_{xx} + \left(\dfrac{6h_x \Delta p}{3h\Delta p + 2\displaystyle\int_0^1 p_x h dx - B} \right) p_x = 0, \\ \\ p|_{x=0} = \Delta p, \quad p|_{x=1} = 0, \end{cases} \tag{4.64}$$

with the yield surface given by (see again [45], equation (34))

$$\sigma(x) = -2h(x)) + \frac{B}{\Delta p} - \frac{2}{\Delta p}\int_0^1 p_x h \, dx. \tag{4.65}$$

In Fig.4.11 we report the yield surface given by (4.65), i.e. the Bingham yield surface, and $\sigma(x)$ obtained solving (4.49), (4.50), i.e. the Casson yield surface. We have considered three cases, $\frac{B}{\Delta p} = 0.1$, 0.5 and 0.86.
The plots show that the two models give rise to very similar curves when $\frac{B}{\Delta p} = 0.1$ and 0.5. If $\frac{B}{\Delta p} = 0.86$ the difference between the two curves is much more evident. We remark that, when $h(x) = 1 + \delta \sin(\pi x)$, left panels, the largest difference occurs in central region. On the contrary, when $h(x) = 1 - \delta \sin(\pi x)$, right panels, the largest difference occurs in the external regions.

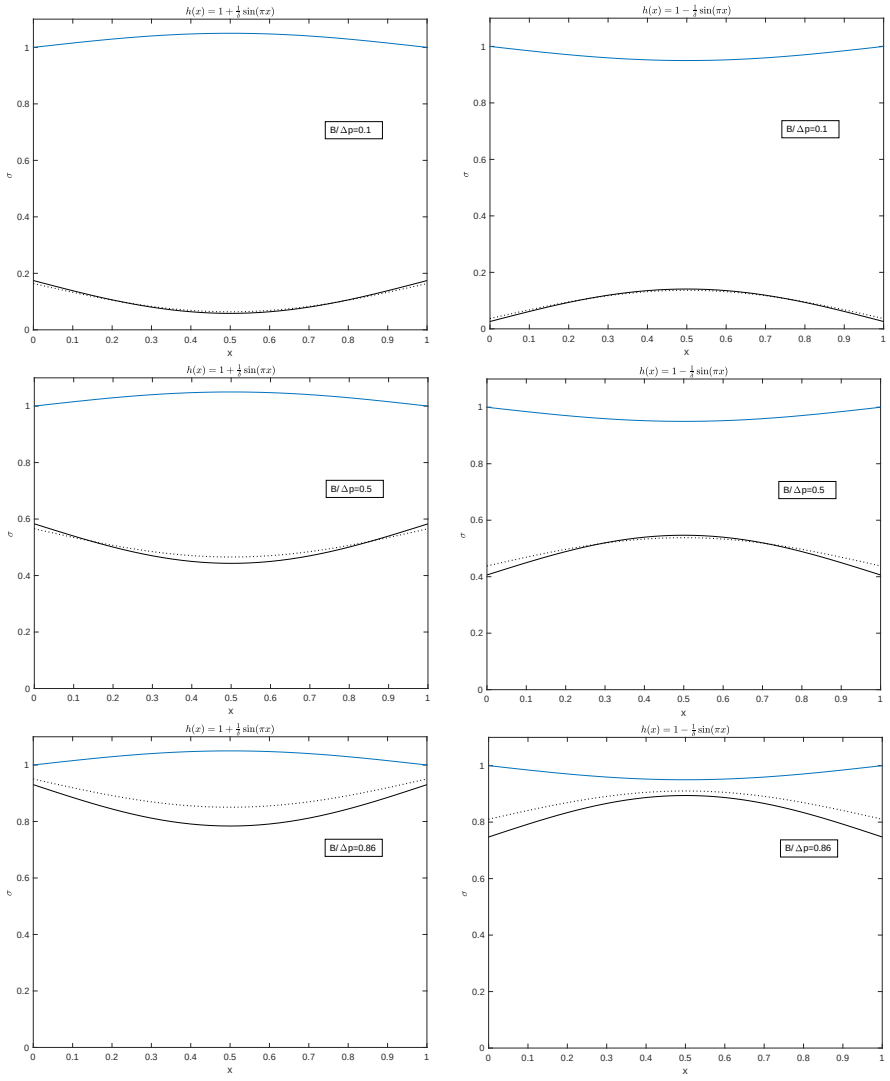

Figure 4.11: Comparisons between $\sigma(x)$ given by (4.50), (4.51), i.e. Casson model, continuous curve, and $\sigma(x)$ given by model (4.64), (4.65), Bingham model, dotted curve.

4.9 Peristaltic Flow

We now consider the case where the duct walls move as traveling waves, i.e. the peristaltic flow. We indeed assume that

$$h(x,t) = 1 + \frac{1}{\delta}\sin(2\pi(x-t)), \tag{4.66}$$

that is a sinusoidal profile whose wave length and speed are equal to 1. Next, the boundary conditions of adhesion on $y = h$, i.e. (4.6), change and become

$$u(x,h,t)=0, \qquad v(x,h,t) = \frac{\partial h}{\partial t}.$$

Recalling (4.25) and following the same approach of Section 4.4, we have that

$$0 = \frac{\partial Q(x,t)}{\partial x} = \frac{\partial}{\partial x}\int_0^{h(x,t)} u dy \underset{(4.12)_1}{=} -\frac{\partial}{\partial x}\int_0^{h(x,t)} \frac{\partial v}{\partial y} dy,$$

which yields

$$\frac{\partial Q}{\partial x} = -\frac{\partial h}{\partial t}.$$

or, because of (4.66),

$$\frac{\partial}{\partial x}(Q-h) = 0,$$

from which we conclude that $Q(x,t)-h(x,t)$ does not depend on x. Now, assuming that the inlet discharge $Q_{in}(t) = Q(0,t)$, we have

$$Q(x,t) - h(x,t) = Q_{in}(t) - h_{in}(t),$$

where $h_{in}(t) = h(0,t)$. Proceeding as in Section 4.7, we insert (4.59) in (4.25) and obtain

$$Q_{in}+h-h_{in}(t) = hu_c - \frac{1}{12}B\mathcal{P}_x^2\frac{(h-\sigma)^4}{4} = hu_c - u_c\frac{(h-\sigma)}{4} = \frac{u_c}{4}(3h-\sigma). \tag{4.67}$$

Now setting

$$\begin{aligned} A(x,t) &= Q_{in}(t) + h(x,t) - h_{in}(t) \\ &= Q_{in}(t) + \frac{1}{\delta}\left[\sin(2\pi(x-t)) + \sin(2\pi t)\right], \end{aligned}$$

rearranging (4.67) yields

$$\sigma(x,t) = \frac{3h(x,t)u_c(t) - 4A}{u_c(t)}, \tag{4.68}$$

with $u_c(t)$ still unknown at this stage. To determine the unknowns (u_c, σ) we exploit $(4.30)_2$ and (4.67) obtaining this system

$$\begin{cases} \int_0^1 \mathcal{P}_x \sigma \, dx = -1, \\ \\ \sigma = \dfrac{3hu_c - 4A}{u_c}. \end{cases} \tag{4.69}$$

To solve this problem we exploit $(4.59)_1$ and (4.68) to determine $\mathcal{P}_x$ as a function of u_c. We thus have

$$\mathcal{P}_x = -\sqrt{\frac{12}{B}} \frac{u_c^2}{(4A - 2hu_c)^{\frac{3}{2}}}, \tag{4.70}$$

where we choose the negative solution according to our assumption about p_x. Now we put (4.70) in $(4.69)_1$ getting

$$\sqrt{\frac{12}{B}} \int_0^1 u_c \frac{3hu_c - 4A}{(4A - 2hu_c)^{\frac{3}{2}}} \, dx = 1, \tag{4.71}$$

with $u_c = u_c(t)$.
To solve equation (4.71), we have to impose some conditions on the integrand function. We require

$$\begin{aligned} 4A - 2hu_c &> 0 \Longrightarrow \frac{u_c}{A} < \frac{2}{h}, \\ 3hu_c - 4A &> 0 \Longrightarrow \frac{u_c}{A} > \frac{4}{3}\frac{1}{h}, \end{aligned}$$

which, setting $\psi(x,t) = \dfrac{u_c(t)}{A(x,t)}$, we rewrite as

$$\frac{4}{3}\frac{1}{h} < \psi < 2\frac{1}{h}.$$

So, rearranging (4.71), we get

$$\sqrt{\frac{12}{B}} \int_0^1 \sqrt{A}\psi \frac{3h\psi - 4}{(4 - 2h\psi)^{\frac{3}{2}}} \, dx = 1. \tag{4.72}$$

So, dividing the time interval $[0,1]$ in n steps, we solve numerically (4.72) at any time step.

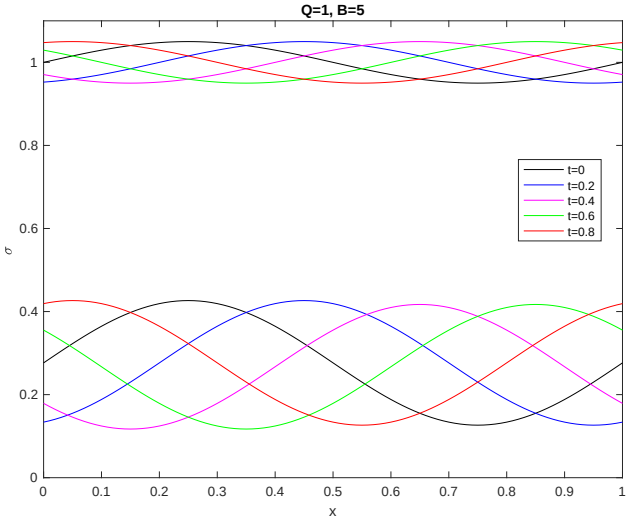

Figure 4.12: Yield surface and the wall profile at five different times. $\delta = 20$, $B = 5$ and $Q(t) \equiv 1$.

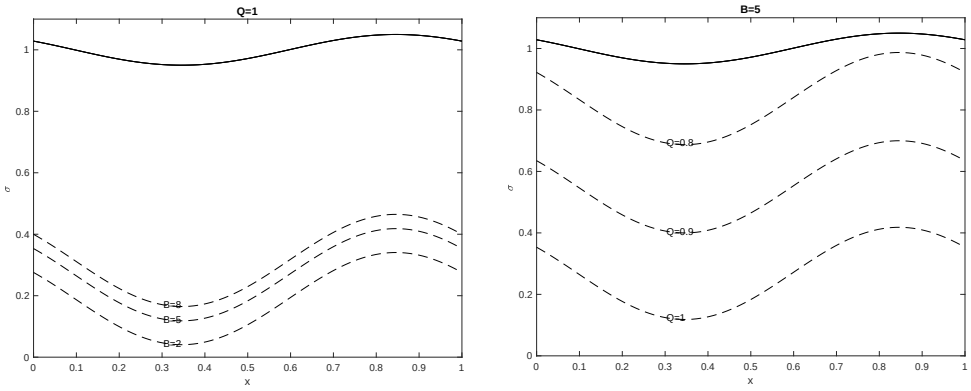

Figure 4.13: Yield surface σ varying the parameters Q and B. On the left panel $Q(t) \equiv 1$ while B varies. On the right panel B is kept constant while Q varies. In both cases we set $\delta = 20$.

4.10 Final remarks

In this chapter we have presented a mathematical model for a Casson flow in a symmetrical channel of varying amplitude, whose walls can move over time as a traveling wave. The formulation of the fluid dynamics problem is obtained by imposing the mass and momentum balance. The latter, written for the central rigid core, results in an integral equation. We have thus determined an explicit expression for the velocity field and for the yield surface (which, being unknown, is a free boundary). The problem has been solved in two cases: (*i*) the driving force of the flow is the pressure difference applied between inlet and outlet; (*iii*) the inlet flow rate is imposed and the walls of the channel are animated by a traveling wave (peristaltic flow). Numerical simulations of the peristaltic flow have shown that as the Bingham number increases and as the flow rate decreases, the yield surface tends to occupy the entire channel. Regarding the analysis of the flow driven by the pressure gradient Δp, a comparison was made between the flow of Bingham and that of Casson. The results obtained seem to show a certain sensitivity to the $B/\Delta p$ parameter. Specifically, the two yield surfaces are very similar when $B/\Delta p \sim 0.5$. As soon as $B/\Delta p$ tends to 0.9, the two surfaces detach significantly. In any case we have found a characteristic of viscoplastic flows in channels of variable amplitude: the yield surface and the channel wall have opposite monotonicity. That is, the plug shrinks (or widens) as the width of the channel increases (or decreases).
The problem addressed, though exceedingly complicated, gives the basis of a new theory for modeling blood as a viscoplastic fluid. Of greatest interest could be the verification of compatibility between results obtained with Newtonian models [36] [38] and those that can be obtained with this new approach. This leaves room for new developments in the future.

Chapter 5

Conclusions

In this thesis, we have essentially dealt with mathematical modeling in hematology. In particular, we have focused on two very particular phenomena that occur at the level of the microcirculation. The first is the Fåhreus-Lindqvist effect, which, as already mentioned, occurs in blood vessels with diameter less than 500-300 micrometers in diameter. Since the discovery of this phenomenon in 1930 and despite various models aiming at a quantitative explanation, the Fåhreus-Lindqvist effect has not been theoretically explained until today. In this work, we have tried to approach the problem in an original way by applying the Prandtl boundary layer theory to a channel entrance flow. This has led to very satisfactory results, although there is still a long way to go towards a model that can fully describe this phenomenon.
The other topic we have addressed is vasomotion, a phenomenon that also occurs at the level of arterioles and venules, i.e., the microcirculation. Again, we have attempted to make a new contribution to existing theories by modeling blood as a viscoplastic Casson fluid. Such work has never been done on vessels with non-parallel walls, except by purely numerical methods. Our approach has led to some significant results that allow effective modeling of blood flow at the microcirculatory level as a viscoplastic fluid.
An interesting future development concerning the Fåhreus-Lindqvist effect could involve three-dimensional flows, for example starting from axisymmetric flows. As for the Casson model, the next step will be to implement it in the model for vasomotion, a model nowadays consider the Newtonian constitutive equation. In particular, it could be of great interest to verify the compatibility between the results obtained considering Newtonian flow and those obtained with the Casson model.

Chapter 6

Appendix

In this chapter we report the explicit expressions of functions $\mathcal{K}_1$, $\mathcal{K}_2$, $\mathcal{K}_3$, $\mathcal{K}_4$, $\mathcal{K}_5$, $\mathcal{W}_3$, $\mathcal{W}_4$ and $\mathcal{W}_5$ which appear in formula (3.29) in chapter 3. Thi expressions have been obtained with computer software MAXIMA® [76]

$$\begin{aligned}\mathcal{K}_1 \;=\; & \frac{1}{8\,\beta}\left[\left(16\,\sinh\left(\sigma\beta\right)\mathrm{e}^{2\,\sigma\beta}\cosh\left(\beta\right)-\mathrm{e}^{4\,\sigma\beta}+\mathrm{e}^{2\,\sigma\beta}\sigma\left(-8\,\left(\cosh\left(\beta\right)\right)^2\beta+\right.\right.\right.\\ & -4\,\beta)+1)\,\mathrm{e}^{-2\,\sigma\beta}-\left(16\,\sinh\left(\beta\right)\cosh\left(\beta\right)\mathrm{e}^{2\,\beta}-8\,\left(\cosh\left(\beta\right)\right)^2\mathrm{e}^{2\,\beta}\cdot\right.\\ & \left.\left.\left.\cdot\,\beta-\mathrm{e}^{4\,\beta}-4\,\mathrm{e}^{2\,\beta}\beta+1\right)\mathrm{e}^{-2\,\beta}\right]\,, \end{aligned} \tag{6.1}$$

$$\begin{aligned}\mathcal{K}_2 \;=\; & \frac{1}{16\,\beta^2}\left[\left(16\,\sinh\left(\sigma\beta\right)\mathrm{e}^{2\,\sigma\beta}\sinh\left(\beta\right)\beta+\mathrm{e}^{4\,\sigma\beta}\left(-2\,\sigma\beta+1\right)+\mathrm{e}^{3\,\sigma\beta}\left(8\,\sigma\cdot\right.\right.\right.\\ & \cdot\cosh\left(\beta\right)\beta-8\,\cosh\left(\beta\right))-16\,\mathrm{e}^{2\,\sigma\beta}\sigma\sinh\left(\beta\right)\cosh\left(\beta\right)\beta^2+\mathrm{e}^{\sigma\beta}\left(8\,\sigma\cdot\right.\\ & \cdot\cosh\left(\beta\right)\beta+8\,\cosh\left(\beta\right))-2\,\sigma\beta-1)\,\mathrm{e}^{-2\,\sigma\beta}-\left(16\,\left(\sinh\left(\beta\right)\right)^2\mathrm{e}^{2\,\beta}\beta+\\ & -16\,\sinh\left(\beta\right)\cosh\left(\beta\right)\mathrm{e}^{2\,\beta}\beta^2+\cosh\left(\beta\right)\left(\mathrm{e}^{3\,\beta}\left(8\,\beta-8\right)+\mathrm{e}^{\beta}\left(8\,\beta+\right.\right.\\ & \left.\left.\left.+8\right)\right)+\mathrm{e}^{4\,\beta}\left(1-2\,\beta\right)-2\,\beta-1\right)\mathrm{e}^{-2\,\beta}\right]\,. \end{aligned} \tag{6.2}$$

$$
\begin{aligned}
\mathcal{K}_3 \;=\; & \frac{1}{8\,\mu\beta}\left(\left(\sinh\left(\sigma\beta\frac{1}{\sqrt{\mu}}\right)\right)^2\left(\sinh\left(\sigma\beta\right)\left(16\,\mathrm{e}^{2\,\frac{\sigma\beta}{\sqrt{\mu}}}\mu\cosh\left(\beta\right)-16\,\cosh\right.\right.\right.\\
& \left.\left.\left.\left(\sigma\beta\right)\mathrm{e}^{2\,\frac{\sigma\beta}{\sqrt{\mu}}}\mu\right)-8\,\left(\cosh\left(\sigma\beta\right)\right)^2\;\mathrm{e}^{2\,\frac{\sigma\beta}{\sqrt{\mu}}}\sigma\mu\beta+16\,\cosh\left(\sigma\beta\right)\mathrm{e}^{2\,\frac{\sigma\beta}{\sqrt{\mu}}}\sigma\mu\cosh\right.\right.\\
& \left.\left.\left(\beta\right)\beta-8\,\mathrm{e}^{2\,\frac{\sigma\beta}{\sqrt{\mu}}}\sigma\mu\left(\cosh\left(\beta\right)\right)^2\beta\right)+\left(\sinh\left(\sigma\beta\frac{1}{\sqrt{\mu}}\right)\cdot\cosh\left(\sigma\beta\frac{1}{\sqrt{\mu}}\right)\cdot\right.\right.\\
& \left.\left.\cdot\left(16\,\left(\sinh\left(\sigma\beta\right)\right)^2\mathrm{e}^{2\,\frac{\sigma\beta}{\sqrt{\mu}}}+\sinh\left(\sigma\beta\right)\left(16\,\cosh\left(\sigma\beta\right)\mathrm{e}^{2\,\frac{\sigma\beta}{\sqrt{\mu}}}\sigma\beta-16\,\mathrm{e}^{2\,\frac{\sigma\beta}{\sqrt{\mu}}}\cdot\right.\right.\right.\right.\\
& \left.\left.\left.\left.\cdot\sigma\cosh\left(\beta\right)\beta\right)+\left(\sinh\left(\sigma\beta\right)\right)^2\left(1-\mathrm{e}^{4\,\frac{\sigma\beta}{\sqrt{\mu}}}\right)\right)\sqrt{\mu}-8\,\left(\cosh\left(\frac{\sigma\beta}{\sqrt{\mu}}\right)\right)^2\cdot\right.\right.\\
& \left.\left.\cdot\left(\sinh\left(\sigma\beta\right)\right)^2\mathrm{e}^{2\,\frac{\sigma\beta}{\sqrt{\mu}}}\sigma\beta-4\,\left(\sinh\left(\sigma\beta\right)\right)^2\mathrm{e}^{2\,\frac{\sigma\beta}{\sqrt{\mu}}}\sigma\beta\right)\cdot\;\mathrm{e}^{-2\,\frac{\sigma\beta}{\sqrt{\mu}}}\left(\sinh\left(\sigma\beta\cdot\right.\right.\right.\\
& \left.\left.\left.\cdot\frac{1}{\sqrt{\mu}}\right)\right)^{-2}-\frac{1}{8\,\mu\beta}\left(\left(\sinh\left(\sigma\beta\frac{1}{\sqrt{\mu}}\right)\right)^2\left(-8\,\left(\cosh\left(\sigma\beta\right)\right)^2\mathrm{e}^{2\,\frac{\beta}{\sqrt{\mu}}}\mu\beta+\right.\right.\right.\\
& \left.\left.\left.+16\,\cosh\left(\sigma\beta\right)\cdot\;\mathrm{e}^{2\,\frac{\beta}{\sqrt{\mu}}}\mu\cosh\left(\beta\right)\beta-8\,\mathrm{e}^{2\,\frac{\beta}{\sqrt{\mu}}}\mu\left(\cosh\left(\beta\right)\right)^2\beta\right)+\left(\sinh\right.\right.\right.\\
& \left.\left.\left.\left(\sigma\beta\frac{1}{\sqrt{\mu}}\right)\cosh\left(\sigma\beta\frac{1}{\sqrt{\mu}}\right)\sinh\left(\sigma\beta\right)\left(16\,\cosh\left(\sigma\beta\right)\cdot\;\mathrm{e}^{2\,\frac{\beta}{\sqrt{\mu}}}\beta-16\,\mathrm{e}^{2\,\frac{\beta}{\sqrt{\mu}}}\cdot\right.\right.\right.\right.\\
& \left.\left.\left.\left.\cdot\cosh\left(\beta\right)\beta\right)+16\,\cosh\left(\frac{\sigma\beta}{\sqrt{\mu}}\right)\left(\sinh\left(\sigma\beta\right)\right)^2\mathrm{e}^{2\,\frac{\beta}{\sqrt{\mu}}}\sinh\left(\frac{\beta}{\sqrt{\mu}}\right)+\left(\sinh\right.\right.\right.\right.\\
& \left.\left.\left.\left.\left(\sigma\beta\right)\right)^2\cdot\left(1-\mathrm{e}^{4\,\frac{\beta}{\sqrt{\mu}}}\right)\right)\sqrt{\mu}+\sinh\left(\sigma\beta\frac{1}{\sqrt{\mu}}\right)\sinh\left(\sigma\beta\right)\left(16\,\mathrm{e}^{2\,\frac{\beta}{\sqrt{\mu}}}\mu\sinh\right.\right.\right.\\
& \left.\left.\left.\left(\frac{\beta}{\sqrt{\mu}}\right)\cosh\left(\beta\right)-16\,\cosh\left(\sigma\beta\right)\cdot\;\mathrm{e}^{2\,\frac{\beta}{\sqrt{\mu}}}\mu\sinh\left(\frac{\beta}{\sqrt{\mu}}\right)\right)-8\,\left(\cosh\right.\right.\right.\\
& \left.\left.\left.\left(\frac{\sigma\beta}{\sqrt{\mu}}\right)\right)^2\left(\sinh\left(\sigma\beta\right)\right)^2\mathrm{e}^{2\,\frac{\beta}{\sqrt{\mu}}}\beta-4\,\left(\sinh\left(\sigma\beta\right)\right)^2\mathrm{e}^{2\,\frac{\beta}{\sqrt{\mu}}}\beta\right)\mathrm{e}^{-2\,\frac{\beta}{\sqrt{\mu}}}\cdot\left(\sinh\right.\right.\right.\\
& \left.\left.\left.\left(\sigma\beta\frac{1}{\sqrt{\mu}}\right)\right)^{-2}\right. \qquad (6.3)
\end{aligned}
$$

$$\mathcal{K}_4 = \frac{\mu^{-\frac{3}{2}}}{16\ \beta^2}\left(\left(\left(\sinh\left(\sigma\beta\frac{1}{\sqrt{\mu}}\right)\right)^3\left(\sinh(\sigma\beta)\left(\cosh(\sigma\beta)\,\sigma\mathrm{e}^{2\frac{\beta}{\sqrt{\mu}}}\left(16\,\mu\ \beta^2+\right.\right.\right.\right.$$

$$-16\ \beta^2\Big)+\sigma\mathrm{e}^{2\frac{\beta}{\sqrt{\mu}}}\left(16\cosh(\beta)\ \beta^2-16\,\mu\cosh(\beta)\ \beta^2\right)\Big)-16\cosh$$

$$(\sigma\beta)\,\mathrm{e}^{2\frac{\beta}{\sqrt{\mu}}}\mu\sinh(\beta)\ \beta^2+16\,\mathrm{e}^{2\frac{\beta}{\sqrt{\mu}}}\mu\sinh(\beta)\cosh(\beta)\ \beta^2\Big)+(\sinh(\sigma\cdot$$

$$\cdot\beta\frac{1}{\sqrt{\mu}}\Big)\Big)^2\left((\sinh(\sigma\beta))^2\,\sigma\mathrm{e}^{2\frac{\beta}{\sqrt{\mu}}}\left(16\,\mu\sinh\left(\frac{\beta}{\sqrt{\mu}}\right)\beta-16\sinh\left(\frac{\beta}{\sqrt{\mu}}\right)\cdot\right.\right.$$

$$\cdot\beta)+\sinh(\sigma\beta)\left(\cosh(\sigma\beta)\left(8\,\mathrm{e}^{\frac{\beta}{\sqrt{\mu}}}\mu-8\,\mathrm{e}^{3\frac{\beta}{\sqrt{\mu}}}\mu\right)+8\,\mathrm{e}^{3\frac{\beta}{\sqrt{\mu}}}\mu\cosh(\beta)+\right.$$

$$\left.-16\,\mathrm{e}^{2\frac{\beta}{\sqrt{\mu}}}\mu\sinh\left(\frac{\beta}{\sqrt{\mu}}\right)\sinh(\beta)\,\beta-8\,\mathrm{e}^{\frac{\beta}{\sqrt{\mu}}}\mu\cosh(\beta)\right)+16\ (\cosh(\sigma\beta))^2\cdot$$

$$\left.\cdot\sigma\mathrm{e}^{2\frac{\beta}{\sqrt{\mu}}}\mu\sinh\left(\frac{\beta}{\sqrt{\mu}}\right)\beta-16\cosh(\sigma\beta)\,\sigma\mathrm{e}^{2\frac{\beta}{\sqrt{\mu}}}\mu\sinh\left(\frac{\beta}{\sqrt{\mu}}\right)\cosh(\beta)\,\beta\right)+$$

$$+\sinh\left(\sigma\beta\frac{1}{\sqrt{\mu}}\right)\left(\left(\cosh\left(\sigma\beta\frac{1}{\sqrt{\mu}}\right)\right)^2\sinh(\sigma\beta)\left(32\cosh(\sigma\beta)\,\sigma\mathrm{e}^{2\frac{\beta}{\sqrt{\mu}}}\cdot\right.\right.$$

$$\left.\cdot\ \beta^2-16\,\sigma\mathrm{e}^{2\frac{\beta}{\sqrt{\mu}}}\cosh(\beta)\ \beta^2\right)+\cosh\left(\sigma\beta\frac{1}{\sqrt{\mu}}\right)(\sinh(\sigma\beta))^2\left(-8\,\mathrm{e}^{3\frac{\beta}{\sqrt{\mu}}}\beta+\right.$$

$$\left.-8\,\mathrm{e}^{\frac{\beta}{\sqrt{\mu}}}\beta\right)+(\sinh(\sigma\beta))^2\left(2\,\mathrm{e}^{4\frac{\beta}{\sqrt{\mu}}}\beta+2\,\beta\right)+8\sinh(\sigma\beta)\cosh(\sigma\beta)\,\sigma\mathrm{e}^{2\frac{\beta}{\sqrt{\mu}}}\cdot$$

$$\left.\cdot\ \beta^2\right)+32\left(\cosh\left(\frac{\sigma\beta}{\sqrt{\mu}}\right)\right)^2(\sinh(\sigma\beta))^2\,\sigma\mathrm{e}^{2\frac{\beta}{\sqrt{\mu}}}\sinh\left(\frac{\beta}{\sqrt{\mu}}\right)\beta+\cosh(\sigma\beta\cdot$$

$$\left.\cdot\frac{1}{\sqrt{\mu}}\right)(\sinh(\sigma\beta))^2\,\sigma\left(2\,\beta-2\,\mathrm{e}^{4\frac{\beta}{\sqrt{\mu}}}\beta\right)\Big)\sqrt{\mu}+\left(\sinh\left(\sigma\beta\frac{1}{\sqrt{\mu}}\right)\right)^2(\cosh$$

$$\left(\sigma\beta\frac{1}{\sqrt{\mu}}\right)\Big((\sinh(\sigma\beta))^2\,\sigma\mathrm{e}^{2\frac{\beta}{\sqrt{\mu}}}\left(-16\,\mu\ \beta^2+16\ \beta^2\right)+16\sinh(\sigma\beta)\,\mathrm{e}^{2\frac{\beta}{\sqrt{\mu}}}\mu\cdot$$

$$\cdot\sinh(\beta)\ \beta^2-16\ (\cosh(\sigma\beta))^2\,\sigma\mathrm{e}^{2\frac{\beta}{\sqrt{\mu}}}\mu\ \beta^2+16\cosh(\sigma\beta)\,\sigma\mathrm{e}^{2\frac{\beta}{\sqrt{\mu}}}\mu\cosh(\beta)\cdot$$

$$\cdot\beta^2\Big)+\sinh(\sigma\beta)\left(\cosh(\sigma\beta)\left(8\,\mathrm{e}^{3\frac{\beta}{\sqrt{\mu}}}\mu\beta+8\,\mathrm{e}^{\frac{\beta}{\sqrt{\mu}}}\mu\beta\right)-8\,\mathrm{e}^{3\frac{\beta}{\sqrt{\mu}}}\mu\cosh(\beta)\,\beta+\right.$$

$$\left.-8\,\mathrm{e}^{\frac{\beta}{\sqrt{\mu}}}\mu\cosh(\beta)\,\beta\right)\Big)+\sinh\left(\sigma\beta\frac{1}{\sqrt{\mu}}\right)\left(\cosh\left(\sigma\beta\frac{1}{\sqrt{\mu}}\right)\Big((\sinh(\sigma\beta))^2\,(8\cdot\right.$$

$$\left.\cdot\mathrm{e}^{3\frac{\beta}{\sqrt{\mu}}}\mu-8\,\mathrm{e}^{\frac{\beta}{\sqrt{\mu}}}\mu\right)+\sinh(\sigma\beta)\left(16\,\sigma\mathrm{e}^{2\frac{\beta}{\sqrt{\mu}}}\mu\sinh\left(\frac{\beta}{\sqrt{\mu}}\right)\cosh(\beta)\,\beta-48\cosh\right.$$

$$(\sigma\beta)\,\sigma \mathrm{e}^{2\,\frac{\beta}{\sqrt{\mu}}}\mu\sinh\left(\frac{\beta}{\sqrt{\mu}}\right)\beta\Big)\Big)+(\sinh(\sigma\beta))^2\left(\mu-\mathrm{e}^{4\,\frac{\beta}{\sqrt{\mu}}}\mu\right)+\sinh(\sigma\beta)\cosh$$

$$(\sigma\beta)\,\sigma\left(2\,\mathrm{e}^{4\,\frac{\beta}{\sqrt{\mu}}}\mu\beta-2\,\mu\beta\right)\Big)-16\,\left(\cosh\left(\frac{\sigma\beta}{\sqrt{\mu}}\right)\right)^3(\sinh(\sigma\beta))^2\,\sigma\mathrm{e}^{2\,\frac{\beta}{\sqrt{\mu}}}\,\beta^2-8\cdot$$

$$\cdot\cosh\left(\frac{\sigma\beta}{\sqrt{\mu}}\right)(\sinh(\sigma\beta))^2\,\sigma\mathrm{e}^{2\,\frac{\beta}{\sqrt{\mu}}}\,\beta^2\Big)\,\mathrm{e}^{-2\,\frac{\beta}{\sqrt{\mu}}}\left(\sinh\left(\sigma\beta\frac{1}{\sqrt{\mu}}\right)\right)^{-3}-\frac{\mu^{-\frac{3}{2}}}{16\,\beta^2}\cdot$$

$$\cdot\Bigg(\left(\left(\sinh\left(\sigma\beta\frac{1}{\sqrt{\mu}}\right)\right)^3\Big((\sinh(\sigma\beta))^2\,\mathrm{e}^{2\,\frac{\sigma\beta}{\sqrt{\mu}}}\sigma\,(16\,\mu\beta-16\,\beta)+\sinh(\sigma\beta)\,(\cosh$$

$$(\sigma\beta)\,\mathrm{e}^{2\,\frac{\sigma\beta}{\sqrt{\mu}}}\sigma^2\left(16\,\mu\,\beta^2-16\,\beta^2\right)+\mathrm{e}^{2\,\frac{\sigma\beta}{\sqrt{\mu}}}\left(\sigma^2\left(16\,\cosh(\beta)\,\beta^2-16\,\mu\cosh(\beta)\,\beta^2\right)+\right.$$

$$\left.-16\,\mu\sinh(\beta)\,\beta\right))+16\,(\cosh(\sigma\beta))^2\,\mathrm{e}^{2\,\frac{\sigma\beta}{\sqrt{\mu}}}\sigma\mu\beta+\cosh(\sigma\beta)\,\mathrm{e}^{2\,\frac{\sigma\beta}{\sqrt{\mu}}}\sigma\mu\,(-16\,\sinh(\beta)\cdot$$

$$\cdot\,\beta^2-16\,\cosh(\beta)\,\beta\Big)+16\,\mathrm{e}^{2\,\frac{\sigma\beta}{\sqrt{\mu}}}\sigma\mu\sinh(\beta)\cosh(\beta)\,\beta^2\Big)+\left(\sinh\left(\sigma\beta\frac{1}{\sqrt{\mu}}\right)\right)^2\cdot$$

$$\cdot\sinh(\sigma\beta)\left(\cosh(\sigma\beta)\left(8\,\mathrm{e}^{\frac{\sigma\beta}{\sqrt{\mu}}}\mu-8\,\mathrm{e}^{3\,\frac{\sigma\beta}{\sqrt{\mu}}}\mu\right)+8\,\mathrm{e}^{3\,\frac{\sigma\beta}{\sqrt{\mu}}}\mu\cosh(\beta)-8\,\mathrm{e}^{\frac{\sigma\beta}{\sqrt{\mu}}}\mu\cosh(\beta)\right)+$$

$$+\sinh\left(\sigma\beta\frac{1}{\sqrt{\mu}}\right)\Bigg(\left(\cosh\left(\sigma\beta\frac{1}{\sqrt{\mu}}\right)\right)^2\Big(32\,(\sinh(\sigma\beta))^2\,\mathrm{e}^{2\,\frac{\sigma\beta}{\sqrt{\mu}}}\sigma\beta+\sinh(\sigma\beta)\,(32\cdot$$

$$\cdot\cosh(\sigma\beta)\,\mathrm{e}^{2\,\frac{\sigma\beta}{\sqrt{\mu}}}\sigma^2\,\beta^2-16\,\mathrm{e}^{2\,\frac{\sigma\beta}{\sqrt{\mu}}}\sigma^2\cosh(\beta)\,\beta^2\Big)\Big)+\cosh\left(\sigma\beta\frac{1}{\sqrt{\mu}}\right)(\sinh(\sigma\beta))^2\cdot$$

$$\cdot\left(-8\,\mathrm{e}^{3\,\frac{\sigma\beta}{\sqrt{\mu}}}\sigma\beta-8\,\mathrm{e}^{\frac{\sigma\beta}{\sqrt{\mu}}}\sigma\beta\right)+(\sinh(\sigma\beta))^2\left(2\,\mathrm{e}^{4\,\frac{\sigma\beta}{\sqrt{\mu}}}\sigma\beta+2\,\sigma\beta\right)+8\,\sinh(\sigma\beta)\cosh$$

$$(\sigma\beta)\,\mathrm{e}^{2\,\frac{\sigma\beta}{\sqrt{\mu}}}\sigma^2\,\beta^2\Big)+\cosh\left(\sigma\beta\frac{1}{\sqrt{\mu}}\right)(\sinh(\sigma\beta))^2\left(2\,\sigma\beta-2\,\mathrm{e}^{4\,\frac{\sigma\beta}{\sqrt{\mu}}}\sigma\beta\right)\Big)\sqrt{\mu}+(\sinh$$

$$\left(\sigma\beta\frac{1}{\sqrt{\mu}}\right)\Big)^2\left(\cosh\left(\sigma\beta\frac{1}{\sqrt{\mu}}\right)\Big((\sinh(\sigma\beta))^2\,\mathrm{e}^{2\,\frac{\sigma\beta}{\sqrt{\mu}}}\sigma^2\left(-16\,\mu\,\beta^2+16\,\beta^2\right)+\sinh(\sigma\cdot\right.$$

$$\left.\cdot\beta)\left(\mathrm{e}^{2\,\frac{\sigma\beta}{\sqrt{\mu}}}\sigma\mu\left(16\,\sinh(\beta)\,\beta^2+16\,\cosh(\beta)\,\beta\right)-48\,\cosh(\sigma\beta)\,\mathrm{e}^{2\,\frac{\sigma\beta}{\sqrt{\mu}}}\sigma\mu\beta\right)-16\,(\cosh\right.$$

$$\left.(\sigma\beta))^2\,\mathrm{e}^{2\,\frac{\sigma\beta}{\sqrt{\mu}}}\sigma^2\mu\,\beta^2+16\,\cosh(\sigma\beta)\,\mathrm{e}^{2\,\frac{\sigma\beta}{\sqrt{\mu}}}\sigma^2\mu\cosh(\beta)\,\beta^2\right)+\sinh(\sigma\beta)\,(\cosh(\sigma\beta)\,(8\cdot$$

$$\left.\cdot\mathrm{e}^{3\,\frac{\sigma\beta}{\sqrt{\mu}}}\sigma\mu\beta+8\,\mathrm{e}^{\frac{\sigma\beta}{\sqrt{\mu}}}\sigma\mu\beta\right)-8\,\mathrm{e}^{3\,\frac{\sigma\beta}{\sqrt{\mu}}}\sigma\mu\cosh(\beta)\,\beta-8\,\mathrm{e}^{\frac{\sigma\beta}{\sqrt{\mu}}}\sigma\mu\cosh(\beta)\,\beta\Big)\Big)+\sinh(\sigma\beta\cdot$$

$$\left.\cdot\frac{1}{\sqrt{\mu}}\right)\left(\cosh\left(\sigma\beta\frac{1}{\sqrt{\mu}}\right)(\sinh(\sigma\beta))^2\left(8\,\mathrm{e}^{3\,\frac{\sigma\beta}{\sqrt{\mu}}}\mu-8\,\mathrm{e}^{\frac{\sigma\beta}{\sqrt{\mu}}}\mu\right)+(\sinh(\sigma\beta))^2\left(\mu-\mathrm{e}^{4\,\frac{\sigma\beta}{\sqrt{\mu}}}\cdot\right.\right.$$

$$\cdot\mu) + \sinh(\sigma\beta)\cosh(\sigma\beta)\left(2\,\mathrm{e}^{4\,\frac{\sigma\beta}{\sqrt{\mu}}}\sigma\mu\beta - 2\,\sigma\mu\beta\right)\Big) - 16\,\left(\cosh\left(\frac{\sigma\beta}{\sqrt{\mu}}\right)\right)^3$$
$$(\sinh(\sigma\beta))^2\,\mathrm{e}^{2\,\frac{\sigma\beta}{\sqrt{\mu}}}\sigma^2\;\beta^2 - 8\,\cosh\left(\frac{\sigma\beta}{\sqrt{\mu}}\right)(\sinh(\sigma\beta))^2\,\mathrm{e}^{2\,\frac{\sigma\beta}{\sqrt{\mu}}}\sigma^2\;\beta^2\Bigg)\mathrm{e}^{-2\,\frac{\sigma\beta}{\sqrt{\mu}}}$$
$$\left(\sinh\left(\sigma\beta\frac{1}{\sqrt{\mu}}\right)\right)^{-3} \tag{6.4}$$

$$\begin{aligned}
\mathcal{K}_5 \;=\; & \frac{1}{8\;\mu^2}\Bigg(\left(\sinh\left(\sigma\beta\frac{1}{\sqrt{\mu}}\right)\right)^3\Big((\sinh(\sigma\beta))^2\,\mathrm{e}^{2\,\frac{\sigma\beta}{\sqrt{\mu}}}\left(-8\;\mu^2+8\,\mu\right)\sinh \\
& (\sigma\beta)\Big(\cosh(\sigma\beta)\,\mathrm{e}^{2\,\frac{\sigma\beta}{\sqrt{\mu}}}\sigma\left(-8\;\mu^2\beta+8\,\mu\beta\right)+\mathrm{e}^{2\,\frac{\sigma\beta}{\sqrt{\mu}}}\sigma\left(8\;\mu^2\cosh(\beta)\cdot\right. \\
& \left.\cdot\beta-8\,\mu\cosh(\beta)\,\beta\right)\Big)-8\;(\cosh(\sigma\beta))^2\,\mathrm{e}^{2\,\frac{\sigma\beta}{\sqrt{\mu}}}\;\mu^2+8\cosh(\sigma\beta)\,\mathrm{e}^{2\,\frac{\sigma\beta}{\sqrt{\mu}}}\cdot \\
& \cdot\mu^2\cosh(\beta)\Big)+\left(\left(\sinh\left(\sigma\beta\frac{1}{\sqrt{\mu}}\right)\right)^2\cosh\left(\sigma\beta\frac{1}{\sqrt{\mu}}\right)\Big((\sinh(\sigma\beta))^2\cdot\right. \\
& \cdot\mathrm{e}^{2\,\frac{\sigma\beta}{\sqrt{\mu}}}\sigma\left(8\,\mu\beta-8\,\beta\right)+\sinh(\sigma\beta)\Big(24\;\cosh(\sigma\beta)\,\mathrm{e}^{2\,\frac{\sigma\beta}{\sqrt{\mu}}}\mu-8\,\mathrm{e}^{2\,\frac{\sigma\beta}{\sqrt{\mu}}}\mu\cdot \\
& \cdot\cosh(\beta))+8\;(\cosh(\sigma\beta))^2\,\mathrm{e}^{2\,\frac{\sigma\beta}{\sqrt{\mu}}}\sigma\mu\beta-8\;\cosh(\sigma\beta)\,\mathrm{e}^{2\,\frac{\sigma\beta}{\sqrt{\mu}}}\sigma\mu\cosh \\
& (\beta)\,\beta)+\sinh\left(\sigma\beta\frac{1}{\sqrt{\mu}}\right)\sinh(\sigma\beta)\cosh(\sigma\beta)\left(\mu-\mathrm{e}^{4\,\frac{\sigma\beta}{\sqrt{\mu}}}\mu\right)+8\cdot \\
& \cdot\left(\cosh\left(\frac{\sigma\beta}{\sqrt{\mu}}\right)\right)^3(\sinh(\sigma\beta))^2\,\mathrm{e}^{2\,\frac{\sigma\beta}{\sqrt{\mu}}}\sigma\beta+4\;\cosh\left(\frac{\sigma\beta}{\sqrt{\mu}}\right)(\sinh(\sigma\cdot \\
& \left.\cdot\beta))^2\,\mathrm{e}^{2\,\frac{\sigma\beta}{\sqrt{\mu}}}\sigma\beta\right)\sqrt{\mu}+\sinh\left(\sigma\beta\frac{1}{\sqrt{\mu}}\right)\left(\left(\cosh\left(\sigma\beta\frac{1}{\sqrt{\mu}}\right)\right)^2(\sinh\right. \\
& (\sigma\beta)\left(8\,\mathrm{e}^{2\,\frac{\sigma\beta}{\sqrt{\mu}}}\sigma\mu\cosh(\beta)\,\beta-16\;\cosh(\sigma\beta)\,\mathrm{e}^{2\,\frac{\sigma\beta}{\sqrt{\mu}}}\sigma\mu\beta\right)-16\;(\sinh \\
& \left.(\sigma\beta))^2\,\mathrm{e}^{2\,\frac{\sigma\beta}{\sqrt{\mu}}}\mu\right)-4\;\sinh(\sigma\beta)\cosh(\sigma\beta)\,\mathrm{e}^{2\,\frac{\sigma\beta}{\sqrt{\mu}}}\sigma\mu\beta\Big)+\cosh(\sigma\beta\cdot \\
& \left.\cdot\frac{1}{\sqrt{\mu}}\right)(\sinh(\sigma\beta))^2\left(\mathrm{e}^{4\,\frac{\sigma\beta}{\sqrt{\mu}}}\mu-\mu\right)\Big)\,\mathrm{e}^{-2\,\frac{\sigma\beta}{\sqrt{\mu}}}\left(\sinh\left(\sigma\beta\frac{1}{\sqrt{\mu}}\right)\right)^{-3}+ \\
& -\frac{1}{8\;\mu^2}\Bigg(\left(\sinh\left(\sigma\beta\frac{1}{\sqrt{\mu}}\right)\right)^3\sinh(\sigma\beta)\Big(\cosh(\sigma\beta)\,\mathrm{e}^{2\,\frac{\beta}{\sqrt{\mu}}}\left(-8\;\mu^2\beta+\right.\right.
\end{aligned}$$

$$+8\,\mu\beta) + \mathrm{e}^{2\,\frac{\beta}{\sqrt{\mu}}}\left(8\ \mu^2\cosh(\beta)\,\beta - 8\,\mu\cosh(\beta)\,\beta\right)\Big) + ((\sinh(\sigma\beta\cdot$$

$$\cdot\frac{1}{\sqrt{\mu}}\Big)\Big)^2\cosh\left(\sigma\beta\frac{1}{\sqrt{\mu}}\right)\Big((\sinh(\sigma\beta))^2\,\mathrm{e}^{2\,\frac{\beta}{\sqrt{\mu}}}\,(8\,\mu\beta - 8\,\beta) + 8\ (\cosh(\sigma\cdot$$

$$\cdot\beta))^2\,\mathrm{e}^{2\,\frac{\beta}{\sqrt{\mu}}}\mu\beta - 8\ \cosh(\sigma\beta)\,\mathrm{e}^{2\,\frac{\beta}{\sqrt{\mu}}}\mu\cosh(\beta)\,\beta\Big) + \sinh\left(\sigma\beta\frac{1}{\sqrt{\mu}}\right)(\cosh$$

$$\left(\sigma\beta\frac{1}{\sqrt{\mu}}\right)\sinh(\sigma\beta)\left(24\ \cosh(\sigma\beta)\,\mathrm{e}^{2\,\frac{\beta}{\sqrt{\mu}}}\mu\sinh\left(\frac{\beta}{\sqrt{\mu}}\right) - 8\,\mathrm{e}^{2\,\frac{\beta}{\sqrt{\mu}}}\mu\sinh\right.$$

$$\left.\left(\frac{\beta}{\sqrt{\mu}}\right)\cosh(\beta)\right) + \sinh(\sigma\beta)\cosh(\sigma\beta)\left(\mu - \mathrm{e}^{4\,\frac{\beta}{\sqrt{\mu}}}\mu\right)\Big) + 8\ \left(\cosh\left(\frac{\sigma\beta}{\sqrt{\mu}}\right)\right)^3\cdot$$

$$\cdot(\sinh(\sigma\beta))^2\,\mathrm{e}^{2\,\frac{\beta}{\sqrt{\mu}}}\beta + 4\ \cosh\left(\frac{\sigma\beta}{\sqrt{\mu}}\right)(\sinh(\sigma\beta))^2\,\mathrm{e}^{2\,\frac{\beta}{\sqrt{\mu}}}\beta\Big)\sqrt{\mu} + (\sinh(\sigma\beta\cdot$$

$$\cdot\frac{1}{\sqrt{\mu}}\Big)\Big)^2\left((\sinh(\sigma\beta))^2\,\mathrm{e}^{2\,\frac{\beta}{\sqrt{\mu}}}\left(8\,\mu\sinh\left(\frac{\beta}{\sqrt{\mu}}\right) - 8\,\mu^2\sinh\left(\frac{\beta}{\sqrt{\mu}}\right)\right) - 8\ (\cosh\right.$$

$$\left.(\sigma\beta))^2\,\mathrm{e}^{2\,\frac{\beta}{\sqrt{\mu}}}\mu^2\sinh\left(\frac{\beta}{\sqrt{\mu}}\right) + 8\ \cosh(\sigma\beta)\,\mathrm{e}^{2\,\frac{\beta}{\sqrt{\mu}}}\mu^2\sinh\left(\frac{\beta}{\sqrt{\mu}}\right)\cosh(\beta)\right)\sinh$$

$$\left(\sigma\beta\frac{1}{\sqrt{\mu}}\right)\left(\left(\cosh\left(\sigma\beta\frac{1}{\sqrt{\mu}}\right)\right)^2\sinh(\sigma\beta)\left(8\,\mathrm{e}^{2\,\frac{\beta}{\sqrt{\mu}}}\mu\cosh(\beta)\,\beta - 16\ \cosh(\sigma\beta)\cdot\right.\right.$$

$$\left.\left.\cdot\mathrm{e}^{2\,\frac{\beta}{\sqrt{\mu}}}\mu\beta\right) - 4\ \sinh(\sigma\beta)\cosh(\sigma\beta)\,\mathrm{e}^{2\,\frac{\beta}{\sqrt{\mu}}}\mu\beta\right) - 16\ \left(\cosh\left(\frac{\sigma\beta}{\sqrt{\mu}}\right)\right)^2(\sinh(\sigma\cdot$$

$$\cdot\beta))^2\,\mathrm{e}^{2\,\frac{\beta}{\sqrt{\mu}}}\mu\sinh\left(\frac{\beta}{\sqrt{\mu}}\right) + \cosh\left(\sigma\beta\frac{1}{\sqrt{\mu}}\right)(\sinh(\sigma\beta))^2\left(\mathrm{e}^{4\,\frac{\beta}{\sqrt{\mu}}}\mu - \mu\right)\Big)\,\mathrm{e}^{-2\,\frac{\beta}{\sqrt{\mu}}}\cdot$$

$$\cdot\left(\sinh\left(\sigma\beta\frac{1}{\sqrt{\mu}}\right)\right)^{-3}, \tag{6.5}$$

$$\mathcal{W}_3 = \left(\sinh(\sigma\beta)\left(1 - \cosh\left(\sigma\beta\frac{1}{\sqrt{\mu}}\right)\right)\left(\sinh\left(\sigma\beta\frac{1}{\sqrt{\mu}}\right)\right)^{-1}\frac{1}{\sqrt{\mu}} + \cosh(\sigma\beta) + \right.$$

$$\left. - \cosh(\beta)\right)^2, \tag{6.6}$$

$$\begin{aligned}\mathcal{W}_4 &= \left(\sinh(\sigma\beta)\left(1-\cosh\left(\sigma\beta\frac{1}{\sqrt{\mu}}\right)\right)\left(\sinh\left(\sigma\beta\frac{1}{\sqrt{\mu}}\right)\right)^{-1}\frac{1}{\sqrt{\mu}}+\cosh\right.\\ &(\sigma\beta)-\cosh(\beta))\left(\cosh(\sigma\beta)\,\sigma\left(1-\cosh\left(\sigma\beta\frac{1}{\sqrt{\mu}}\right)\right)(\sinh(\sigma\beta\cdot\right.\\ &\left.\cdot\frac{1}{\sqrt{\mu}}\right)\Big)^{-1}\frac{1}{\sqrt{\mu}}-\frac{\sinh(\sigma\beta)\,\sigma}{\mu}\cosh\left(\sigma\beta\frac{1}{\sqrt{\mu}}\right)\left(1-\cosh\left(\sigma\beta\frac{1}{\sqrt{\mu}}\right)\right)\cdot\\ &\left.\cdot\left(\sinh\left(\sigma\beta\frac{1}{\sqrt{\mu}}\right)\right)^{-2}-\frac{\sinh(\sigma\beta)\,\sigma}{\mu}+\sinh(\sigma\beta)\,\sigma-\sinh(\beta)\right),\end{aligned} \tag{6.7}$$

$$\begin{aligned}\mathcal{W}_5 &= \left(\sinh(\sigma\beta)\left(1-\cosh\left(\sigma\beta\frac{1}{\sqrt{\mu}}\right)\right)\left(\sinh\left(\sigma\beta\frac{1}{\sqrt{\mu}}\right)\right)^{-1}\frac{1}{\sqrt{\mu}}+\cosh\right.\\ &(\sigma\beta)-\cosh(\beta))\left(\cosh(\sigma\beta)\,\beta\left(1-\cosh\left(\sigma\beta\frac{1}{\sqrt{\mu}}\right)\right)(\sinh(\sigma\beta\cdot\right.\\ &\left.\cdot\frac{1}{\sqrt{\mu}}\right)\Big)^{-1}\frac{1}{\sqrt{\mu}}-\frac{\sinh(\sigma\beta)\,\beta}{\mu}\cosh\left(\sigma\beta\frac{1}{\sqrt{\mu}}\right)\left(1-\cosh\left(\sigma\beta\frac{1}{\sqrt{\mu}}\right)\right)\cdot\\ &\left.\cdot\left(\sinh\left(\sigma\beta\frac{1}{\sqrt{\mu}}\right)\right)^{-2}-\frac{\sinh(\sigma\beta)\,\beta}{\mu}+\sinh(\sigma\beta)\,\beta\right).\end{aligned} \tag{6.8}$$

Bibliography

[1] Abbott J.R., Tetlow N., Graham A.L., Altobelli S.A., Fukushima E., Mondy L.A., Stephens S.T. Experimental observations of particle migration in concentrated suspensions: couette flow, J. Rheol. 35, 773–795 (1991).

[2] Ahnert T., Münch A., Wagner B., Models for the two-phase flow of concentrated suspensions, Eur. J. Appl. Math. 30, 585-617 (2019).

[3] Aird W.C., Discovery of the cardiovascular system: from Galen to William Harvey. J. Thromb. Haemost. 9 (Suppl. 1), 118-129 (2011).

[4] Anand M., Rajagopal K., A note on the flows of inhomogeneous fluids with shear-dependent viscosities, Archives of Mechanics 57, 417–428 (2005).

[5] Anderson T.B., Jackson R., Fluid mechanical description of fluidized beds, Ind. Eng. Chem. Fund. 7, 12-21 (1968).

[6] Arp P.A., Mason S.G., Kinetics of flowing dispersions. 9. Doublets of rigid spheres,J. Colloid Interface Sci. 61, 44–61 (1977).

[7] Ascolese M., Angiolo F., Fasano A.: The Fåhraeus-Lindqvist effect in small blood vessels: how does it alleviate the heart? J. Biol. Phys. (2019)

[8] Barnes H.A., Thixotropy- a review. J. Non-Newtonian Fluid Mech. 70, 1-33 (1997)

[9] Barnes H.A., Hutton J.F., Walters K., An introduction to rheology, Amsterdam, Elsevier, 1989.

[10] Batchelor G.K., Green J.T., The hydrodynamic interaction of two small freely moving spheres in a linear flow field, J, Fluid Mech, 56, 375–400 (1972).

[11] Batchelor G.K., Green J.T., The determination of the bulk stress in a suspension of spherical particles to order c^2, J. Fluid Mech. 56, 401–427 (1972).

[12] Batchelor G.K., The effect of Brownian motion on the bulk stress in a suspension of spherical particles, J. Fluid Mech. 83, 97–117 (1977).

[13] Beale L.S., The Microscope in Medicine (J. & A. Churchill, London, 1877)

[14] Bercovier M., Engelman M., A finite-element method for incompressible non-Newtonian flows, J. Comput. Phys., 36 (1980) 313–326.

[15] Bingham E.C., An investigation of the laws of plastic flow. U.S. Bur. Stand. Bull. 13, 309-353 (1916)

[16] Bingham E.C., Fluidity and Plasticity, McGraw-Hill, New York, 1922.

[17] Bird R.B., Dai G.C., Yarusso B.J., The rheology and flow of viscoplastic materials, Rev. Chem. Eng., 1 (1983) 1–70.

[18] Bird B., Armstrong R. C., Hassager O., Dynamics of Polymeric Liquids: Volume 1 Fluid Mechanics, John Wiley & Sons, 1987.

[19] Bodoia J.R., Osterle J.F., Finite difference analysis of plane Poiseuille and Couette flow developments, Appl. Sci. Res. 16, 265-276 (1961).

[20] Boyer F., Guazzelli E., Pouliquen O., Unifying suspension and granular rheology, Phys. Rev. Lett. 107, 188301-6 (2011).

[21] Campbell W.D., Slattery J. C., Flow in the entrance of a tube, J. Basic Eng. 85, 41-45, (1963).

[22] Casson N., Rheology of disperse systems, Ed. C.C. Mill, Pergamon Press, Oxford (1959).

[23] Chandran K. B., Yoganathan A. P., Rittgers S. E., Biofluid Mechanics. The Human Circulation, CRC, 2007.

[24] Chang C.Y., Powell R.L., Effect of particle size distributions on the rheology of concentrated bimodal suspensions, J. Rheol. 38, 85–98 (1994).

[25] Chinnayya A., Chtaba A., Shao J.Q., Carter R.M., Yan Y., Caillat S., Characterization of pneumatic transportation of pulverised coal in a horizontal pipeline through measurement and computational modelling, Fuel 88, 2348-2356 (2009).

[26] Coirier J., Mécanique des milieux continus, Dunod, Paris, 1997.

[27] Collins M., W. R. Schowalter, Laminar flow in the inlet region of a straight channel, Phys. Fluids 5, 1122-1124 (1962).

[28] Cooney D.O., Biomedical Engineering Principles: An Introduction to Fluid, Heat and Mass Transport Processes, Marcel Dekker, 1976.

[29] Chien S., King R.G., Skalak R., Usami S., Copley A.L., Viscoelastic properties of human blood and red cell suspensions. Biorheology 12, 341-346 (1975)

[30] Dintenfass L., Blood Microrheology - Viscosity Factors in Blood Flow. Ischaemia and Thrombosis (Butterworth, Oxford, 1971)

[31] Dongaonkar R.M., Quick C.M., Vo J.C., Meisner J.K., Laine G.A., Davis M.J., Stewart R.H., Blood flow augmentation by intrinsic venular contraction in vivo. Am. J. Phys. Regul. Integr. Comp. Physiol. 302, R1436-R1442 (2012)

[32] Drew D.A., Passman, S.L., Theory of multicomponent fluids (Vol. 135). Springer Science and Business Media, 2006.

[33] Einstein A., Eine neue bestimmung der molekűledimensionen, Annal Phys. 19, 289–306 (1906).

[34] Evans E.A., Hochmuth R.M., Membrane viscoelasticity. Biophys. J. 16(1), 1-11 (1976)

[35] Fåhraeus R., Lindqvist T., The viscosity of blood in narrow capillary tubes. Am. J. Physiol. 96, 362-368 (1931)

[36] Farina A., Fasano A., Rosso F., Mathematical models for some aspects of blood microcirculation, Symmetry, 13 (2021) 1020. doi.org/10.3390/sym13061020

[37] Farina A., Fusi L., Viscoplastic fluids: Mathematical modeling and applications, in Non-Newtonian Fluid Mechanics and Complex Flows. C.I.M.E. Summer School, Levico Terme, 2016, Lecture Notes in Mathematics 2212, A. Farina, A. Mikelic, F. Rosso, Ed.s, 229-298, Springer, (2018).

[38] Farina A., Fusi L., Fasano A., Ceretani A., Rosso F., Modeling peristaltic flow in vessels equipped with valves: Implications for vasomotion in bat wing venules. Int. J. Eng. Sci. 2016, 107, 1-12.

[39] Fasano A., Sequeira A., Hemomath: The Mathematics of Blood, Springer-Verlag, Berlin-Heidelberg, (2017).

[40] Fedosov D.A., Caswell B., Karniadakis G.E.: A multiscale red blood cell model with accurate mechanics, rheology, and dynamics. Biophys. J. 98:2215-25, (2010)

[41] Fedosov D.A., Caswell B., Popel A.S., Karniadakis G.E.: Blood flow and cell-free layer in microvessels Microcirculation. 17:615-28, (2010)

[42] Fincke A., Beitrage zur Losung Rheologischer Probleme in Der Schokoladentechnologie, Dissertation, TH Karlsruhe, 1961.

[43] Frigaard I.A., Nouar C., On the usage of viscosity regularization methods for visco-plastic fluid flow computation, J. Non-Newtonian Fluid Mech., 127 (2005) 1-26.

[44] Fusi L., Farina A., Rosso F., Rajagopal K., Thin-film flow of an inhomogeneous fluid with density-dependent viscosity, Fluids 4, 30 (2019).

[45] Fusi L., Farina A., Rosso F., Roscani S., Pressure driven lubrication flow of a Bingham fluid in a channel: a novel approach, J. Non Newt. Fluid Mech. 221 (2015) 66–75.

[46] Fusi L., Farina A., Rosso F., Planar squeeze flow of a Bingham fluid, J. Non Nnewt. Fluid Mech. 225 (2015) 1–9.

[47] Fusi L., Lubrication flow of a generalized Casson fluid with pressure-dependent rheological parameters, J. Non-Newt. Fluid Mech. 274 (2019) 104199.

[48] Gadala-Maria F., Acrivos A., Shear induced structure in a concentrated suspension of solid spheres, J. Rheol. 24, 799–815 (1980).

[49] Galappatti G., Vreugdenhil C.B., A depth-integrated model for suspended sediment transport, J. Hydraulic Res. 23, 359-377 (1985).

[50] Gessner T., Sperandio M.B., Gross J.F., Gaehtgens P.: Resistance to blood flow in microvessels in vivo. Circ. Res. 75:904-15, (1994)

[51] Golubitsky M., Krupa M., Lim C., Time-Reversibility and particle sedimentation, SIAM J. Appl. Math. 51, 49–72 (1991).

[52] Göz M.E, On the origin of wave patterns in fluidized beds, J. Fluid Mech. 240, 379-404 (1992).

[53] Gratton R.J., Gandley R.E., McCarthy J.F., Michaluk W.K., Slinker B.K., McLaughlin M.K., Contribution of vasomotion to vascular resistance: a comparison of arteries from virgin and pregnant rats. J. Appl. Physiol. 85, 2255-2260 (1998)

[54] Guadagni S., Farina A., Entrance flow of a suspension and particles migration towards the vessel center. International Journal of Non-Linear Mechanics. Volume 126, (2020).

[55] Guadagni S., Palade L.I., Fusi L., Farina A., On a Casson Fluid Motion: Nonuniform Width Symmetric Channel and Peristaltic Flows. Fluids, 6, 356 (2021).

[56] Hampton R.E., Mammoli A.A., Graham A.L., Tetlow N., Altobelli S.A., Migration of particles undergoing pressure-driven flow in a circular conduit, J. Rheol. 41, 621–640 (1997).

[57] Han L.S., Hydrodynamic entrance lengths for incompressible laminar flow in rectangular ducts, J. Appl. Mech. 27, 403-409 (1960).

[58] Haynes R.H.: Physical basis of the dependence of blood viscosity on tube radius. Am. J. Physiol. 198:1193-1200, (1960)

[59] Herschel W.H., Bulkley R., Konsistenzmessungen von gummi-benzollosungen, Kolloid-Zeitschrift 39 (1926) 291–300.

[60] Hookham P.A., Concentration and velocity measurements in suspensions flowing through a rectangular channel, Ph.D. thesis, California Institute of Technology, 1986.

[61] Huilgol R.R., Fluid Mechanics of Viscoplasticity, Springer-Verlag, Berlin-Heidelberg, (2015).

[62] Hund S.J., Kameneva M.V., Antaki J.F., A quasi-mechanistic mathematical representation for blood viscosity, Fluids, 2, 10–36 (2017).

[63] Intaglietta M., Vasomotion and flowmotion: physiological mechanisms and clinical evidence. Vasc. Med. Rev. 2, 1101-112 (1990)

[64] Karnis A., Goldsmith H.L., Mason S.G., The kinetics of flowing dispersions: concentrated suspensions of rigid particles, J. Colloid. Interface Sci. 22, 531–553 (1966).

[65] Koh C.J., Hookham P., Leal L.G., An experimental investigation of concentrated suspension flows in a rectangular channel, J. Fluid Mech, 266, 1–32 (1994).

[66] Krieger I.M., A dimensional approach to colloid rheology, Trans. Soc. Rheol. 7, 101–110 (1963).

[67] Krieger I.M., Rheology of monodisperse lattice, Adv. Colloid Interface Sci. 3, 111–136 (1972).

[68] Lautrup B., Physics of Continuous Matter, Boca Raton, CRC Press, 2011.

[69] Langhaar H.L., Steady flow in the transition length of a straight tube, J. Appl. Mech. 64, A55–A58 (1942).

[70] Lecampion B., Garagash D.I., Confined flow of suspensions modelled by a frictional rheology, J. Fluid Mech. 759, 197 235 (2014).

[71] Leighton D., Acrivos A., The shear-induced migration of particles in concentrated suspensions, J. Fluid Mech. 181, 415–439 (1987).

[72] Leighton D., Acrivos A., Measurement of shear-induced self-diffusion in concentrated suspensions of spheres, J. Fluid. Mech. 177, 109–131 (1987).

[73] Lundgren T.S., Sparrow E.M., J.B. Starr, Pressure drop due to the entrance region in duts of arbitrary cross section, J. Basic Eng. 620-626 (1964).

[74] Martini P., Pierach A., Scheryer E.: Die Stromung des Blutes in engen Gefaben. Eine Abweichung vom Poiseuille'schen Gesetz. Deutsches Archiv fur klinische Medizin; 169:212-222, (1930)

[75] Massoudi M., Vaidya A., Unsteady flows of inhomogeneous incompressible fluids, Int. J. Non-Linear. Mech. 46, 738–741 (2011).

[76] Maxima.sourceforge.net. 2011 Maxima, a computer algebra system, version 5.25.1. See http://www.maxima.sourceforge.net.

[77] McCann H., Pricking the Vessels: Bloodletting Therapy in Chinese Medicine (Singing Dragons, London, 2014)

[78] McDonald D.A., Blood Flow in Arteries, 2nd edn. (The Camelot, Southampton, 1974)

[79] Merrill E.W., Margetts W.G., Cokelet G.C., Gilliland E.R., The Casson equation and rheology of the blood near shear zero, in Proceedings Fourth International Congress on Rheology, Part 4, ed. by A.L. Copley (Interscience, New York, 1965), pp. 135–143.

[80] Meyer C., de Vries G., Davidge S.T., Mayes D.C., Reassessing the mathematical modeling of the contribution of vasomotion to vascular resistance. J. Appl. Physiol. 92, 888-889 (2002)

[81] Mitsoulis E., Flows of viscoplastic materials: models and computations, Rheology Reviews (2007), 135– 178.

[82] Monsorno D., Varsakelis C., Papalexandris M.V., A thermomechanical model for granular suspensions, J. Fluid Mech. 808, 410–440 (2016).

[83] Monsorno D., Varsakelis C., Papalexandris M.V., Poiseuille flow of dense non-colloidal suspensions: The role of intergranular and nonlocal stresses in particle migration, J. Non-Newtonian Fluid Mech. 247, 229–238 (2017).

[84] Muravleva L., Squeeze plane flow of viscoplastic bingham material, J. Non-newton. Fluid Mech. 220 (2015) 148–161.

[85] Muravleva L., Axisymmetric squeeze flow of a Casson medium, J. Nonnewton. Fluid Mech. 267 (2019) 35–50.

[86] Nott P.R., Brady J.F., Pressure-driven flow of suspensions: simulation and theory, J. Fluid Mech. 275, 157–199 (1994).

[87] Oldroyd J., On the Formulation of Rheological Equations of State. Proceedings of the Royal Society of London. Series A, Mathematical and Physical Sciences. 200 (1063), 523-541 (1950)

[88] Papanastasiou T.C., Flow of materials with yield, J. Rheol., 31, (1987), 385–404.

[89] Peskin C., Flow patterns around heart valves. Ph.D. thesis, Albert Einstein College of Medicine, New York, 1972

[90] Peskin C., Flow patterns around heart valves: a numerical method. J. Comput. Phys. 10, 252- 271 (1972)

[91] Peskin C., The immersed boundary method. Acta Numer. 11, 479-517 (2002)

[92] Peskin C., McQueen D., A three-dimensional computational method for blood flow in the heart. J. Comput. Phys. 81, 372-405 (1989)

[93] Phan-Thien N., Graham A.L., Altobelli S.A., Abbott J.R., Mondy L.A., Hydrodynamic particle migration in a concentrated suspension undergoing flow between rotating eccentric cylinders, Ind. Eng. Chem. Res. 34, 3187–3194 (1995).

[94] Phan-Thien N., Fang Z., Entrance length and pulsatile flows of a model concentrated suspension. J. Rheol. 40, 521–529 (1996).

[95] Phillips R.J., Armstrong R.C., Brown R.A., Graham A.L., Abbott J.R., A constitutive model for concentrated suspensions that accounts for shear-induced particle migration, Phys. Fluid A 4, 30–40 (1991).

[96] Pries A.R., Secomb T.W., Gaehtgens P., Gross J.F: Blood flow in microvascular networks. Experiments and simulation. Circ. Res. 67:826-34, (1990)

[97] Putz A., Frigaard I.A., Martinez D.M., On the lubrication paradox and the use of regularization methods for lubrication flows, J. Non-Newton. Fluid Mech. 163 (2009) 62–77.

[98] Popel A.S., Johnson P.C., Microcirculation and hemorheology. Annu. Rev. Fluid Mech. 37, 43-69 (2005)

[99] Rajagopal K.R., Tao L., Mechanics of Mixtures, Singapore, World Scientific, 1995.

[100] Robertson A.M., Sequeira A., Kameneva M.V., Hemorheology, in Hemodynamical Flows: Modeling, Analysis and Simulation, ed. by G.P. Galdi, R. Rannacher, A.M. Robertson, S. Turek. Oberwolfach Seminars, vol. 37 (Birkhauser, Basel, 2008), pp. 63-120

[101] Robertson A.M., Sequeira A., Owens R.G., Hemorheology, in Cardiovascular Mathematics. Modeling and Simulation of the Circulatory System, ed. by L. Formaggia, A. Quarteroni, A. Veneziani, vol. 1 (Springer, Berlin, 2009), pp. 211-242

[102] Rossi S., Anisotropic modeling of cardiac mechanical activation. Ph.D. in Mathematics, IST, Lisbon, and EPFL, 2014

[103] Rossi S., Ruiz-Baier R., Pavarino L.F., Quarteroni A., Orthotropic active strain models for the numerical simulation of cardiac biomechanics. Int. J. Numer. Methods Biomed. Eng. 28, 761-788 (2012)

[104] Rossi S., LassilaT., Ruiz-Baier R., Sequeira A., Quarteroni A., Thermodynamically con- sistent orthotropic activation model capturing ventricular systolic wall thickening in cardiac electromechanics. Eur. J. Mech. A. Solids 48, 129-142 (2014)

[105] Safronchik A.I., Nonstationary flow of a visco-plastic material between parallel walls, J. Appl. Math. Mech., 23, (1959) 1314-1327.

[106] Schiller L., Die enfwicklung der laminaren geschwindigkeitsverfeilung und ihre bedeufung fur zahigkeiismessungen, ZAMM, 2 96-106 (1922).

[107] Schlichting H. Laminare Kanaleinlaufströmung, ZAMM 9, 368-373 (1922).

[108] Schlichting H., Gersten K., Boundary-Layer Theory, Springer, 8th edition, 2000.

[109] Scott-Blair G.W., An equation for the flow of blood, plasma and serum through glass capillaries. Nature 183, 613-614 (1959)

[110] Secomb T.W., Blood flow in the microcirculation, Annu. Rev. Fluid Mech. 49, 443–461 (2017).

[111] Secomb T.W., Pries A.R., Blood viscosity in microvessels: experiment and theory. C R Phys. 2013 June-July; 146:470-478, (2013)

[112] Segré G., Silberberg A. Radial particle displacements in Poiseuille flow of suspensions, Nature 189, 209–210 (1961).

[113] Siegel R., The effect of heating on boundary layer transition for liquid flow in a tube, Sc.D. thesis, Department of Mechanical Engineering, Massachusetts Institute of Technology, 1953

[114] Siginer D.A. Developments in the Flow of Complex Fluids in Tubes, Springer, 2015.

[115] Sinton S.W., Chow A.W., NMR flow imaging of fluids and solid suspensions in Poiseuille flow, J. Rheol. 35, 735-773 (1991).

[116] Sirangelo B., Braca G., Identification of hazard conditions for mudflow occurrence by hydrological model: Application of FLaIR model to Sarno warning system, Eng. Geology 73, 267-276 (2004).

[117] Slezkin N.A., Dynamic of Viscous Incompresible Fluids (in Russian), Gostekhizdat, Moscow, 1955.

[118] Sparrow E.M., Lin S. H., Lundgren T.S., Flow development in the hydrodynamic entrance region of tubes and ducts, Phys. Fluids 7, 338-347 (1964).

[119] Stickell J.J., Powell R.L., Fluid mechanics and rheology of dense suspensions. Annual Rev. Fluid Mech. 37, 129–149 (2005).

[120] Thiriet M., Biology and Mechanics of Blood Flows. Part I: Biology. CRM Series in Mathematical Physics (Springer, Berlin, 2008)

[121] Thurston G.B., Viscoelasticity of human blood. Biophys. J. 12, 1205-1217 (1972)

[122] Thurston G.B., Non-Newtonian viscosity of human blood: flow induced changes inmicrostructure. Biorheology 31(2), 179-192 (1994)

[123] Thurston G.B., Viscoelastic properties of blood and blood analogs. Adv. Hemodyn. Hemorheol. 1, 1-30 (1996)

[124] White F.M., Viscous Fluid Flow. McGraw-Hill, New York. (1991)

[125] Yeleswarapu K.K., Kameneva M.V., Rajagopal K.R., Antaki J.F., The flow of blood in tubes: theory and experiment. Mech. Res. Commun. 25(3), 257-262 (1998)

Acknowledgements

I would like to thank INdAM for the support given me during my PhD.
I wish express my sincere gratitude to the GNFM and its director, Prof. Giuseppe Saccomandi, for giving me the opportunity of attend several scientific events.
I would like to thank Prof. Antonio Fasano for the numerous advices he has given me.
Last but not least, I would like to express my sincere gratitude to Prof. Angiolo Farina for his valuable help during the last years for his patience, motivation, and immense knowledge. Prof. Farina is an important reference point, not only from an academic point of view, but also and especially on a human level.
I could not have imagined having a better advisor and mentor for my Ph.D study.